Design of interdigitated back-contact solar cells by means of TCAD numerical simulations

Vincenzo Maccaronio

Department of Computer Science, Modeling, Electronics and Systems Engineering

University of Calabria

This dissertation is submitted for the degree of

Doctor of Philosophy

November 2016

To my family

Acknowledgements

In these years of Ph.D I've met and worked with many people and I've learned something from each one, so I want to express my gratitude to all of them.

In the first place, I would like to deeply thank my tutors, Prof. Giuseppe Cocorullo and Prof. Felice Crupi, for giving me this opportunity and for their constant guidance and encouragement.

I'm grateful to Dr. Mauro Zanuccoli and Dr. Paolo Magnone, for their invaluable help during the first steps with the TCAD simulator.

My thanks go to all the guys in the laboratory (Antonio, Marco, Noemi, Ramiro, Raffaele), and I want to especially express my gratitude to my colleague and friend Paul Procel, for his kindness and help, and for the countless and enlightening discussions, on working topics and not.

During this Ph.D course I had the chance to spend some months at the Delft University in the Netherlands, and for this experience I'm thankful to Prof. Miro Zeman and Prof. Olindo Isabella, along with Dr. Andrea Ingenito and the other Ph.D students there.

Aside from the working environment, I must say thank you to all my friends, who supported me in many ways (and kept me sane): Alessandro, Davide, Silvio and also, Claudio, Andrea, Antonio, Mauro, Piero.

Finally, I'm grateful to my parents and my sister Flavia, for being there for me whenever I need them.

Summary

The widespread adoption of renewable energies has become of paramount importance to reduce the impact of fossil fuels on the global climate and, amongst all the possible sources, photovoltaic technology has the potential to be the leading one. The key point for its faster diffusion is the reduction of the fabrication costs, and for this purpose a deep optimization study is necessary. The vast majority of the photovoltaic production is based on crystalline silicon, mainly for historical and economical reasons, and, among the wide variety of solar cells, currently both the most efficient laboratory cell and commercial module are based on the *back-contact* architecture.

This kind of structure, which features both the metallic contacts on the rear side, offers many advantages over the conventional solar cell, including zero shadowing losses and better appearance, but it's higher complexity requires a careful design process. Due to the increasing computational power and modeling accuracy, in the last years the study of high efficiency solar cells design has been greatly enhanced by the use of numerical simulations. This kind of approach allows to significantly reduce the investigation costs while provides a deep insight on the working mechanisms and the source of losses.

The aim of this work of thesis is to provide production design guidelines for *interdigitated back-contact* (iBC) solar cells, obtained by a thorough analysis of the impact of the fabrication parameters on the performance, conducted by means of TCAD numerical simulations.

In the first chapter of the thesis the physics of a solar cell has been explained and all the working principles detailed, starting with the light

absorption process, moving to the creation of the charges and ending with their collection to generate power. The recombination mechanisms, along with others loss causes, have been presented and examined.

In the second chapter, the architecture of a cell has been illustrated, highlighting the different regions and presenting the back-contact architecture. The third chapter has been dedicated to the explanation of the simulation strategy used in this work, with the definition of the physical models applied and calibrated to ensure the required accuracy.

In chapter four and five the simulations results have been presented and explained. In particular, chapter four shows the trends of the figures of merit with respect to the doping peak variations in the three main doped regions of an iBC (emitter, BSF and FSF). A bell shape in efficiency has been found in all the cases, determined by a trade off between high recombination effects both for low and high doping levels. Specifically, for low doping levels the main contribution comes from recombination on contacts in the emitter and BSF, and surface recombination in FSF. For high doping levels, the dominant mechanisms are Auger recombination in emitter and BSF and surface recombination in the FSF. In chapter five are presented the effects on efficiency trends of the rear side geometry variations, in particular of the dimension of gap, pitch, thickness and the optimal emitter coverage. The results show that the highest efficiencies can be reached with smaller gap and pitch, due to the detrimental effect of larger geometries on resistive and recombination losses. The optimal thickness for a cell with the simulated parameters has been determined as 200 μm, for a trade off between optical generation and SRH recombination. The analysis on the optimal emitter coverage pointed out that is not possible to determine an absolute optimum value, since it depends on the main regions doping and bulk resistivity, but only a relative one, ranging from 80% to 90%. Finally, it has been shown that an additional metal line contact for the emitter region improves the conversion efficiency due to lower resistive losses, in particular in case of long emitters.

Sommario

La promessa dell'energia solare come forma di energia principale è sempre più concreta, ma il nodo cruciale rimane il costo per Watt, che deve essere sempre di più avvicinato o finanche ulteriormente ridotto rispetto a quello delle reti di distribuzione energetiche esistenti. Un lavoro di ottimizzazione in termini di design e parametri di fabbricazione è quindi fondamentale per raggiungere questo obiettivo. Il silicio cristallino è il materiale maggiormente diffuso nell'industria fotovoltaica, per via di diversi fattori, tra cui l'ottimo rapporto costo/prestazioni e la vasta presenza di macchinari per la sua lavorazione, dovute al suo impiego pluridecennale nell'industria microelettronica.

Fra le diverse tipologie di celle esistenti è stata scelta un'architettura che presenta entrambi i contatti metallici sul retro, chiamata per questo *interdigitated back-contact* (iBC). Questo particolare design offre numerosi vantaggi in termini di efficienza massima, costo di produzione ed estetica del pannello, in relazione alle celle convenzionali. Difatti, al momento attuale le maggiori efficienze in celle monogiunzione, sia a livello di laboratorio che di moduli commerciali, sono state ottenute utilizzando questa struttura, sulla quale un'approfondita attività di ricerca può quindi dimostrarsi di notevole interesse.

Per il processo di analisi è stato scelto un approccio numerico, tramite l'uso del simulatore di dispositivi TCAD Sentaurus di Synopsys. L'utilizzo di simulazioni offre numerosi punti a favore rispetto all'ottimizzazione per mezzo di step ripetuti di fabbricazione. In primis, un vantaggio in termini di costi, non necessitando di macchinari, materiali e camere pulite. Inoltre un'analisi numerica rende possibile individuare ed evidenziare punti o cause specifiche di perdite o problemi di progettazione. La problematica maggiore di questo approccio risiede nella necessità di garantire l'affidabilità delle simulazioni e ciò è stato ottenuto mediante l'applicazione dello stato dell'arte di tutti i modelli fisici specifici coinvolti nel funzionamento di questo tipo di celle.

La tematica di ricerca affrontata è stata quindi la progettazione di celle solari al silicio con contatti interdigitati sul retro tramite l'uso di simulazioni numeriche. Il lavoro di ottimizzazione è stato realizzato investigando uno spazio di parametri di fabbricazione molto vasto e ottenendo informazioni sui trend delle prestazioni al variare degli stessi.

Nel primo capitolo è stata illustrata la fisica e i principi di funzionamento di una cella solare, iniziando dall'assorbimento della luce, passando alla sua conversione in cariche elettriche, per finire con la loro raccolta per generare potenza. I meccanismi di ricombinazione e le altre cause di perdite sono stati presentati ed esaminati. Nel secondo capitolo è stata dettagliata l'architettura di una cella solare, evidenziando le diverse regioni e presentando la struttura *back-contact*. Il terzo capitolo è stato dedicato alla spiegazione delle strategie di simulazione applicate in questo lavoro, con la definizione dei modelli fisici applicati e calibrati per assicurare l'accuratezza richiesta.

Nei capitoli quattro e cinque sono stati presentati i risultati delle simulazioni effettuate, realizzate variando le caratteristiche geometriche delle diverse regioni della cella e i profili di drogaggio. Sono stati ottenuti i trend di comportamento relativi ai singoli parametri che, nel caso relativo ai drogaggi, permettono di affermare che per ogni regione l'andamento dell'efficienza ha una forma a campana, che presenta un ottimo di drogaggio relativo in un punto intermedio. Questo comportamento è dovuto, per bassi valori di drogaggio, all'effetto della ricombinazione sul contatto per BSF ed emettitore e della ricombinazione superficiale per l'FSF. Per alti valori di drogaggio, la degradazione dell'efficienza dipende dall'effetto della ricombinazione Auger per BSF ed emettitore e da quella superficiale per l'FSF. Per quanto riguarda i parametri geometrici, le analisi svolte evidenziano che il gap tra emettitore e BSF deve essere quanto più piccolo possibile, dato che all'aumentare della sua dimensione aumentano le perdite per effetto resistivo e di ricombinazione. È stato determinato che il valore ottimale di emitter coverage non è assoluto, ma dipende dalla resistività del bulk e dai drogaggi delle altre regioni, os-

cillando tra l'80% e il 90%. Per quanto riguarda il pitch ottimale, cioè la distanza tra i contatti, è stato determinato che maggiori efficenze corrispondono a valori minori, principalmente perché all'aumentare della distanza aumentano le resistenze parassite. Infine si è evidenziato che l'aggiunta di un secondo contatto sull'emettitore, equispaziato dal centro della regione, migliora l'efficienza totale poiché riduce le perdite resistive, soprattutto nel caso di celle con emettitori lunghi.

Table of contents

Acknowledgements **v**

Summary **vii**

List of figures **xvii**

List of abbreviations and symbols **xxvii**

Introduction **1**

Chapter 1 Device physics of a solar cell **7**

1.1 Solar cell operating principle 7
1.2 Light absorption 8
1.3 Carrier Recombination 11
1.3.1 Radiative Recombination 13
1.3.2 Auger Recombination 14
1.3.3 Shockley-Read-Hall recombination 15
1.4 Carrier transport inside a semiconductor 18
1.4.1 Drift-Diffusion Model 19
1.4.2 Semiconductor Equations 21
1.5 *pn*-junction electrostatic model 23
1.6 Solar cell characteristics and figures of merit 28
1.6.1 Boundary conditions and I-V characteristic 28
1.6.2 Solar cell figures of merit 33
1.6.3 Other figures of merit 35
1.7 Loss mechanisms and temperature effect 37
1.7.1 Optical losses 37

1.7.2 Recombination Losses 37
1.7.3 Parasitic resistance effects 39
1.7.4 Temperature effect 41
1.8 Limits in conversion efficiency 42
Chapter 2 Solar cell fabrication process and architecture 45
2.1 Fabrication process 45
2.1.1 Process flow 46
2.2 Solar cell architectures 51
2.2.1 Bulk region 51
2.2.2 Front surface 54
2.2.3 Back surface 56
2.3 Back-contact solar cells 56
2.3.1 Metal wrap-through (MWT) 58
2.3.2 Emitter wrap-through (EWT) 59
2.3.3 Interdigitated back-contact (iBC) 60
Chapter 3 Solar cell numerical modeling 63
3.1 Introduction to solar cell numerical simulations 63
3.2 Finite Element Method 64
3.3 Physical models 67
3.3.1 Carrier statistics 67
3.3.2 Band Gap Narrowing (BGN) 68
3.3.3 Carriers mobility model 71
3.3.4 Bulk recombination 71
3.3.5 Surface recombinations 73
3.4 Optical generation 75
3.5 Simulation domain and meshing strategy 80
Chapter 4 Optimization of doping parameters 85
4.1 Simulation methodology 85
4.2 Planar front surface 87

4.2.1 FSF region 87
4.2.2 BSF region 89
4.2.3 Emitter region 91
4.3 Textured front surface 93
4.3.1 FSF region 95
4.3.2 BSF region 98
4.3.3 Emitter region 100
4.4 Conclusions on doping parameters variations 103
Chapter 5 Optimization of geometrical parameters 107
5.1 Simulation methodology 107
5.2 Planar front surface 108
5.2.1 Gap width 109
5.2.2 Emitter width 111
5.2.3 Pitch width 113
5.3 Textured front surface 115
5.3.1 Gap width 115
5.3.2 Emitter width 118
5.3.3 Optimum Emitter coverage 120
5.3.4 Pitch width 123
5.3.5 Substrate thickness 125
5.4 Double Emitter contact 127
5.5 Conclusions on geometrical parameters 131
Conclusions 135
References 137
List of Publications 147

List of figures

1 World total primary energy supply (TPES) from 1971 to 2014 in Mtoe (Million Tons of Oil Equivalent). 2

2 Estimated renewable energy share of global final energy consumption (2014). 3

3 Solar PV global capacity by country/region, 2005-2015. 4

1.1 Spectrum irradiance for three standardized solar spectra. The reference spectrum used in this work is the AM1.5 Global. . . 9

1.2 Direct bandgap photon absorption process. E_1 and E_2 are respectively the energy of an electron before and after the photon absorption. E_g is the bandgap. 10

1.3 Indirect bandgap photon absorption process. E_1 and E_2 are the initial and final electron energy respectively. The transition requires a phonon absorption or emission whether the photon energy is lower ($h\nu < E_g$) or higher ($h\nu > E_g$) than the bandgap. 11

1.4 Absorption coefficient for direct (GaAs) and indirect (Si) semiconductor at 300K. The bandgaps are 1.4 and 1.12 eV respectively 12

1.5 Radiative recombination mechanism. An electron in conduction band recombines with an hole in the valence emitting a photon in the process 13

1.6 Auger recombination mechanism in conduction (a) and valence (b) band. An electron in conduction band gives its excess energy to another electron and recombines with a hole. The excited electrons releases its energy through lattice interactions. Same process occurs in the valence band for holes. 15

1.7 SRH recombination by defect levels 16

1.8 Band bending and drift movement in semiconductor 20

1.9 Simple solar cell schematic (1D abrupt pn-junction). Front contact is on the n-type side, back contact on the p-type side. The junction is in $x = 0$, and the depletion region extends from $-x_N$ to x_P. 24

1.10 *pn*-junction equilibrium conditions. (a) Energy bands diagram: E_c, E_i, E_F and E_V are the conduction band energy, the intrinsic energy level, the Fermi energy level and the valence band energy level, respectively. E_0 is the vacuum energy and χ the electron affinity. (b) Electric field in the semiconductor. (c) Charge density in the semiconductor. 27

1.11 Schematic equivalent circuit for a solar cell. Diode 1 represents the recombination current in the quasi-neutral regions, while diode 2 the recombination in the depletion region. . . . 33

1.12 Voltage-current characteristic of a solar cell. P_m is the point where the output power is maximum. I_{SC} is the maximum current (short-circuit current) and V_{OC} is the maximum voltage (open circuit voltage). 34

1.13 Optical losses in a solar cell. Light can be reflected, blocked by contacts or being reflected from the rear surface without being absorbed. 38

1.14 Solar cell equivalent circuit including parasitic series resistance R_S and shunt resistance R_{Sh}. 39

1.15 Effect of series resistance on the I-V characteristic of a solar cell ($R_{Sh} = 0$). 40
1.16 Effect of shunt resistance on the I-V characteristic of a solar cell ($R_S = 0$). 41
1.17 Shockley-Queisser efficiency limits versus bandgap: (a) unconcentrated 6000K black body radiation, (b) fully concentrated 6000K black body radiation, (c) unconcentrated AM1.5-Direct and (d) AM1.5-Global. 43

2.1 Typical fabrication process flow with subsequent steps. . . . 50
2.2 Conventional solar cell basic architecture. 51
2.3 Front surface texturing effects: (a) decreased reflection and (b) increased photogeneration. 55
2.4 Conventional solar cell architecture. 58
2.5 Metal wrap-through (MWT) solar cell architecture. 59
2.6 Emitter wrap-through (EWT) solar cell architecture. 60
2.7 Interdigitated back-contact (iBC) solar cell architecture. . . . 60

3.1 Finite element method mesh implementation example. . . . 66
3.2 Intrinsic carrier density accounting for BGN for different models, including the revised one used for the simulations. . 70
3.3 The symbols are measured minority electron mobility (left) and minority hole mobility (right). Klaassen's model of the majority mobility is shown as dashed line, while model of the minority as solid line. 71
3.4 Surface recombination velocities for holes s_{p0} as function of the doping level. Symbols are measurements in different scenarios while lines are parametrization of eq. (3.24), dashed for textured and solid for planar surfaces, respectively. . . . 75
3.5 Schematic of the 3D simulated domain for the optical generation calculation (left) and 2D slice (right). 76

3.6 Reflection and transmission of an incident ray at planar surface. 77
3.7 Thin layer stack boundary condition used to simulate the ARC. 78
3.8 Optical generation in the simulation domain of the solar cell. 80
3.9 3D sketch of an iBC solar cell. 81
3.10 2D longitudinal slice of the 3D structure of fig. 3.9. 81
3.11 Simulation domain used in this work and definition of the main regions. 82
3.12 Overall simulation mesh across the simulated domain. 82
3.13 Meshing strategy on the top surface, finer to better simulate FSF auger recombination, surface recombination and higher optical generation. 83
3.14 Meshing strategy on the rear surface, finer to better simulate Auger recombination in emitter and BSF, surface recombination on the passivation and the contacts. 83

4.1 Element of symmetry used for doping parameters variation simulations. 86
4.2 Efficiency, short-circuit current density J_{SC}, open-circuit voltage V_{OC} and Fill Factor for FSF doping peak $D_{FSF,pk}$. 88
4.3 Dark recombination current density components for simulations changing FSF doping peak $D_{FSF,pk}$. 88
4.4 Efficiency, short-circuit current density J_{SC}, open-circuit voltage V_{OC} and Fill Factor for BSF doping peak $D_{BSF,pk}$. 90
4.5 Dark recombination current density components for simulations changing BSF doping peak $D_{BSF,pk}$. 90
4.6 Efficiency, short-circuit current density J_{SC}, open-circuit voltage V_{OC} and Fill Factor for Emitter doping peak $D_{emi,pk}$. . . 92
4.7 Dark recombination current density components for simulations changing Emitter doping peak $D_{emi,pk}$. 92
4.8 Doping profiles in the three regions: (a) FSF, (b) BSF) and (c) Emitter. Doping peaks value changes through the simulations. 94

4.9 Efficiency, short-circuit current density J_{SC}, open-circuit voltage V_{OC} and Fill Factor for FSF doping peak $D_{FSF,pk}$. 95
4.10 Recombination losses components under illumination in short-circuit for FSF doping peak $D_{FSF,pk}$. 96
4.11 Comparison of minority carrier (hole) density and electrical field intensity for different FSF doping peak concentration. . 97
4.12 Efficiency, short-circuit current density J_{SC}, open-circuit voltage V_{OC} and Fill Factor for BSF doping peak $D_{BSF,pk}$. 98
4.13 Recombination losses components under illumination in short-circuit for BSF doping peak $D_{BSF,pk}$. 99
4.14 Comparison of minority carrier (hole) density and electrical field intensity for different BSF doping peak concentration. . 100
4.15 Efficiency, short-circuit current density J_{SC}, open-circuit voltage V_{OC} and Fill Factor for Emitter doping peak $D_{emi,pk}$. . . 101
4.16 Saturation current competitive components in dark conditions as function of Emitter doping peak $D_{emi,pk}$. 102
4.17 Comparison of electron density and electrical field intensity for different emitter doping peak concentration. 103

5.1 Element of symmetry used for doping parameters variation simulations. 108
5.2 Efficiency, short-circuit current density J_{SC}, open-circuit voltage V_{OC} and Fill Factor for gap width variations. 110
5.3 Dark recombination current density components for simulations changing gap width. 110
5.4 Efficiency, short-circuit current density J_{SC}, open-circuit voltage V_{OC} and Fill Factor for emitter/pitch ratio R variations. . 112
5.5 Dark recombination current density components for simulations changing emitter/pitch ratio R. 112
5.6 Efficiency, short-circuit current density J_{SC}, open-circuit voltage V_{OC} and Fill Factor for pitch size variations. 114

5.7 Dark recombination current density components for simulations changing pitch size. 114
5.8 Efficiency, short-circuit current density J_{SC}, open-circuit voltage V_{OC} and Fill Factor for gap width variations. 117
5.9 Light recombination current density components for simulations changing gap width. 117
5.10 Efficiency, short-circuit current density J_{SC}, open-circuit voltage V_{OC} and Fill Factor for emitter/pitch ratio R variations. . 119
5.11 Light recombination current density components for simulations changing emitter/pitch ratio R. 119
5.12 R_{opt} dependence from BSF and emitter doping for bulk resistivity of (a) 1 $\Omega \cdot cm$ and (b) 10 $\Omega \cdot cm$. Dotted lines illustrate calculated efficiencies. 121
5.13 Calculated R_{opt} for different values of pitch (left), emitter width (middle) and BSF width (right). Numbers above points are calculated efficiencies. Starred point is the highest simulated efficiency. 121
5.14 Simulated efficiency dependence from BSF and emitter width for a bulk resistivity of (a) 1 $\Omega \cdot cm$ and (b) 10 $\Omega \cdot cm$. In both cases, the BSF and the emitter width can be optimized independently one another. 122
5.15 Efficiency, short-circuit current density J_{SC}, open-circuit voltage V_{OC} and Fill Factor for pitch size variations. 124
5.16 Light recombination current density components for simulations changing pitch size. 124
5.17 Efficiency, short-circuit current density J_{SC}, open-circuit voltage V_{OC} and Fill Factor for substrate thickness variations. . . 126
5.18 Dark recombination current density components for simulations changing substrate thickness. 126

5.19 Sketch of the simulated iBC solar cell with double emitter contact. 128
5.20 Efficiency (color scale) and FF (dotted lines) as a function of f and d/W_{emi} for a fixed $W_{emi} = 1200\mu m$. 129
5.21 Efficiency as a function of d/W_{emi} (dotted line represents the efficiency in case of single emitter contact). 130
5.22 Efficiency and figures of merit as a function of W_{emi} with single and double contact at emitter region, $W_C = 5\mu m$. . . . 131

List of abbreviations and symbols

Roman Symbols

$D_{BSF,pk}$ Peak doping concentration of the BSF region

$D_{emi,pk}$ Peak doping concentration of the Emitter region

$D_{FSF,pk}$ Peak doping concentration of the FSF region

E_c Conduction band energy level

E_F Fermi energy level

E_g Energy bandgap

E_i Intrinsic energy level

E_V Valence band energy level

f Emitter metal coverage

I_m Maximum Power Point Current

I_{SC} Short-circuit Current

J_{ph} Photogenerated Current Density

J_{SC} Short-circuit Current Density

P_m Maximum Power Point

R Emitter/Pitch width ratio

R_{opt} Optimum emitter coverage

R_S Series Resistance

R_{Sh} Shunt Resistance

V_{bi} Built-in voltage

V_m Maximum Power Point Voltage

V_{OC} Open-circuit Voltage

W_{BSF} BSF region width

W_C Metal contact width

W_{emi} Emitter region width

Greek Symbols

τ Minority carriers lifetime

τ_{bulk} Bulk minority carriers lifetime

τ_{Auger} Auger minority carriers lifetime

τ_{eff} Effective minority carriers lifetime

τ_{rad} Radiative minority carriers lifetime

τ_{SRH} SRH minority carriers lifetime

Acronyms / Abbreviations

APCVD Atmospheric pressure chemical vapor deposition

ARC Anti-reflective coating

BC-BJ	Back-contact back-junction solar cell
BGN	Band-Gap Narrowing
c-Si	Monocrystalline silicon
Cz	Czochralski fabrication process for silicon
EQE	External Quantum Efficiency
EWT	Emitter Wrap-Through solar cell
FEM	Finite Element Method
FF	Fill Factor
FZ	Float Zone fabrication process for silicon
iBC	Interdigitated back-contact solar cell
IQE	Internal Quantum Efficiency
LLI	Low level of injection
MWT	Metallization Wrap-Through solar cell
RIE	Reactive Ion Etching
SRH	Shockley-Read-Hall recombination
SRV	Surface Recombination Velocity
TCAD	Technology Computer-Aided Design
TMM	Transfer Matrix Method

Introduction

Two opposite phenomena are nowadays driving the energy production on a global scale. On one hand, there is an ever growing need for energy (see fig. 1), either for the constant increase of the human population or for the search of improved life's quality from larger portions of the society, especially in the once less developed areas of the world. On the other hand, the human activities responsible for energy production have caused, and continues to cause, global climate changes. Global warming is an established and well documented reality: the period from 1983 to 2012 was the warmest 30-year period of the last 1400 years [1] and recently the concentration of CO_2 in the atmosphere surpassed the 400 ppm, the highest value in more than 3 million years of Earth history [2]. Governments are discussing the matter and trying to propose solutions (although not equally shared), as the *Kyoto Protocol* in 2005 or the last year *Paris Agreement*, in order to contain the warming below 2 °C [3], considered a non-returning point for the global climate.

Evaluating the necessary interventions required, the highest priority goes to the drastic reduction of the carbon emission in the atmosphere, supposedly reached by 2030. However, since the main sources for energy production still are, by far, the fossil fuels (see fig. 2), the urge for a widespread adoption of renewable energy sources is now more pressing than ever. Amongst the viable options, the solar power is the one with the potential to most likely become the world's primary source. The power of the sunlight reaching the Earth's surface is thousands of times sufficient to fulfill the overall global consumption [4],

moreover solar generation has the highest power density in the renewable energies category. This type of energy production doesn't create pollution or byproducts, and the end-wastes are manageable with existing pollution controls. The solar light can be directly converted in electric power using the photovoltaic (PV) cells.

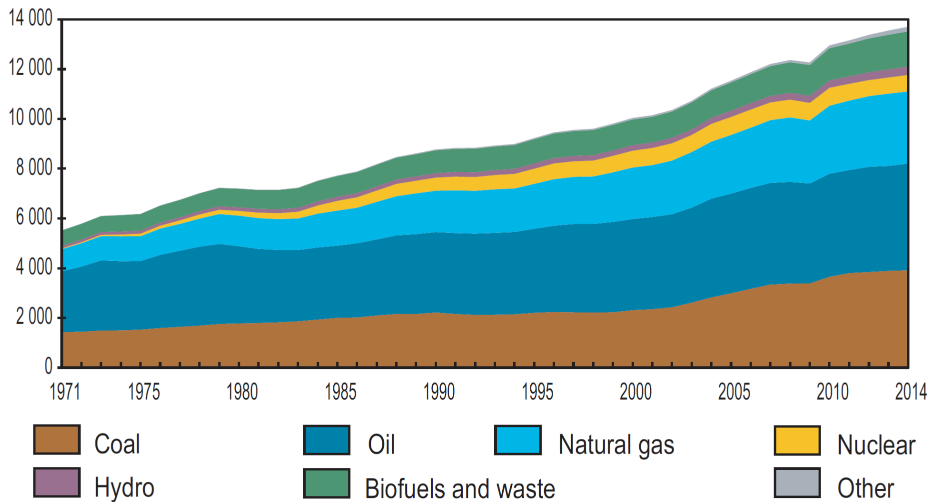

Fig. 1 World total primary energy supply (TPES) from 1971 to 2014 in Mtoe (Million Tons of Oil Equivalent) [5].

Even if the photovoltaic market is experiencing a record growth in the last years, with the 2015 market capacity up to 25% over the 2014's, for a total capacity of 227 GW, still the overall energy production from photovoltaic sources is just around 2% of the global electricity demand. The main obstacle to the diffusion of the this technology is the cost, in the form of the so called *grid parity*, i.e the possibility to generate PV power at a cost equal or lower to the price of the electricity grid. The *grid parity* has already been reached in some countries [7] but, in order to achieve the highest diffusion of photovoltaic technology, and given the drop in the price of fossil fuels after the financial crisis in 2008, the need for reducing the cost and increasing

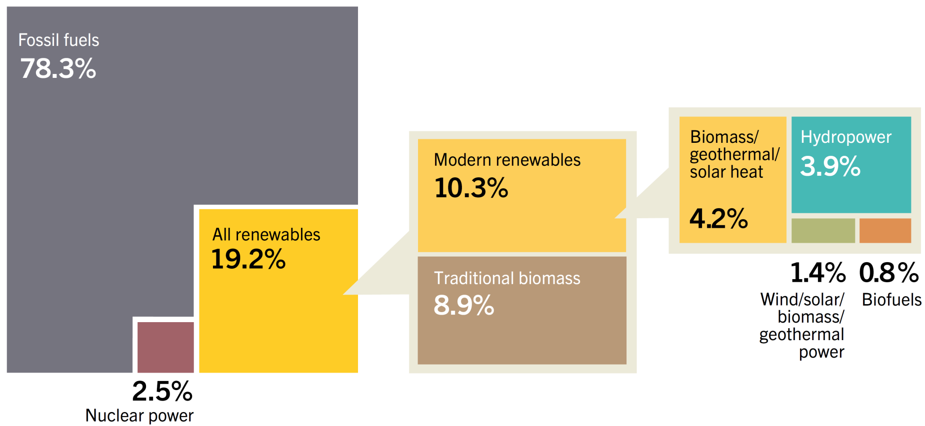

Fig. 2 Estimated renewable energy share of global final energy consumption (2014) [6].

the efficiency in PV production is still of paramount importance to maintain and increase this growing trend (see fig. 3). The key to accomplish this result is a process of design optimization, based on the understanding and the reduction of the loss mechanism, along with the creation of guidelines for the manufacturers, to better calibrate the production process to get highest efficiency for the fabricated cells.

Though, especially in the recent past, many different types of solar cells and various materials have been studied and produced, silicon wafer based PV technology is accounted for about 93 % of the total production in 2015 [8]. The main reason is linked to the usage, for many decades, of silicon in the microelectronic industry, which makes it one of the most well know materials and one of the cheaper to produce on mass scale, given the diffusion of facilities dedicated to its fabrication.

The highest efficiency crystalline silicon solar cell at laboratory level reaches 25.6% [9], while the most efficient solar panel already on the market has a conversion efficiency of 21.5% [10]. Both of this devices use the back-contact architecture, studied in this work. This kind of structure presents

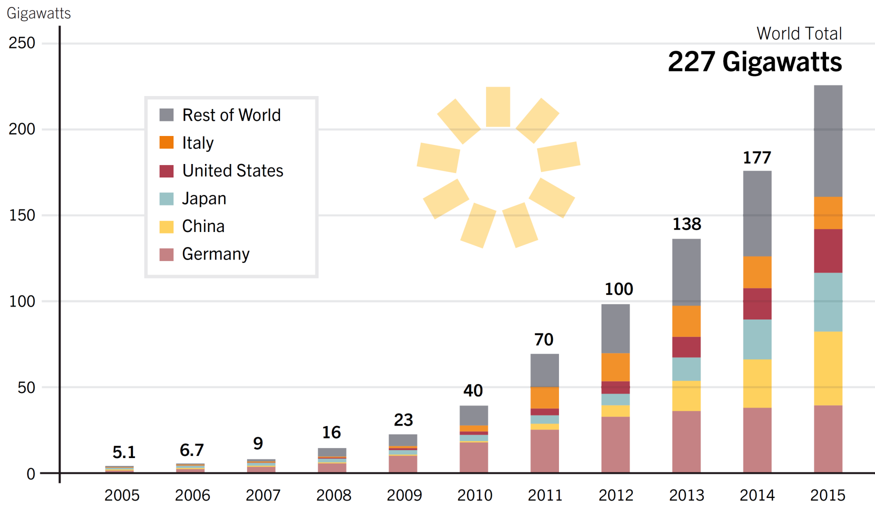

Fig. 3 Solar PV global capacity by country/region, 2005-2015 [6].

many advantages over the conventional solar cell, but the more complex configuration implies higher fabrication costs. Since the potential to optimize this type of structure is noticeable, in order to achieve the possibility of high-efficiency solar cell production at lower cost, an extensive study has been carried out.

The aim of this work of thesis is to provide guidelines and design advices for the fabrication of crystalline silicon interdigitated back contact solar cells, with the goal of efficiency improvement while reducing the production costs. In order to achieve this objective, a multidimensional simulation approach has been used, by means of TCAD electronic device software simulator Sentaurus, from Synopsys [11]. The use of simulations allowed a deep analysis of the performance of this kind of solar cell, highlighting the main causes of losses, either in nature or in position, given the possibility to examine all the electrical mechanism inside the device. A wide range of fabrication parameters has been analyzed, including doping and geometries of the structure, pointing out

the most appropriate production strategy to apply for each of them in order to maximize the conversion efficiency.

Thesis outline

A summary of the content of each chapter of this thesis is presented below:

Chapter 1 : in this chapter a review of the physics behind the operation of a solar cell is presented, detailing the processes that allows to convert the solar light power into electrical power, describing the mechanisms which hamper or degrade the efficiency in performing this task and defining the maximum theoretical limits to the energy conversion.

Chapter 2 : in this chapter a quick view on the fabrication process of a solar cell is provided, along with the illustration of the regions composing the structure of a cell, detailing their function and characteristics. In the second part, the architecture of back-contact solar cells, modeled in this work, is presented.

Chapter 3 : the aim of this chapter is to explain in detail how the simulations used in this analysis was performed. The physical models applied to emulate the actual behavior of a cell are explained, as well as the characteristics of the TCAD software simulator employed, and the strategies to optimize the simulation process.

Chapter 4 : in this chapter are presented the analysis made regarding doping parameters variation effects on the performance of an iBC solar cell. Planar and textured solar cells behaviors have been simulated and the efficiency trends are extracted providing indications to improve the design process with respect to the doping characteristics of the main regions of the cell.

Chapter 5 : the analysis presented in this chapter concern the performance trends with respect to geometrical parameters variation on both planar and textured iBC solar cells. Loss mechanisms have been pointed out and guidelines for the optimization of the fabrication process geometries are provided.

Chapter 1

Device physics of a solar cell

In this chapter silicon solar cells operating principles will be presented and explained. This section is organized in a similar way and essentially follows the correspondent arguments presented by Jeffery Gray in the *Handbook of Photovoltaic Science and Engineering* [12]. The process to transform the sunlight power to output electrical power will be detailed, following the conversion of light in electrons, the movement of electrons in the semiconductor and their collection using a *pn*-junction. The mechanisms of recombination and losses will be pointed out. The main figures of merit to describe the electrical behavior of a solar cell will be presented, along with the maximum theoretical efficiency limits of sunlight conversion.

1.1 Solar cell operating principle

The working principle of a silicon solar cells is the so-called *photovoltaic effect* [13], discovered by E. Beckerel in 1839. This effect causes the production of electrons inside certain materials when exposed to light. An electrical potential is created by the freeing of electrons from atoms due to the absorptions of photons. In a solar cell these free electrons, which are not in equilibrium thus tend to recombine quickly, are separated from the relative

holes and forced to pass through an external circuit by the presence of an energy band bending created with an electrical junction. A large number of materials have been proved to be adequate for energy production using this effect, but the most common and diffused one, by far, is silicon. The reason of this choice is mainly economic, since silicon is a very well known material and its production for microelectronic purpose is widely established. The final cost is in fact the key point for PV development and diffusion.

1.2 Light absorption

The first step in the production of energy from a solar cell is, as the name says, the sunlight. The Sun produces a wide spectrum of electromagnetic radiations, but its characteristics on the surface of the earth depend on many conditions, as the daytime and the position. To allow performance comparison of various devices from different research centers and manufacturers, standard spectra have been defined. In fig. 1.1 are shown three of these spectra. The AM0 is referred to the solar irradiance in space, which an integrated power of 1366.1 W/m^2. The AM1.5 standards refer to earth surface irradiation in conditions of an absolute air mass of 1.5 (i.e. an average latitude for US and Europe). AM1.5 Direct is used for solar concentrator and takes in account the direct illumination plus the component in a disk 2.5 degree around the Sun. The spectrum generally used for solar cell characterization is the AM1.5 Global, which has an integrated power of 1000 W/m^2 [14].

When light shines on a semiconductor, a portion of the incident power will be absorbed in a process called *fundamental absorption*, in which a photon with energy $E = h\nu$, where h is the Planck constant and ν is the frequency of the light, excites an electron from the valence band to the conduction band, leaving a hole behind. Both the total energy and momentum of all the particles involved must be conserved. In the case of direct bandgap semiconductors, where in relation to the crystal momentum p the minimum

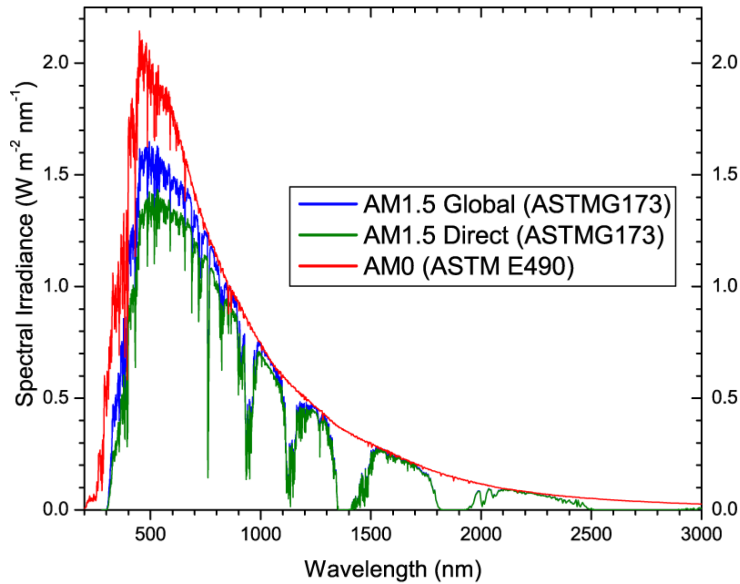

Fig. 1.1 Spectrum irradiance for three standardized solar spectra. The reference spectrum used in this work is the AM1.5 Global.

of the conduction band correspond with the maximum of the valence band (see fig. 1.2), the momentum is conserved and the final energy of the electron E_2 will be the initial energy E_1 plus the photon energy $h\nu$. The probability of this process depends directly on the concentrations of electrons and holes. This process could happen only if the energy received by the electron from the photon is enough to overcome the bandgap E_g, i.e. energy states not allowed for electrons. Photons with an energy lower than the bandgap will not be absorbed, instead they will pass through the semiconductor without interactions. In the case of indirect bandgap semiconductors, such as silicon, the minimum of the conduction band is at a different crystal momentum than the maximum of the valence band (see fig. 1.3). Momentum conservation of the electron requires an additional particle, a phonon, representative of the lattice vibration. An electron with initial energy E_1 can be excited from valence band to conduction band (final energy E_2) by a photon and a phonon

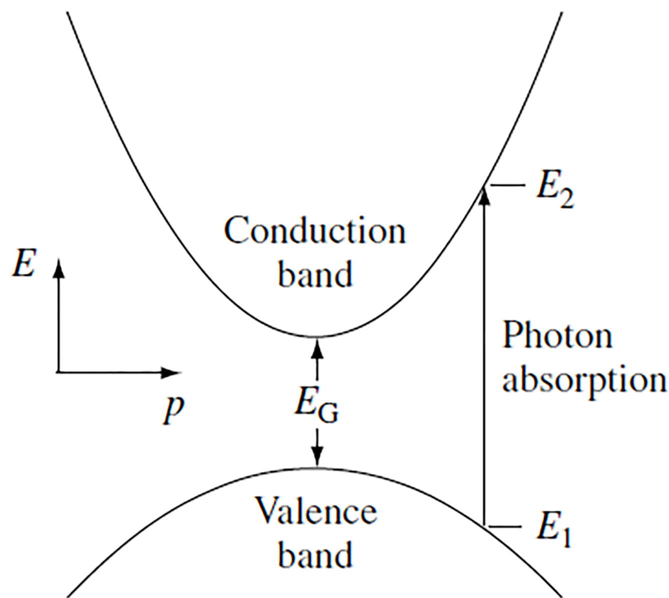

Fig. 1.2 Direct bandgap photon absorption process. E_1 and E_2 are respectively the energy of an electron before and after the photon absorption. E_g is the bandgap.

absorption (if the photon energy $h\nu < E_g$) or by a photon absorption and a subsequent phonon emission (if the photon energy $h\nu > E_g$).

Since the absorption process involves two different particles, the probability in the case of indirect bandgap is lower than the direct bandgap case, thus light penetrates more deeply into the semiconductor. Fig. 1.4 shows the absorption coefficient for a direct (GaAs) and indirect (Si) bandgap semiconductor respectively [15]. In analysis and modeling, measured absorption coefficients or empirical expression for the absorption coefficient are used.

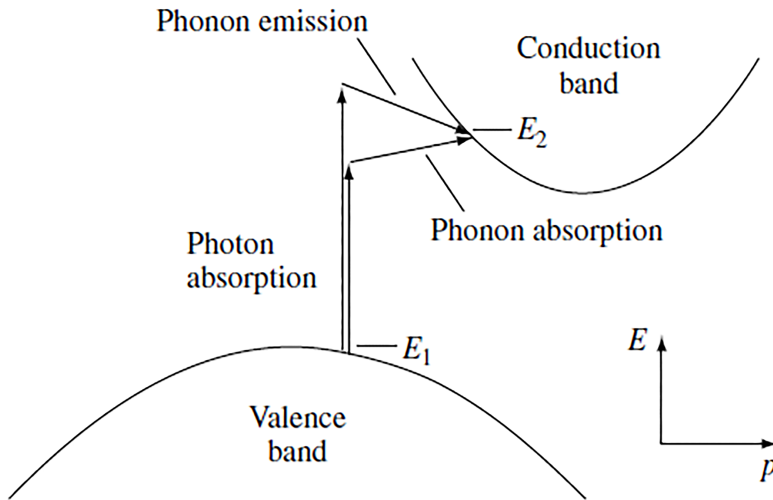

Fig. 1.3 Indirect bandgap photon absorption process. E_1 and E_2 are the initial and final electron energy respectively. The transition requires a phonon absorption or emission whether the photon energy is lower ($h\nu < E_g$) or higher ($h\nu > E_g$) than the bandgap.

1.3 Carrier Recombination

The excitation of electrons inside the semiconductor creates a non equilibrium condition, where the excited electrons in the conduction band will tend to fall back to their initial energy, refilling the holes previously created in the valence band, in a process called *recombination*. The time in which this event occurs is called *minority carrier lifetime*, τ , and is used to quantify the recombination losses in a semiconductor. Lifetime is a statistical concept that represents the amount of time a photo-excited electron survives before recombining, and is expressed as:

$$\tau = \frac{\Delta n}{U} \tag{1.1}$$

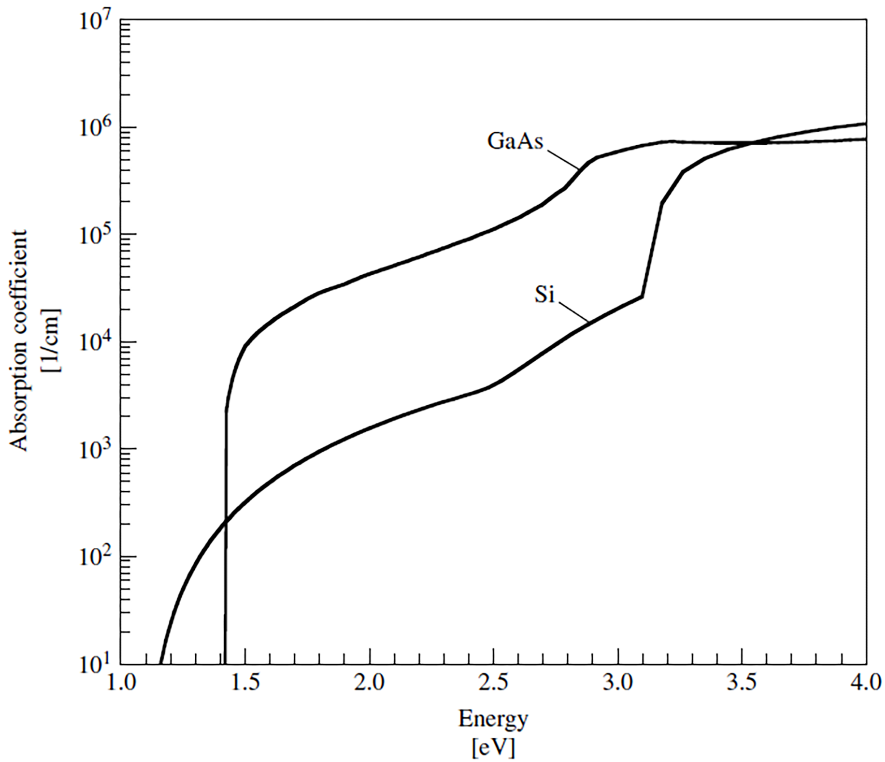

Fig. 1.4 Absorption coefficient for direct (GaAs) and indirect (Si) semiconductor at 300K. The bandgaps are 1.4 and 1.12 eV respectively

where U is the volume recombination rate (cm^{-3}/s) and Δn is the excess carrier concentration for volume unit (cm^{-3}).

Three main recombination mechanisms occur in a semiconductor:

1. Radiative recombination
2. Auger recombination
3. Shockley-Read-Hall (i.e. recombination through defects).

1.3.1 Radiative Recombination

Radiative recombination (also called *band-to-band* recombination) is the inverse mechanism of the light absorption. It occurs when an excited electron falls back to its previous energy and recombine with a hole emitting a photon in the process (see fig.1.5)

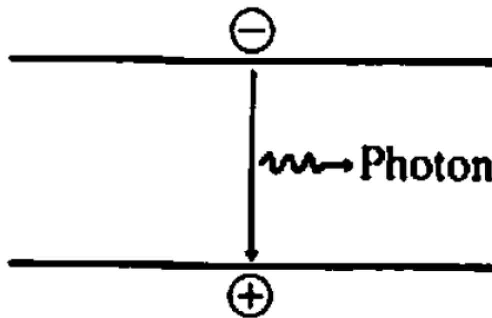

Fig. 1.5 Radiative recombination mechanism. An electron in conduction band recombines with an hole in the valence emitting a photon in the process

In a direct bandgap semiconductor the energy of the emitted photon is the same than the energy difference before and after the transition, i.e. the bandgap E_g. In an indirect bandgap semiconductor the process will involve also the energy of a phonon, thus in silicon this recombination is much less probable than the other types. The radiative recombination rate per unit time and volume is expressed as:

$$U_{rad} = Bnp = B(n_0 + \Delta n)(p_0 + \Delta p) \tag{1.2}$$

where B is a semiconductor dependent constant, n and p are the total concentrations of electrons and holes, n_0 and p_0 are the concentration of electron and holes in dark (due to doping) and Δn and Δp are the excess

concentrations of electrons and holes respectively (due to light generation). The low value of B measured for silicon ($9.5 \times 10^{-15}\ cm^3/s$) shows the low probability of this recombination to happen [16]. Following eq. (1.1) and eq. (1.2) the lifetime due to radiative recombination can be expressed as:

$$\tau_{rad} = \frac{\Delta n}{B(n_0 + \Delta n)(p_0 + \Delta p)} \tag{1.3}$$

In low injection level (LLI) conditions (where Δn,$\Delta p << n_0, p_0$) in an *n-type* semiconductor (where $p_0 << n_0$) the lifetime due to radiative recombination is expressed as:

$$\tau_{rad,LLI} = \frac{1}{Bn_0} \tag{1.4}$$

A similar equation can be written for *p-type* semiconductors.

1.3.2 Auger Recombination

Auger recombination is similar to radiative recombination, except that the transition energy is given to another carrier (in either the conduction or the valence band). The electron (or hole) that receive the excess energy than releases it through lattice interaction with phonons (see fig. 1.6).

Auger recombination is particularly important in highly doped material (i.e. when the doping concentration is higher than $10^{17} cm^{-3}$) and is one of the main loss mechanisms in the highly doped regions of a solar cell.
The Auger recombination rate can be expressed as:

$$U_{Auger} = (C_n n + C_p p)(pn - n_i^2) \tag{1.5}$$

where C_n and C_p are temperature dependent coefficients. Eq. (1.5) can be simplified if we assume low injection conditions and that C_n and C_p are of similar magnitude. In terms of effective lifetime from Auger recombination

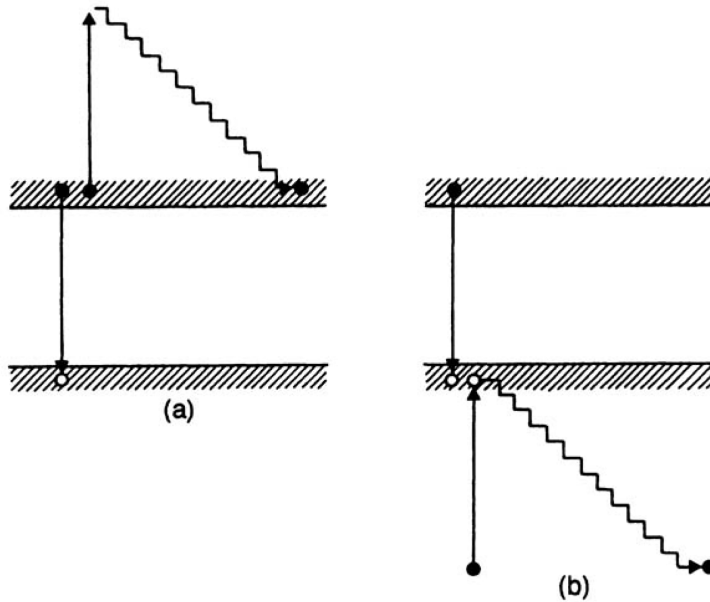

Fig. 1.6 Auger recombination mechanism in conduction (a) and valence (b) band. An electron in conduction band gives its excess energy to another electron and recombines with a hole. The excited electrons releases its energy through lattice interactions. Same process occurs in the valence band for holes.

we can write:

$$\tau_{Auger} = \frac{1}{C_n n_0^2} \tag{1.6}$$

for a n-type semiconductor. A similar expression can be derived for p-type semiconductors.

1.3.3 Shockley-Read-Hall recombination

Lifetime in a semiconductor is fundamentally determined by the presence of impurities and defects in the crystal. These imperfections lead to the creation of energy levels inside the otherwise forbidden band gap. These impurity levels act like traps for charge carriers and then determine the recombination to

a high degree. The theory of this mechanism was developed by Shockley and Read [17], and Hall [18], thus the name of this kind of recombination (often abbreviated in *SRH recombination*). For an energy level in the forbidden band four processes are possible (see fig.1.7):

- an electron is captured by an unoccupied energy level (1)
- an electron is emitted from an occupied level into the conduction band(2)
- a hole is captured by an occupied energy level(3)
- a hole is emitted into an unoccupied state in the valence band(4)

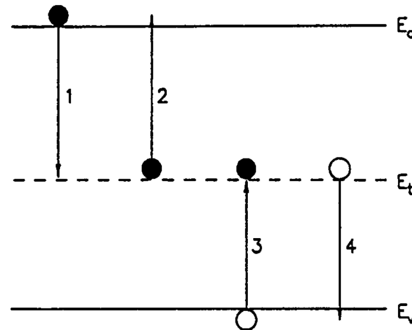

Fig. 1.7 SRH recombination by defect levels

Calculating the corresponding probabilities for these processes we may find the following relationship for the recombination rate ($s^{-1}cm{-}3$) associated with SRH recombination:

$$U_{SRH} = \frac{V_{th}N_t(np - n_i^2)}{(1/\sigma_p)(n+n_1) + (1/\sigma_n)(p+p_1)} \tag{1.7}$$

where

Vth is the thermal velocity,

N_t is the density of traps,
σ_n is the capture cross section for the electrons,
σ_p is the capture cross section for the holes.
The variables n_1 and p_1 mean

$$n_1 = n_i^{\left(\frac{E_t - E_i}{kT}\right)} \tag{1.8}$$

and

$$p_1 = n_i^{\left(\frac{E_i - E_t}{kT}\right)} \tag{1.9}$$

where E_t is the energy of the defect level. V_{th} is about $10^7 cm/s$ at 300K and typical values for σ_n and σ_p are $10^{-15} cm^2$. It is worth noting that the maximum net recombination rate occurs when E_t is exactly in the mid of the band gap, for which there is the highest probability of transition. For crystalline silicon the single level trap approximation can be used whereas for material like amorphous silicon, in which there is a continuous energy level distribution of defects, a more extended SRH modeling is needed. The SRH lifetime can be expressed as:

$$\tau_{SRH} = \frac{1}{\sigma V_{th} N_t} \tag{1.10}$$

Therefore carrier lifetime inside the semiconductor may be heavily decreased through SRH recombination by large capture cross section, high thermal velocities and large trap densities. It has been shown that SRH recombination can be also dependent one the substrate doping level [19] and this has been taken in account in the simulation of the device by using the Scharfetter relation [11]:

$$\tau_{SRH,dop} = \tau_{min} + \frac{\tau_{max} - \tau_{min}}{1 + (\frac{N_A + N_D}{Nref})^{\gamma}} \tag{1.11}$$

where γ and N_{ref} are fit parameters, τ_{max} and τ_{min} are the best and worst case carrier lifetimes and N_A and N_D are the bulk acceptor and donor concentrations.

A particular type of SRH recombination occurs at the interface between two materials or two grain boundaries of one material. Dangling bonds at the interfaces creates energy level for traps in the band gap. The net expression for surface SRH recombination due to all the surface defect states is given by [11]

$$U_{SRH,surf} = \frac{np - n_i^2}{(n+n_1)/s_p + (p+p_1)/s_n} \tag{1.12}$$

where

$$n_1 = n_{i,eff} e^{\frac{E_{trap}}{kT}} \tag{1.13}$$

and

$$p_1 = n_{i,eff} e^{\frac{-E_{trap}}{kT}} \tag{1.14}$$

s_n and s_p are the doping dependent surface recombination velocities for electron and holes respectively. The net recombination rate due to all types of recombination mechanisms if found by summing the rates of the individual processes:

$$U_{Total} = U_{rad} + U_{Auger} + U_{SRH} \tag{1.15}$$

and the effective total lifetime is given by:

$$\frac{1}{\tau_{eff}} = \frac{1}{\tau_{rad}} + \frac{1}{\tau_{Auger}} + \frac{1}{\tau_{SRH}} \tag{1.16}$$

1.4 Carrier transport inside a semiconductor

After their generation due to light absorption, charge carriers move inside the material and must be collected before their recombination in order to extract power from a solar cell. Charge carriers inside a semiconductor follow the so-called Drift-Diffusion model.

1.4.1 Drift-Diffusion Model

The two driving forces of motion for carriers are the diffusion due to different concentration inside the material and the drift due to the interaction with the electrical field. In absence of external forces electrons and holes move from regions of high concentration to region of low concentration creating a flux that tends to distribute evenly the carriers in the material. This diffusion current is proportional to the gradient of the carrier density and can be written as:

$$\mathbf{J}_p = -qD_p \bigtriangledown p \tag{1.17}$$

for holes and

$$\mathbf{J}_n = qD_n \bigtriangledown n \tag{1.18}$$

for electrons. D_p and D_n are the diffusion coefficient for holes and electrons respectively. When an electric field $\mathbf{E}$ is applied on an uniformly doped semiconductor there is a bending in the energy bands in the direction of the applied field. Electrons in the conduction band move in the opposite direction of the field and holes in the valence band in the same direction (see fig. 1.8) [12]. During their motion, carriers are scattered by many objects such as lattice atoms, dopant ions, crystal defects and even other electrons and holes. The final results is a bouncing movement in the direction forced by the electric field $\mathbf{E} = -\bigtriangledown\phi$, where ϕ is the electrostatic potential. The net effect on macroscopic scale is a movement at constant velocity, v_d, called drift velocity. Drift velocity is directly proportional to the electrical field

$$|\mathbf{v}_d| = |\mu\mathbf{E}| = |\mu\bigtriangledown\phi| \tag{1.19}$$

where μ is the carrier mobility. Carrier mobility is in general independent of the electric field strength until very high values, not reached in the typical solar cell operation range. The most relevant scattering mechanisms in solar cell are lattice and ionized impurities scattering and their effect on mobility

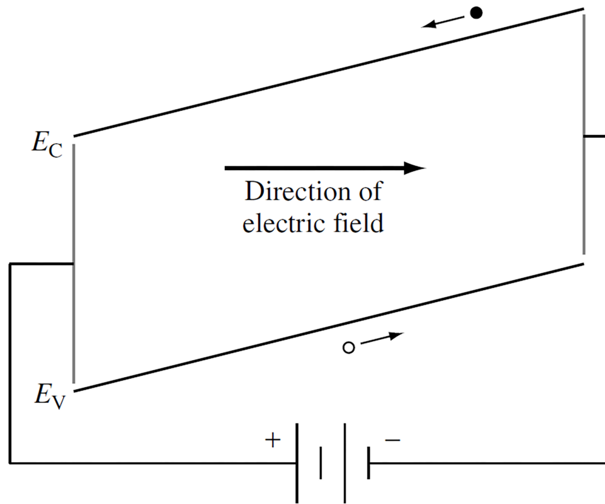

Fig. 1.8 Band bending and drift movement in semiconductor

can be approximated as

$$\mu_L = C_L T^{-3/2} \tag{1.20}$$

and

$$\mu_I = \frac{C_I T^{-3/2}}{N_D^+ + N_A^-} \tag{1.21}$$

These can be combined using Mathiessen's rule to give the carrier mobility [20]:

$$\frac{1}{\mu} = \frac{1}{\mu_L} + \frac{1}{\mu_I} \tag{1.22}$$

In modeling of solar cells Klaassens unified mobility model is often used because is more precise, taking in account phonon scattering, impurity scattering but also carrier-carrier scattering [21].
The drift currents for holes and electrons can be written as:

$$\mathbf{J}_p = qp\mathbf{v}_{d,p} = q\mu_p p\mathbf{E} = -q\mu_p p \bigtriangledown \phi \tag{1.23}$$

and

$$\mathbf{J}_n = -qn\mathbf{v}_{d,n} = q\mu_n n\mathbf{E} = -q\mu_n n\bigtriangledown\phi \tag{1.24}$$

In thermal equilibrium a net current of electrons or holes is not possible, therefore the drift and diffusion currents must balance perfectly. This leads to the Einstein relationship for non degenerate materials:

$$\frac{D}{\mu} = \frac{kT}{q} \tag{1.25}$$

The total holes and electrons current are the sum of the respective drift and diffusion components:

$$\mathbf{J}_p = q\mu_p p\mathbf{E} - qD_p\bigtriangledown p = -q\mu_p p\bigtriangledown\phi - qD_p\bigtriangledown p \tag{1.26}$$

$$\mathbf{J}_n = q\mu_n n\mathbf{E} + qD_n\bigtriangledown n = -q\mu_n n\bigtriangledown\phi + qD_n\bigtriangledown n \tag{1.27}$$

The total current than is:

$$\mathbf{J} = \mathbf{J}_p + \mathbf{J}_n + \mathbf{J}_{disp} \tag{1.28}$$

where $\mathbf{J}_{disp}$ is the displacement current given by:

$$\mathbf{J}_{disp} = \varepsilon\frac{\partial\mathbf{D}}{\partial t} \tag{1.29}$$

where ε is the electric permittivity of the semiconductor. The displacement current is typically neglected in solar cells since they are static (DC) devices.

1.4.2 Semiconductor Equations

In order to describe the transport of carriers inside a semiconductor we need to know the dependence of the concentrations of electrons and holes from position and time ($n(\mathbf{r},t)$ and $p(\mathbf{r},t)$) and the spatial distribution of the electric

field $\mathbf{E}(\mathbf{r})$. Two equations can be used to describe these relations. Under quasi-stationary conditions, Poisson equation links the spatial charge density and the electrical potential:

$$\bigtriangledown \cdot \varepsilon \mathbf{E} = q(p - n + N) \tag{1.30}$$

where N is the net charge in the substrate due to dopants and trapped charges. The second equation is the continuity equation, that takes in account the law of conservation of charge. The continuity equations for holes and electrons are:

$$\bigtriangledown \cdot \mathbf{J}_p = q(G - R_p - \frac{\partial p}{\partial t}) \tag{1.31}$$

$$\bigtriangledown \cdot \mathbf{J}_n = q(R_n - G + \frac{\partial n}{\partial t}) \tag{1.32}$$

where G is the optical generation rate of electron-hole pairs and R_p and R_n are the recombination rates for holes and electrons respectively. For an uniformly doped semiconductor, band gap, electric permittivity, mobility and diffusion coefficients are independent of position. Therefore semiconductor equations can be reduced to:

$$\frac{d\mathbf{E}}{dx} = \frac{q}{\varepsilon}(p - n + N_D - N_A) \tag{1.33}$$

$$q\mu_p \frac{d}{dx}(p\mathbf{E}) - qD_p \frac{d^2 p}{dx^2} = q(G - R) \tag{1.34}$$

$$q\mu_n \frac{d}{dx}(n\mathbf{E}) + qD_n \frac{d^2 n}{dx^2} = q(R - G) \tag{1.35}$$

In regions far enough from the junction, where the electric field is very small, under low-level injection conditions ($\Delta p = \Delta n << N_D, N_A$), R simplifies as:

$$R = \frac{\Delta n_P}{\tau_n} \tag{1.36}$$

in the p-type region and to

$$R = \frac{\Delta p_N}{\tau_p} \tag{1.37}$$

in the n-type region, where Δp_N and Δn_P are the excess minority carrier concentrations. Eq. (1.34) and eq. (1.35) thus can be reduced to:

$$D_p \frac{d^2 \Delta p_N}{dx^2} - \frac{\Delta p_N}{\tau_p} = -G(x) \tag{1.38}$$

in n-type material and

$$D_n \frac{d^2 \Delta n_P}{dx^2} - \frac{\Delta n_P}{\tau_n} = -G(x) \tag{1.39}$$

in p-type material. These equations are called *minority-carrier diffusion equations* and are often used in the analysis of semiconductor device operations.

1.5 *pn*-junction electrostatic model

The very base of a solar cell is the so-called *pn-junction*, i.e. the junction of two oppositely doped silicon blocks. In thermal equilibrium, when a p-type semiconductor and an n-type semiconductor are placed together, no net current can flow and Fermi energy level must be the same independently of the position. This determines a bending in the energy levels of the structure (see fig. 1.10(a)). The different concentration of holes and electrons inside the semiconductor create a flow of carriers due to diffusion, electrons move in the p-type region and holes in the n-type region. When the carriers diffuse, they leave behind the charged impurities due to doping (acceptors in the p-type material and donors in the n-type material), no longer electrically screened. This net charge difference inside the material give rise to an electrical field (or electrostatic potential difference, called *built-in voltage* V_{bi}), which limits the carrier diffusions between the two regions.

In thermal equilibrium drift and diffusion currents of electrons and holes balance exactly and there is no net current flow. The transition region between the p-type and n-type semiconductor, where the electric field is present, is called *space-charge region* or *depletion region*, since it's depleted of electrons and holes, drifted away by the field. If the p-type and n-type regions are thick

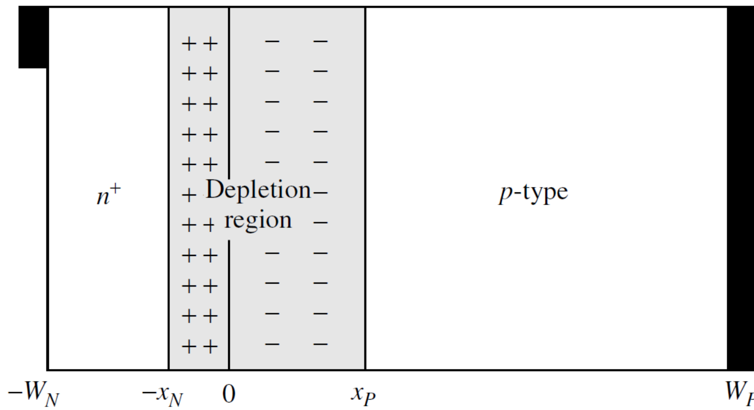

Fig. 1.9 Simple solar cell schematic (1D abrupt pn-junction). Front contact is on the n-type side, back contact on the p-type side. The junction is in $x = 0$, and the depletion region extends from $-x_N$ to x_P.

enough, the regions on either sides of the depletion region are charge-neutral and called *quasi-neutral regions*.

A simple 1D pn-junction, representative of a simple solar cell, is showed in fig. 1.9. In this case the n-type region is much more doped than the p-type region, so the depletion zone extends for the majority in the p-type side and the junction is called *abrupt*. The external contacts of the solar cell are showed on both sides of the junction, the front contact on the n-type side (usually called *emitter*) and the rear contact on the p-type side (also called *base*).

The electrostatic of the junction can be described with Poisson equation:

$$\nabla^2 \phi = \frac{q}{\varepsilon}(n_0 - p_0 + N_A^- - N_D^+) \tag{1.40}$$

where ϕ is the electrostatic potential, n_0 and p_0 are the equilibrium concentrations of electrons and holes, N_A^- is the ionized acceptor concentration and N_D^+ is the ionized donor concentration.
Inside the depletion region ($-x_N < x < x_P$) n_0 and p_0 can be neglected so eq. (1.40) can be simplified to:

$$\nabla^2\phi = -\frac{q}{\varepsilon}N_D^+, \qquad \text{for } -x_n < x < 0 \text{ and} \tag{1.41a}$$

$$\nabla^2\phi = \frac{q}{\varepsilon}N_A^-, \qquad \text{for } 0 < x < x_p. \tag{1.41b}$$

Outside the depletion region, assuming charge neutrality

$$\nabla^2\phi = 0, \qquad \text{for } x \leq -x_N \text{ and } x \geq x_P. \tag{1.42}$$

The built-in voltage V_{bi} can be obtained integrating the electric field inside the depletion zone, $\mathbf{E} = -\nabla\phi$

$$\int_{-x_N}^{x_P} \mathbf{E}dx = -\int_{-x_N}^{x_P} \frac{d\phi}{dx}dx = -\int_{V(-x_N)}^{V(x_P)} d\phi = \phi(-x_N) - \phi(x_P) = V_{bi} \tag{1.43}$$

Solving equations (1.41) and (1.42) (with $\phi(x_p)$=0) we obtain the distribution of the electrostatic potential:

$$\phi(x) = \begin{cases} V_{bi}, & x \leq -x_N \\ V_{bi} - \dfrac{qN_D}{2\varepsilon}(x+x_N)^2, & -x_N < x \leq 0 \\ \dfrac{qN_A}{2\varepsilon}(x-x_P)^2, & 0 \leq x < x_P \\ 0, & x \geq x_P \end{cases} \tag{1.44}$$

In $x = 0$ the potential and the electric field must be continuous (see fig. 1.10(b)), so from eq. (1.44):

$$V_{bi} - \frac{qN_D}{2\varepsilon}x_N^2 = \frac{qN_A}{2\varepsilon}x_P^2 \tag{1.45}$$

and

$$x_N N_D = x_P N_A \tag{1.46}$$

Eq. (1.46) shows that the net charge of the two sides of the space-charge region is zero, so the depletion region extends furthest in the lightly doped side (see fig. 1.10(c)). From equations (1.45) and (1.46) the depletion zone width W_D in equilibrium conditions can be derived:

$$W_D = x_N + x_P = \sqrt{\frac{2\varepsilon}{q}\left(\frac{N_A + N_D}{N_A N_D}\right) V_{bi}} \tag{1.47}$$

If an external voltage V is applied, the depletion region width will be dependent on it:

$$W_D = x_N + x_P = \sqrt{\frac{2\varepsilon}{q}\left(\frac{N_A + N_D}{N_A N_D}\right)(V_{bi} - V)} \tag{1.48}$$

V_{bi} can be calculated taking in account that under thermal equilibrium the net hole and electron currents are zero.

$$q\mu_p p_0 \mathbf{E} = qD_p \bigtriangledown p \tag{1.49}$$

Using Einstein relation, in one dimension the electric field is:

$$E = \frac{kT}{qp_0}\frac{dp_0}{dx} \tag{1.50}$$

Integrating the electric field of eq. (1.50) in the depletion region using eq. (1.43) we can find the expression for the built-in potential:

$$V_{bi} = \frac{kT}{q} ln \left[\frac{N_D N_A}{n_i^2}\right] \tag{1.51}$$

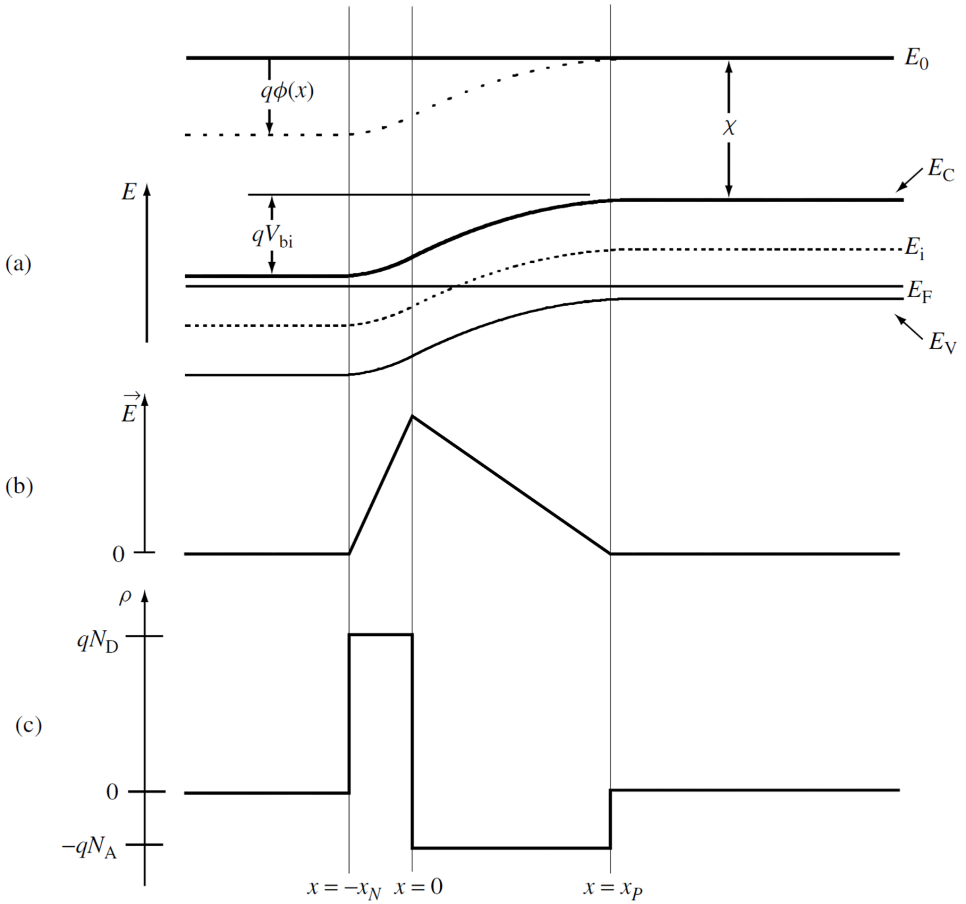

Fig. 1.10 *pn*-junction equilibrium conditions. (a) Energy bands diagram: E_c, E_i, E_F and E_V are the conduction band energy, the intrinsic energy level, the Fermi energy level and the valence band energy level, respectively. E_0 is the vacuum energy and χ the electron affinity. (b) Electric field in the semiconductor. (c) Charge density in the semiconductor.

1.6 Solar cell characteristics and figures of merit

The basic current-voltage characteristic of a solar cell can be obtained by solving the minority carrier equation for a *pn*-junction with specific boundary conditions.

1.6.1 Boundary conditions and I-V characteristic

In order to define the conditions at the edges of the cell (for $x = -W_N$ and $x = W_P$, where the metal contacts are placed) we need to do some considerations. On the front side, in a conventional solar cell, only a small fraction of the surface is covered with the metal contact, in fact the smallest possible, in order to reduce the amount of light that cannot penetrate in the base. In addition, for the opposite reason, i.e to increase the light absorption, usually the front surface is coated with an anti-reflective layer (SiO_2 or other materials) and textured with a pattern. Therefore, if in the case of a simple metallic contact the excess minority carrier at the surface would be zero, in a real solar cell the boundary condition in $x = -W_N$ is:

$$\left.\frac{d\Delta p}{dx}\right|_{x=-W_N} = \frac{S_{F,eff}}{D_p}\Delta p(-W_N) \tag{1.52}$$

where $S_{F,eff}$ is the effective surface recombination velocity on the front. The back side (in $x = W_P$), not exposed to light, could be actually completely covered with a metallic contact and thus, even in this case, the excess minority carrier concentration on the surface would be zero. However, solar cells are often fabricated with a *back-surface field* (BSF), a thin more heavily doped layer at the edge of the base region. This layer creates an energy bands bending, that helps to keep the minority carriers away from the contact and increases the possibility for them to be collected. Therefore the boundary

condition in $x = W_P$ is:

$$\left.\frac{d\Delta n}{dx}\right|_{x=W_P} = \frac{S_{B,eff}}{D_n}\Delta n(W_P) \tag{1.53}$$

where $S_{B,eff}$ is the effective surface recombination velocity on the back. Under non-equilibrium conditions in a non-degenerate semiconductor and low-level injection, we can assume that quasi-Fermi energies (F_P and F_N) are constant inside the depletion region,

$$qV = F_N(x) - F_P(x) \qquad \text{for } -x_N \leq x \leq x_P \tag{1.54}$$

Carrier concentrations can be expressed in function of the quasi-Fermi energies:

$$p = n_i^{(E_i - F_P)/kT} \tag{1.55}$$

and

$$n = n_i^{(F_N - E_i)/kT} \tag{1.56}$$

Using equations (1.54), (1.55) and (1.56) we can obtain the *law of the junction*, the boundary conditions at the edges of the depletion zone:

$$p_N(-x_N) = \frac{n_i^2}{N_D} e^{qV/kT} \tag{1.57}$$

and

$$n_P(x_P) = \frac{n_i^2}{N_A} e^{qV/kT} \tag{1.58}$$

The last equation needed is the optical generation rate. In a solar cell the rate of generation of electron-hole pairs as a function of position is

$$G(x) = (1-s)\int_\lambda (1-r(\lambda))f(\lambda)\alpha(\lambda)e^{-\alpha(x+W_N)}d\lambda \tag{1.59}$$

where s is the shadowing factor due to front grid, $r(\lambda)$ is the reflectance, $\alpha(\lambda)$ is the absorption coefficient, $f(\lambda)$ is the incident photon flux(number of incident photons per unit are per second per wavelength) and the light is supposed to be incident at $x=0$. Only photons with wavelength $\lambda \leq hc/Eg$ contribute to the optical generation rate. We can solve the minority carrier diffusion equation (1.38) by using the boundary conditions defined in equations (1.52), (1.53), (1.57) and (1.58) and the generation rate defined in eq. (1.59) to obtain:

$$\Delta p_N(x) = C_{N,1}\, sinh\left[\frac{x+x_N}{L_p}\right] + C_{N,2}\, cosh\left[\frac{x+x_N}{L_p}\right] + \Delta p'_N(x) \tag{1.60}$$

in the n-type region and

$$\Delta n_P(x) = C_{P,1}\, sinh\left[\frac{x-x_P}{L_n}\right] + C_{P,2}\, cosh\left[\frac{x-x_P}{L_n}\right] + \Delta n'_P(x) \tag{1.61}$$

in the p-type region. L_p and L_n are the diffusion lengths for holes and electrons defined as:

$$L_p = \sqrt{D_p \tau_p} \tag{1.62}$$

and

$$L_n = \sqrt{D_n \tau_n} \tag{1.63}$$

The terms $\Delta p'_N(x)$ and $\Delta n'_P(x)$ are particular solutions associated with $G(x)$, given by:

$$\Delta p'_N(x) = -(1-s)\int_\lambda \frac{\tau_p}{(L_p^2\alpha^2-1)}[1-r(\lambda)]f(\lambda)\alpha(\lambda)e^{-\alpha(x+W_N)}d\lambda \tag{1.64}$$

and

$$\Delta n'_P(x) = -(1-s)\int_\lambda \frac{\tau_n}{(L_n^2\alpha^2-1)}[1-r(\lambda)]f(\lambda)\alpha(\lambda)e^{-\alpha(x+W_N)}d\lambda \tag{1.65}$$

The coefficients $C_{N,1}$, $C_{N,2}$, $C_{P,1}$ and $C_{P,2}$ can be obtained using the boundary conditions.
In the quasi-neutral regions, since the electric field is negligible, minority carrier current densities are just the diffusion currents:

$$\mathbf{J}_{p,N}(x) = -qD_p \frac{d\Delta p_N}{dx} \tag{1.66}$$

and

$$\mathbf{J}_{n,P}(x) = qD_n \frac{d\Delta n_P}{dx} \tag{1.67}$$

The total current of the cell is given by:

$$I = A[J_p(x) + J_n(x)] \tag{1.68}$$

where A is the area of the solar cell. Equations (1.66) and (1.67) don't give the hole and electron currents in the same point, but we can integrate the electron continuity equation (1.32) over the depletion region to obtain:

$$\mathbf{J}_n(-x_N) = \mathbf{J}_n(x_P) + q\int_{-x_N}^{x_P} G(x)dx - q\int_{-x_N}^{x_P} R(x)dx \tag{1.69}$$

Assuming a constant recombination rate in the depletion region $R(x_m)$ where x_m is the point of maximum recombination ($p_D(x_m) = n_D(x_m)$) and a midgap single level trap recombination, from equations (1.7), (1.54), (1.55), (1.56) the recombination rate in the depletion region is:

$$R_D = \frac{n_i(e^{qV/2kT} - 1)}{\tau_D} \tag{1.70}$$

where τ_D is the effective lifetime in the depletion region.
Expanding equation (1.69) we can obtain:

$$\begin{aligned}\mathbf{J}_n(-x_N) &= \mathbf{J}_n(x_P) + q\int_{-x_N}^{x_P} G(x)dx - q\int_{-x_N}^{x_P} R_D dx \\ &= \mathbf{J}_n(x_P) + q(1-s)\int_{\lambda}[1-r(\lambda)]f(\lambda)[e^{-\alpha(W_N - x_N)} - e^{-\alpha(W_N + x_P)}]d\lambda \\ &\quad - q\frac{W_D n_i}{\tau_D}(e^{qV/2kT} - 1) \\ &= \mathbf{J}_n(x_P) + J_D - q\frac{W_D n_i}{\tau_D}(e^{qV/2kT} - 1)\end{aligned} \tag{1.71}$$

where $W_D = x_P + x_N$ and J_D is the generation current from the depletion region. Substituting in eq. (1.68):

$$I = A[J_p(-x_N) + J_n(x_P) + J_D - q\frac{W_D n_i}{\tau_D}(e^{qV/2kT} - 1)] \tag{1.72}$$

The last term is the recombination rate inside the depletion region. Using equation (1.60), (1.61) it is possible to evaluate the minority carrier current densities in eq. (1.66), (1.67). Then these can be substituted in eq. (1.72) to finally obtain the general *I-V* characteristic for a solar cell:

$$I = I_{SC} - I_{o1}(e^{qV/kT} - 1) - I_{o2}(e^{qV/2kT} - 1) \tag{1.73}$$

where I_{SC} is called *short-circuit current* and is the sum of all the contributions from each region (*n*-type region, depletion region and *p*-type region).

$$I_{SC} = I_{SCN} + I_{SCD} + I_{SCP} \tag{1.74}$$

The detailed equations of the three components can be found in [12].

1.6.2 Solar cell figures of merit

Equation (1.73) is the main I-V characteristic of a solar cell.

$$I = I_{SC} - I_{o1}(e^{qV/kT} - 1) - I_{o2}(e^{qV/2kT} - 1) \tag{1.75}$$

The term I_{SC} represents the polarization factor due to light generated current. The terms I_{o1} and I_{o2} represents the dark saturation currents in the quasi-neutral regions and in the depletion zone, respectively. From a circuital point of view this expression can be transposed in the schematic of fig 1.11. It is

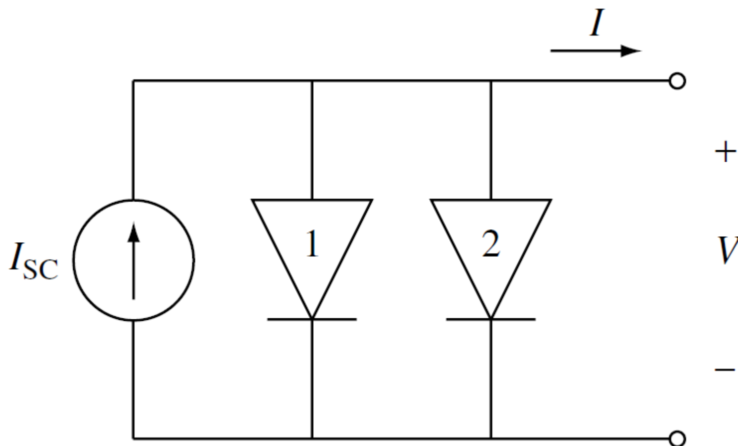

Fig. 1.11 Schematic equivalent circuit for a solar cell. Diode 1 represents the recombination current in the quasi-neutral regions, while diode 2 the recombination in the depletion region.

worth noting that the two diodes have a different ideality factor, 1 for the diode representing recombination in the quasi-neutral zones and 2 for the diode representing recombination in the depletion region. The second diode is commonly neglected especially for high bias voltages. The typical I-V curve of a solar cell is show in fig. 1.12. V_m and I_m denote the maximum output

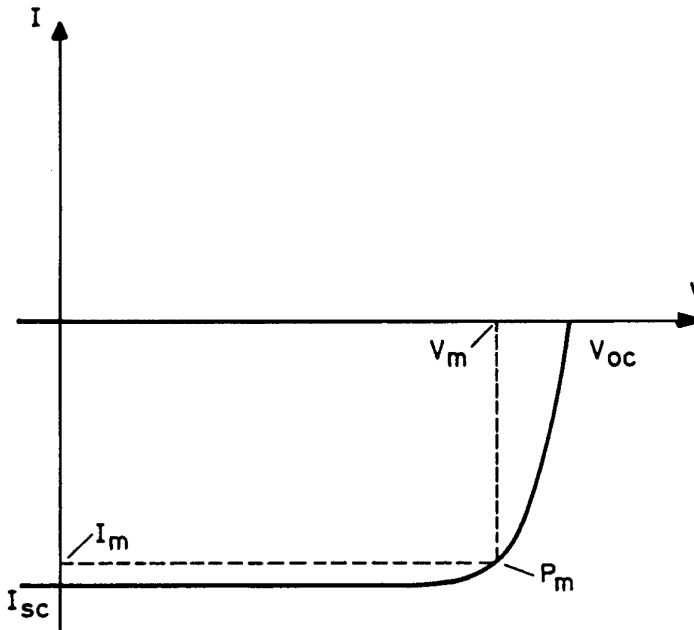

Fig. 1.12 Voltage-current characteristic of a solar cell. P_m is the point where the output power is maximum. I_{SC} is the maximum current (short-circuit current) and V_{OC} is the maximum voltage (open circuit voltage).

power voltage and current, respectively. At $V = V_m$, $I = I_m$ corresponds the maximum power point $P_m = V_m I_m$, i.e. the value of the maximum power that can be drawn from the cell. The maximum current of the cell is for $V = 0$ in equation (1.75), i.e the short circuit current I_{SC}. In open circuit condition ($I = 0$) all the light generated current I_{SC} flows through the diode 1 so the *open-circuit voltage* V_{OC} is defined as:

$$V_{OC} \approx \frac{kT}{q}\, ln\, \frac{I_{SC}}{I_{o1}} \tag{1.76}$$

where $I_{SC} >> I_{o1}$. The third figure of merit is the so called *fill factor*. It is a measure of the squareness of the I-V characteristic and is always less than one. It is the ratio of the maximum power rectangle with respect to the rectangle

defined by I_{SC} and V_{OC} and is defined as:

$$FF = \frac{P_m}{I_{SC}V_{OC}} = \frac{I_m V_m}{I_{SC}V_{OC}} \tag{1.77}$$

Finally, the most important figure of merit of a solar cell is its power conversion *efficiency*, η, defined as the ratio of the maximum output power to the incident power:

$$\eta = \frac{P_m}{P_{in}} = \frac{FF V_{OC} I_{SC}}{P_{in}} \tag{1.78}$$

1.6.3 Other figures of merit

Short-circuit current, open-circuit voltage and fill factor are not always sufficient to understand the main sources of losses inside a solar cell, since they may provide partial informations about the light absorption process and some of the recombination mechanisms. Therefore some other figures of merit can be used in the performance analysis. From the optical point of view is very important to understand the fraction of light that is actually absorbed by the cell. A part of the total incident light can be reflected, depending on the incident surface properties, or transmitted trough the cell without being absorbed (whether for not being enough energetic or for a too short optical path). The parameters that describe these phenomena can be defined as:

$$R(\lambda) = \frac{P_{refl}}{P_{in}} \qquad \textit{Reflectance} \tag{1.79}$$

$$T(\lambda) = \frac{P_{tran}}{P_{in}} \qquad \textit{Transmittance} \tag{1.80}$$

where P_{in} is the incident power and P_{refl} and P_{tran} the portion of incident light power reflected and transmitted, respectively. To satisfy the optical

conservation law the total power must be conserved so:

$$R(\lambda)+T(\lambda)+A(\lambda)=1 \tag{1.81}$$

where $A(\lambda)$ is the fraction of incident light absorbed.

External and Internal quantum efficiencies

The external quantum efficiency (EQE) is defined as the ratio, at a specific photon energy, of the carriers contributing to current in short-circuit condition and the total number of incident photons.

$$EQE(\lambda)=\frac{J_{SC}(\lambda)}{qf(\lambda)} \tag{1.82}$$

where J_{SC} is the short-circuit current density per unit area and f is the incident photon flux (per unit area per second). If all photons of a specific energy are absorbed and the correspondent generated carriers are collected, then the EQE for that specific wavelength is unity. The internal quantum efficiency (IQE) takes in account only the photons that are actually absorbed inside the cell and relates them to the light generated current:

$$IQE(\lambda)=\frac{EQE(\lambda)}{1-R(\lambda)-T(\lambda)} \tag{1.83}$$

The IQE is always higher than the EQE. From the IQE is possible to retrieve informations about the cell ability to effectively collect the generated carriers, thus informations about the recombination mechanisms, which are one of the main losses in a solar cell.

1.7 Loss mechanisms and temperature effect

There are many causes of losses in the conversion efficiency of a solar cell, someone affecting primarily one the three figures of merit (short-circuit current, open-circuit voltage and fill factor) some others with a mixed effect among them.

1.7.1 Optical losses

The factors that mainly affect the I_{SC} are the optical losses that reduce the photocurrent. The reflection of a portion of the incident light on the silicon surface is one of them, since, on bare flat silicon, is over 30% due to its high refractive index [22]. This problem, though, can be greatly reduced using different techniques, such as application of an anti-reflective layer and surface texturization to increase light trapping. Another source of optical losses is the shadowing due to the presence of the front contact, consisting in a metal grid spreading across the top surface and blocking light. Moreover another portion of incident light may not be absorbed and pass through being lost, or being reflected back by the rear surface and escape from the front, due to a short optical path in thin solar cells (see fig. 1.13).

1.7.2 Recombination Losses

Recombination losses affect both the short-circuit current as well as the open-circuit voltage. In general recombination is defined by the portion of cell in which it occurs, typically on the external surfaces (surface recombination) or in the bulk of the cell (bulk recombination).

Regarding the I_{SC} is important to ensure that the light generated carriers arrive to the junction before recombining. This means the carrier must generate within a diffusion length of the junction and in case of localized high recombination sites (such as the surfaces) this means that the recombination

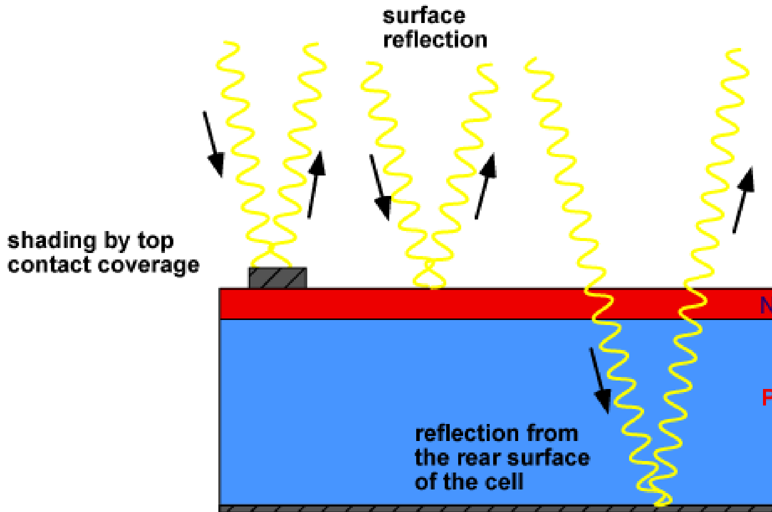

Fig. 1.13 Optical losses in a solar cell. Light can be reflected, blocked by contacts or being reflected from the rear surface without being absorbed.

velocity must be reduced applying a surface passivation layer or a doped layer (called *back-surface field, BSF*) that repels minority carriers.

The V_{OC} is strongly dependent on the diode saturation current I_{o1}. This is controlled by the number of minority carriers at the edge of the junction, how fast they move away and recombine. In terms of recombination, higher diffusion lengths, achieved with lower dopings, are suitable for keeping the V_{OC} higher. The presence of high recombination sites, as the surfaces, will allow carriers to move away from the junction and recombine quickly, dramatically affect the open-circuit voltage. A solution to this problem may be, again, the passivation of the surfaces and the BSF. However, the presence of the BSF, which is a highly doped region, decreases the diffusion length and increases Auger recombination, thus leading to a trade-off between reduced recombination at surfaces and increased recombination in the bulk.

1.7.3 Parasitic resistance effects

The main contribution in Fill Factor degradation is the presence of parasitic resistances which determine series and shunt resistance losses. For a real solar cell eq. (1.75) must be rewritten including the parasitic series resistance R_S and shunt resistance R_{Sh}.

$$I = I'_{SC} - I_{o1}(e^{q(V+IR_S)/kT} - 1) - I_{o2}(e^{q(V+IR_S)/2kT} - 1) - \frac{V - IR_S}{R_{Sh}} \quad (1.84)$$

where I'_{SC} is the short-circuit current without parasitic resistances. The equivalent circuit of fig. 1.11 can be also update to the circuit in fig.

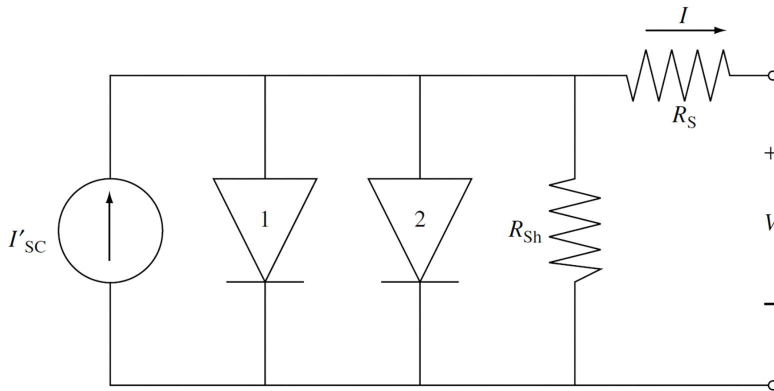

Fig. 1.14 Solar cell equivalent circuit including parasitic series resistance R_S and shunt resistance R_{Sh}.

The series resistance R_S is mainly due to three causes: the current through the emitter and base of the solar cell, the contact resistance between the metal contacts and the silicon and the resistance of the top and rear contacts. In a conventional solar cell the top contact resistance depends both on fingers and bus-bars, while in general is negligible for the back contact, since the back surface is completely metalized. This is not true in case of more complex architecture, such as back-contact or point-contact solar cells [23] .

The lowering of shunt resistance R_{Sh} (which ideally would be infinite) is mainly caused by manufacturing defects, that provide an alternative path for the light generated current causing leakage current across the *p*-*n* junction and on the edges of the device. From eq. (1.84) it is possible to see that the series resistance R_S affects only the maximum short-circuit current, with no effect on the open-circuit voltage. On the contrary, shunt resistance R_{Sh} has no effect on the short-circuit current but reduces the open-circuit voltage. These effects are shown in figures 1.15 and 1.16, respectively.

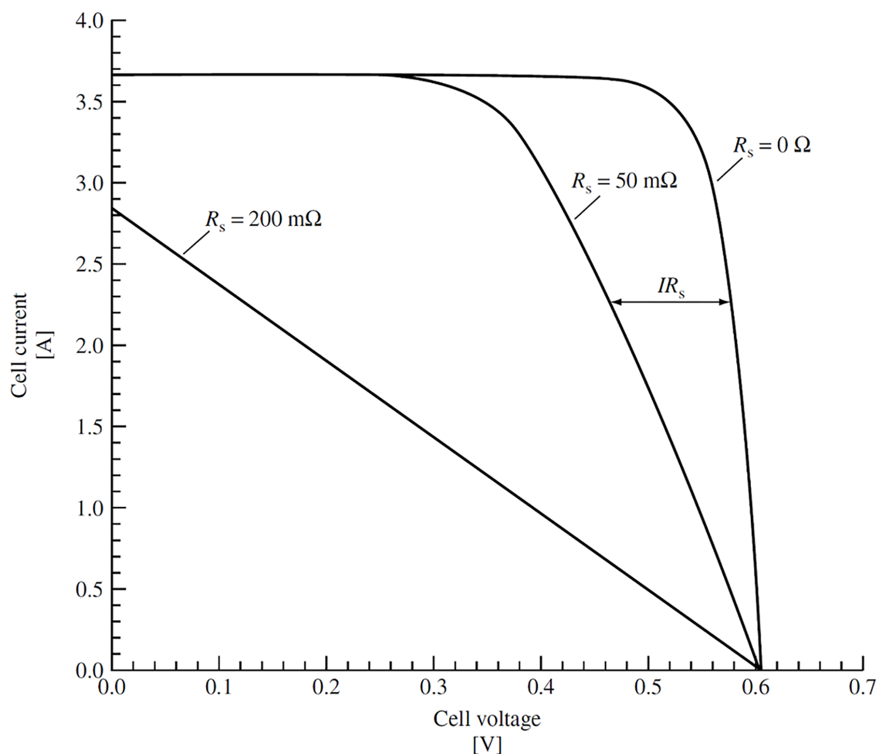

Fig. 1.15 Effect of series resistance on the I-V characteristic of a solar cell ($R_{Sh} = 0$).

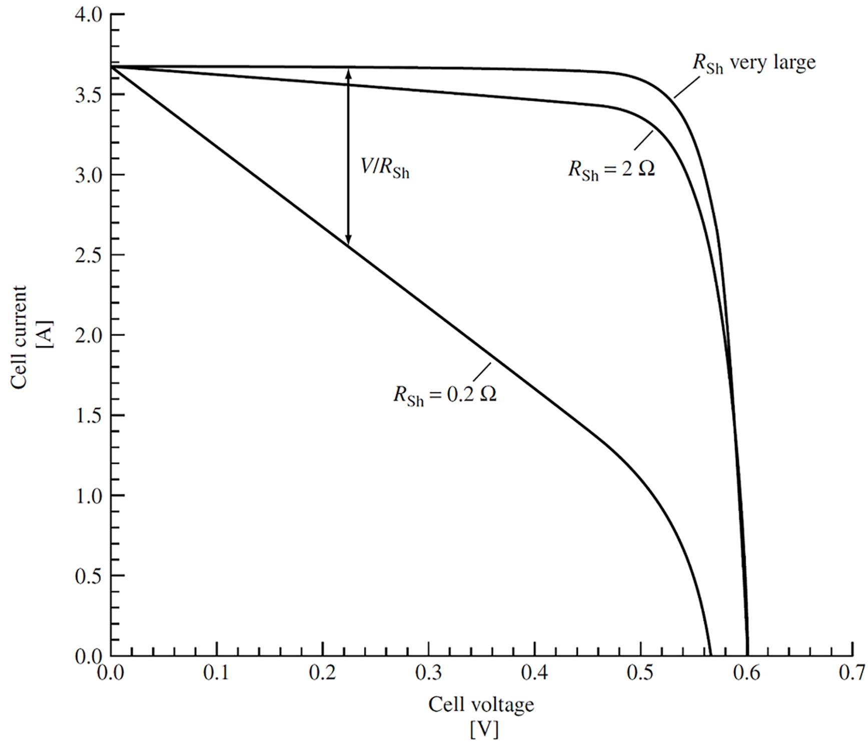

Fig. 1.16 Effect of shunt resistance on the I-V characteristic of a solar cell ($R_S = 0$).

1.7.4 Temperature effect

In eq. (1.75) the parameters I_{o1} and I_{o2} are temperature dependent in the form of [12]:

$$I_{o1} \propto n_i^2 \tag{1.85}$$

and

$$I_{o2} \propto n_i \tag{1.86}$$

If the dark saturation current increases, the open-circuit voltage decreases. The intrinsic carrier concentration n_i is exponentially dependent on the inverse of bandgap (as shown in eq. (1.87)), which is also directly dependent on

temperature.

$$n_i = 2(m_n^* m_p^*)^{3/4} \left(\frac{2\pi kT}{h^2}\right)^{3/2} e^{-E_g/2kT} \tag{1.87}$$

where m_n^* and m_p^* are the effective masses of electrons and holes, respectively, generally considered weakly dependent of temperature. Bandgap decreases as temperature increases, a mechanism called *bandgap narrowing*, following the relation:

$$E_g(T) = E_g(0) - \frac{aT^2}{T+b} \tag{1.88}$$

where a and b are semiconductor specific coefficients. Bandgap narrowing is also doping dependent. If the bandgap decreases, n_i increases thus dark saturation current increases. The dependence of V_{OC} from temperature can be expressed as [24]:

$$\frac{dV_{OC}}{dT} = \frac{\frac{E_g(0)}{q} - V_{OC} + \zeta \frac{kT}{q}}{T} \tag{1.89}$$

where ζ is a temperature dependent parameter. V_{OC} decreases roughly linearly with increasing temperature (for silicon at 300K about -2.3mV/C°). Finally also the absorption coefficient of silicon is temperature dependent as described in [25].

1.8 Limits in conversion efficiency

Sunlight is a very abundant and intense source of energy, however, not all this power can be converted in actual electric output. Since the beginning of photovoltaic studies, efficiency forecasts have been carried out to determine the maximum limit in conversion efficiency. In a milestone paper published in 1961 [26], Shockley and Queisser pointed out, using the detailed balance approach, that the unavoidable ultimate recombination process, counterpart of the generation mechanism, is the main limit for the energy conversion. This

allowed to determine the maximum theoretical limit of efficiency for a single *pn*-junction solar cell, which is 40,7% for the photon spectrum approximated by a black body at 6000K using a fully concentrated design, i.e all the incident light is concentrated on the active area of the cell (see fig. 1.17). In space

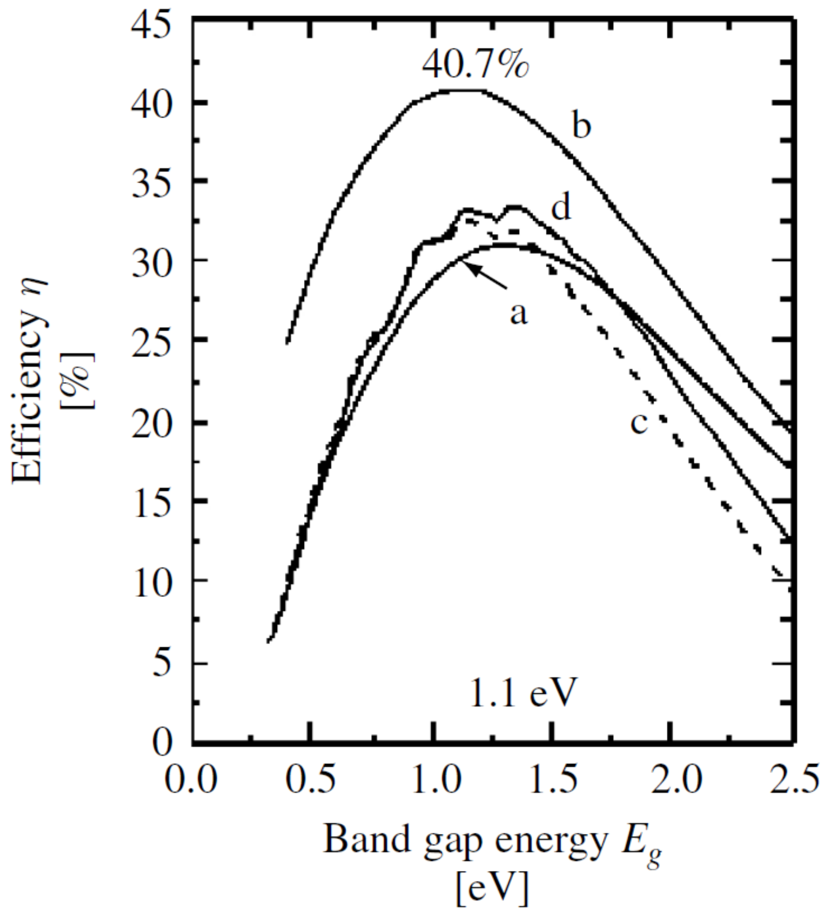

Fig. 1.17 Shockley-Queisser efficiency limits versus bandgap: (a) unconcentrated 6000K black body radiation, (b) fully concentrated 6000K black body radiation, (c) unconcentrated AM1.5-Direct and (d) AM1.5-Global.

the solar spectrum of the sun can be fairly approximated with a black body

emitting at around 6000K [27], but on earth the light spectrum is influenced by latitude and atmosphere. For a single junction solar cell, using the AM1.5 spectrum the maximum efficiency is 33.7% for a material with a bandgap of 1.34 eV. For silicon, however, which has a bandgap of 1.1 eV, this value is lower. For a crystalline silicon solar cell under one sun illumination at 25 °C the maximum theoretical efficiency limit has been recently calculated by Richter *et al.* in 29.43% [28]. The main cause of losses in conversion efficiency is that the main part of incident power is converted in heat, while another relevant portion is not absorbed at all because the photon energy is lower than the bandgap.

The current record for a fabricated c-Si solar cell is 25% efficiency [29], while using a HIT design (heterojunction of crystalline with amorphous silicon) the record has been set by Panasonic to 25.6% [9].

Chapter 2

Solar cell fabrication process and architecture

In this chapter a brief exposition of the fabrication process that leads to the solar cell production will be provided, describing the different steps. In the second part the architecture of a solar cell will be explained, detailing the different regions, and the back-contact solar cell types will be shown.

2.1 Fabrication process

The fabrication of a crystalline silicon solar cell starts with the production of a silicon block of sufficient quality for the proposed target.

Silicon ingots can be created using different methods that leads to different silicon types and grades. In increasing order for quality and cost there are:

(a) Polycrystalline silicon, created using two techniques: Bridgman [30] and block-casting process [31]. This type of silicon offers advantages in terms of lower manufacturing costs at the price of reduced lifetimes. Main problems are the recombination active impurities and extended defects such as grain boundaries and dislocations.

(b) Monocrystalline silicon (c-Si) created with Czochralski (Cz) process [32]. This is the more diffused type of silicon in PV industry, allowing to fabricate cost-effective quantities of Si with sufficient quality.

(c) High quality monocrystalline silicon created using the Float Zone (FZ) process. This kind of silicon, with very low impurities and defects, is typically used in the laboratory top record solar cells, however is quite expensive and less suitable for mass production.

2.1.1 Process flow

The main steps of fabrication of a solar cells are showed in fig. 2.1. Metal contacts are created using screen printing technology, the most common metallization technique for solar cells in PV industry. A description of each step is presented here:

1. **Starting material**: as mentioned before, for mass production the starting material is a slice of silicon, monocrystalline Cz or multicrystalline, in pseudo-square or square shape. The thickness is variable in the order of 200-300 μm. Substrate is usually p-type with resistivity of around 1 $\Omega \cdot cm$.

2. **Saw damage removal**: the cutting process leaves irregular and rough surfaces, that are removed using a bath in alkaline or acid solutions. Around 10 μm of thickness on each side are etched off.

3. **Texturization**: to increase the light trapping and reduce reflections, both sides of the cell are etched using alkaline solutions (NaOH or KOH). Using appropriate temperature, concentration and time parameters for the process, random pyramid patterns are created on both surfaces of the bulk. Since the etching process is based on the crystal orientation of the silicon lattice, for multicrystalline substrate the texturing is carried out using different techniques, such as chemical acidic

texturization [33], mechanical texturization [34], or reactive ion etching (RIE) texturization [35].

4. **Phosphorous diffusion**: the *n*-type dopant used for the creation of the emitter layer is almost always phosphorous. The diffusion process implies the deposition of a phosphorous layer on the surface and then its diffusion inside the bulk by means of heat, thus it requires high temperatures and the absence of impurities at the surfaces. There are different procedures to perform phosphorous diffusion, that can be categorized upon the type of furnace used:

   Quartz furnace: in which the slices of silicon are loaded into an end of a quartz tube using quartz boats, while on the other end dopant gases (usually nitrogen bubbling through liquid $POCl_3$) are inserted. Resistance heaters provide an uniform temperature inside the furnace. Both surfaces and the edge of the wafer are diffused.

   Belt furnaces: in which solid phosphorous sources are used. By chemical vapor deposition (CVD) or other techniques phosphorus compound are applied on one face of the wafer and then the slice of silicon are placed on a conveyor belt passing under resistance or infrared (IR) heater. The temperatures can be adjusted in different zones of the furnace and gases can be supplied.

   Quartz furnaces offer the benefits of cleanliness, since there are no heated metallic elements, while belt furnaces advantages are automation and throughput.

5. **Edge isolation**: if the *n*-layer deposition is performed on both sides of the wafer, a conductive path will be created between the two sides of the cell, resulting in a very low shunt resistance. Therefore the edges of the wafer must be cut off to isolate the junctions. Dry etching, low temperature procedures are used, such as plasma etching or laser cutting [36].

6. **ARC deposition**: an anti-reflective coating (ARC) is a mono or multi-layer of materials deposited on the top surface of the cell (in bifacial cell also on the back). Its purpose is to use light interference properties to reduce the amount of reflected light. The materials employed more often are titanium oxide (TiO_2) and silicon nitride (SiN_x). Techniques used to create the ARC can be atmospheric pressure chemical vapor deposition (APCVD) [37] or spin-on and screen printing.

7. **Front and back contacts creation**: the requirements for metallic contacts of a solar cell are: low resistivity, low contact resistance to silicon, good mechanical adhesion and compatibility with the encapsulation materials. Silver is the most suited material to fulfill these specifications, cause copper may have similar advantages but its high diffusivity can produce contamination during the subsequent steps. Although vacuum evaporation techniques would produce better results, in order to keep the cost as low as possible, the most used metallization method is screen printing. Screen printing is a technology that consist in translating a layer of material in a desired pattern on the surface of the wafer. This is made by using screens, which are fabrics of synthetic or steel wires stretched on an aluminum frame, and pastes, which are compounds of different materials, including solvents, binders and conductive elements [38]. For solar cells, a silver paste is used for creating contacts on the front side (on *n*-type silicon), while a paste formed by a mixture of aluminum and silver is used for the back side (on *p*-type silicon). This is because silver doesn't form ohmic contacts on *p*-type silicon, but aluminum alone cannot be soldered. After the printing pastes must be dried in furnace at 100-200 °C.

8. **Cofiring of metal contacts**: a last high temperature step is required for many reasons. Organic components in the contact pastes must dry out, front metal paste must penetrate the ARC layer to contact the *n*-type emitter while back paste must completely perforate the parasitic *n*-type

layer on the back to contact the base. This is a crucial step, since, if the heat treatment is insufficient, this can lead to high contact resistivity, but if it is too strong, the front contact could penetrate the emitter resulting in a short-circuited cell. Therefore the composition of the pastes and thermal profile of this step must be very carefully adjusted.

9. **Testing**: finally, the cells are tested using a solar simulator, a device that produces an artificial light similar to the solar spectrum and the *I*-*V* characteristics are measured to ensure the cell is not defective and inside the desired tolerance limits.

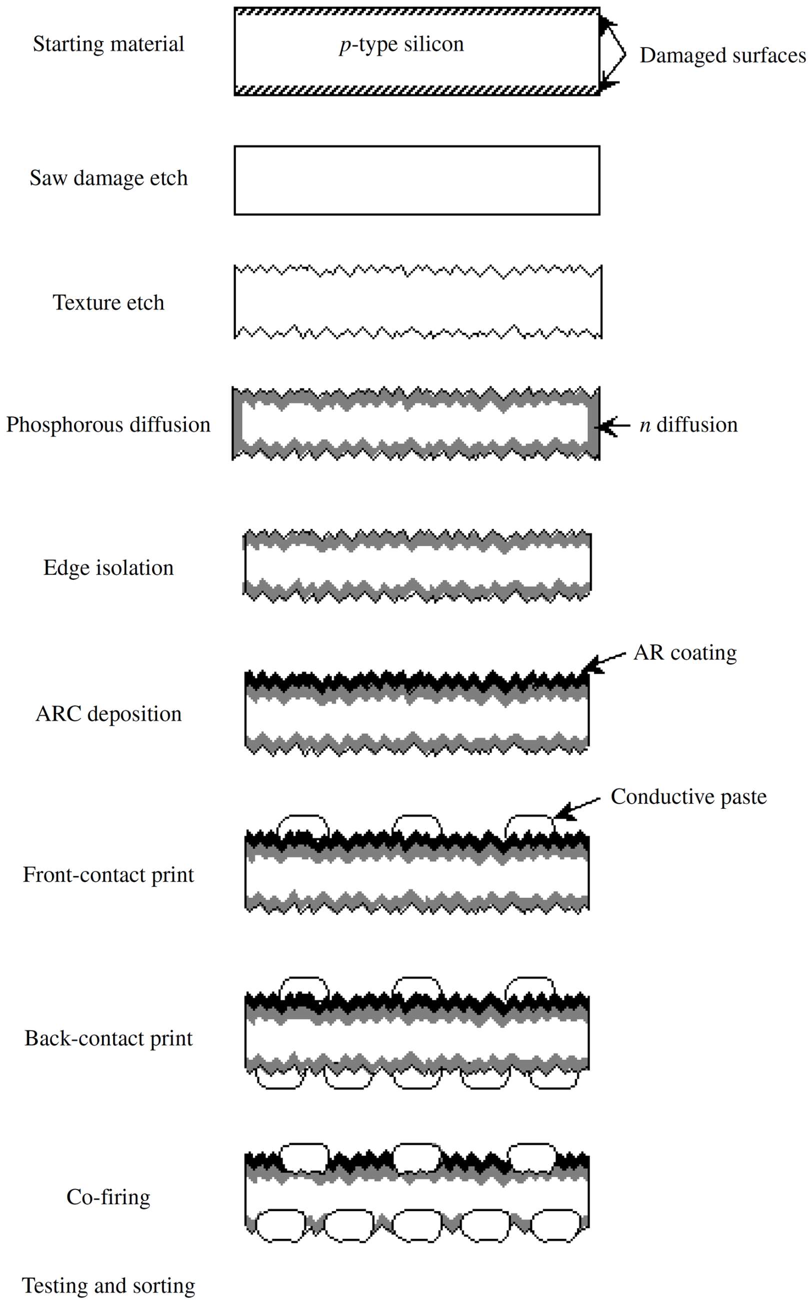

Fig. 2.1 Typical fabrication process flow with subsequent steps.

2.2 Solar cell architectures

A crystalline silicon solar cell is a device with a quite simple working process. Light must be absorbed to the highest extent, converted as much as possible into charge carriers, then these carriers must be separated before they recombine and collected through an external circuit to generate power. Thus solar cell architecture respect these demands: the exposed surfaces are optimized to absorb incident light, the bulk of the cell is the region where light is converted and carriers generated, the emitter region forms the *pn*-junction used to separate the carriers, the metallic contacts provide the external electrical connection to the device. All this regions must be optimized in order to reduce the losses and increase the conversion efficiency. Fig. 2.2 shows a basic structure for a conventional solar cell.

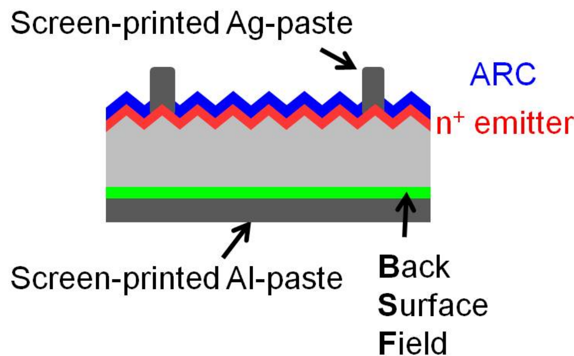

Fig. 2.2 Conventional solar cell basic architecture [39].

2.2.1 Bulk region

The highest efficiency are achieved with FZ silicon, which, due to the extreme crystalline perfection and the low impurity levels, offers the highest lifetime for SRH recombination, in the millisecond range or higher. Industrial cells are usually made with Cz silicon because of its availability and cost. Low cost

commercial cells are made with multicrystalline substrates, growth with specific procedures for the photovoltaic industry. In this kind of bulk, lifetimes are lower due to the crystal defect, such as dislocations and grain boundaries, and also to the high metallic contamination. Contamination during the fabrication process is an important problem. The insertion of gettering steps in the fabrication flow helps to reduce this issue that can reduce initial lifetimes. In general, is it possible to get advantage of the fact that phosphorous and aluminum diffusion, under certain conditions, produce gettering [40], i.e. the segregations of impurities in layers where they have a lower impact on the performance.

The doping type and level of the bulk is another important aspect of the fabrication. The standard for many years in solar cell industry has been *p*-type doping for the bulk with *n*-type emitter. The origin of this is historical and related to the first commercial applications of solar cell in space industry. It was found that *p*-type solar cells has less lifetime degradation due to radiation damages, because of the smaller electron capture cross-section for damage centers [41]. Another argument is based on physical properties of boron. Electrons have an higher mobility than holes (about a factor of 3), therefore, for the same minority carrier lifetime, the diffusion length of electrons (minority carrier in *p*-type substrates) is longer. However, for the modern situation of high-efficiency commercial solar cells, these reasons are no longer adequate.

First, most of the cell produced are used in terrestrial application, where radiation damage is not a problem. Second, and more important, the mobility advantage is based on the assumption that electrons and holes have the same lifetime as minority carrier. This is not true when considering the low-cost commercial-grade silicon wafer used for the industrial processes. In fact, the production process can introduce many defects in the silicon, such as chemical impurities or metallic contamination. The *n*-type silicon substrates have been found less sensitive to chemical impurities activated during high temperature

steps [42] [43]. Moreover, recent studies have shown a severe light-induced lifetime degradation for low-resistivity boron-doped Cz wafers, due to the creation of boron-oxygen complexes [44]. For all these reasons the production of high efficiency laboratory solar cells as well as that of commercial solar panels is moving towards *n*-type substrates. In fact, both the highest efficiency crystalline silicon cell [9] and the highest efficiency commercial module [45] have an n-type substrate. The optimum doping level depends on the cell architecture and the dominant recombination mechanism. Low doping present advantages in terms of higher Auger-limited lifetimes, while high doping levels may have advantages in terms of SRH recombination, since it depends on excess carriers density which decreases as the doping increases. Moreover higher doping also reduces the series resistance component. Industrial cells have doping levels in the order of $10^{16} cm^{-3}$.

Regarding the thickness there is a trade-off between light absorption and recombination. Thicker cells improve the absorption of light, since it depends on the optical path, but if the diffusion length is lower than the thickness the recombination becomes relevant. Thinning the cell increases surface recombination component and reduces light absorption (that can be enhanced with light trapping techniques), therefore the types of cell with non-ideal light trapping or relatively high surface recombination benefits of greater thickness (250-400 μm). Back-contacted solar cells have more advantages in thinning the substrate, both for resistance and for recombination issues, therefore the average thickness is about 150-200 μm. Commercial solar cells have a low diffusion length, due to low-grade silicon, and are rather insensitive to thinning. The most important aspect is the cost of the material, and this is the reason because the industry is trying to move to thinner and less expensive substrates.

2.2.2 Front surface

The front surface of a conventional solar cell contains three main elements: the metal contact, the optical structure and the emitter region. Metal grids are place on the front surface to create the electrical contact and collect the photogenerated carriers. Their geometries must be carefully designed to cope with the trade-off between the high resistivity, for narrow metal lines, and the shadowing losses, due to reflected and obstructed light, for large contacts. Laboratory cells use high cost techniques, such as photolithography and evaporation to create narrow metal fingers (10 to 15 μm) with high conductive materials, not suitable for commercial mass production, where usually Ag screen printed contacts are used (100 μm).

The optical structure is created to enhance light absorption to the highest extend. Part of the light (around 10% or more) is lost for the metal contact shading. Another loss is due to the reflectance of silicon, more the 30% for bare Si in air. This reflectivity is reduced by applying a mono- or multi-layer of non-absorbing material on the top surface of the cell. This is called anti-reflective coating (ARC) and uses destructive interference to reduce the amount of reflected light. The ARC is designed to have the minimum of reflectance ar around 600nm, where the photon flux of the solar spectrum is maximum. Material used for ARC can be various, like TiO_x, SiN_x or SiO_x. To further decrease the reflected light, a treatment called texturization is applied. Alkaline (KOH or NaOH-based) solutions are used to etch the silicon surface and create random, square-based pyramids, with sizes of a few nanometers. An incident light ray is reflected to the pyramids around and this increases the absorption probability (see fig. 2.3). Other techniques have been used to create different texturing, such as inverted or regular pyramids [46]. Light entering the cell is tilted with respect to the normal and this causes the photogeneration to happen closer to the junction, which is very important for cell with a low diffusion length, enhancing the collection of medium and long

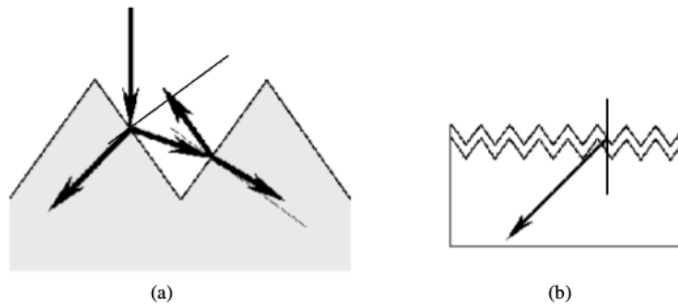

Fig. 2.3 Front surface texturing effects: (a) decreased reflection and (b) increased photogeneration.

wavelengths. Together with ARC this treatment greatly reduces the reflected light.

The emitter is the regions of the cell with a complementary doping with respect to the bulk. At the interface between the emitter and bulk regions, the *pn*-junction, responsible for the carrier separation, is formed. Doping and dimensions of the emitter may vary depending on the characteristics of the cell. If the region extends all across the surface it's called homogeneous emitter and the collection probability in this case is very sensitive to surface recombination.

For cells with poor passivation the emitter is very thin and highly doped to improve the electric contact with the metallization, while if the surface recombination is lower is possible to increase the depth of the region and reduce the doping in order to improve lifetimes in the region. In general the emitter is created with a two steps process, with a deposition of the doping species on the surface (predeposition) and a heat induced diffusion into the substrate (drive-in). Other improved and more optimized types are the selective and localized emitters [47], which uses multiple step process to create more performing structures, at the cost of increasing complexity. For industrial solar cells the emitter design is strongly influenced by the screen printed metallization. In order to achieve a low resistivity contact the region

must be very highly doped and thick enough to not be perforated during the firing step. This creates a very poor photovoltaic active region that strongly reduces the short wavelength absorption and increases recombination.

2.2.3 Back surface

On the back surface of the cell is present the second metallic contact, the one for majority carriers. Since the recombination on the metal is quite high, it is very important to prevent that minority carriers arrives in that zone, and this is made using the effect of an electrical field that repels minority carrier, created by a doped region called *back surface field* (BSF). For industrial cell, since the thickness is much greater than the diffusion length, this effect is irrelevant and thus they are not optimized for this purpose. For high-efficiency solar cells, however, a good BSF design is crucial. Like the emitter, even for BSF there are different structures and types. Homogeneous BSF spans across all the back interface all over the contact for a full surface metallization. For localized contact, if the passivation is poor, the BSF can be used to reduce surface recombination at the back interface, while, with a good passivation it can be restricted to the contact size, both for striped or pointed contacts. A shallow and light diffusion on the back helps in many cases in reducing surface recombination; this diffusion can be of the same type of the substrate [48] but also of the opposite one [49].

2.3 Back-contact solar cells

A solar cell is defined as back-contact when both metallic contacts are on the rear side of the cell, the non-illuminated one. This is an evolution of the standard solar cell structure, that allows to get many advantages but also some drawbacks:

Pros

- Complete absence of shadowing losses, thus increased short-circuit current I_{SC}.
- Lack of trade-off for the front contact between large width for low resistance and narrow width to reduce shadowing, thus reduced series resistance R_S.
- Possibility to optimize the front surface for light trapping and reduced surface recombination.
- Both contacts on the rear side make possible coplanar interconnections at module level, reducing the occupied area.
- Uniform exposed surface with a plain color (generally black) that increase the appeal for all the applications of PV in urban contexts.

Cons

- More complex architectures, that requires a few more fabrication steps than a conventional solar cell.
- Need for high quality silicon with good lifetime, since having both contacts on the rear side, diffusion length for minority carriers generated in the front must be high.
- Surface recombination velocities on both surfaces and on metal are crucial to obtain good efficiencies

In general the material used for back-contact solar cells must be of high quality, and this, along with the more complex fabrication process, leads to an higher cost with respect to the conventional solar cells. Higher efficiencies are then required to compensate the increased cost, and this can be obtained with an optimization process of all the parameters of the cell, object of this thesis.

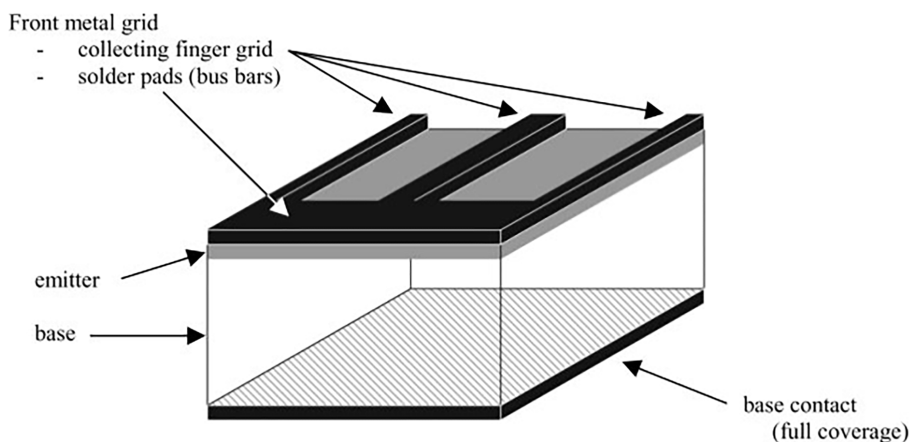

Fig. 2.4 Conventional solar cell architecture.

A conventional solar cell architecture is presented in fig. 2.4. The emitter region is on the top side of the cell and metal contacts are on both surfaces, with a grid on the front, formed by fingers and bus-bars, and a completely metal covering on the back.

Back-contact solar cells architectures can be divided into three main groups:

- *Metallization wrap-through* solar cells (MWT).
- *Emitter wrap-through* solar cells (EWT).
- *Interdigitated back-contact* solar cells (iBC), also called *back-contact back-junction* solar cells (BC-BJ).

In the following sections a short review of these kinds of cells is presented, while a complete and extensive review can be found in [50].

2.3.1 Metal wrap-through (MWT)

Metallization wrap-through is the concept more similar to a conventional solar cell [51]. The emitter region and the junction are still near the front

surface and even a part of the metallization is on the top. Busbars, however, are placed on the rear and the connections with the top fingers are made with laser drilled holes in the cell (see fig. 2.5). Due to the similarities with a

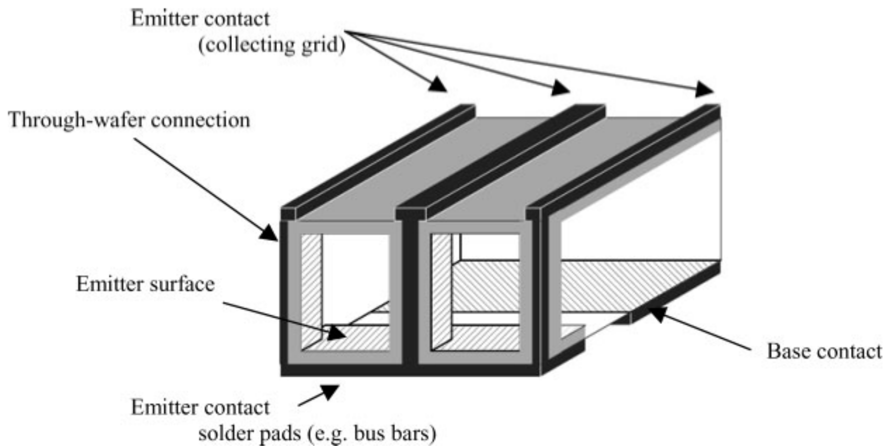

Fig. 2.5 Metal wrap-through (MWT) solar cell architecture.

conventional cell, transition from fabrication of standard cells to MWT cells is not particularly difficult, however the laser drilling of metal connections is a sensitive process. The advantages over conventional cells are the reduced shadowing losses and the coplanar interconnections possibility, while the drawbacks are the more complex fabrication and the high recombination over the walls of the interconnection holes.

2.3.2 Emitter wrap-through (EWT)

In the emitter wrap-through design the front surface is void of any metallization [52][53]. The emitter region is both on the top and the rear of the cell, while the relative contact is only on the back side. The front and back emitters are connected via diffused laser drilled holes (see fig. 2.6). This architectures provides the advantage of completely absence of shadowing losses and coplanar interconnections, such as the BC-BJ architecture. An

advantage on the BC-BJ cells is that, since there are two junctions, on front and rear side of the cell, the path for the minority carriers to travel before been collected is shorter. This means lower required lifetimes in the bulk and therefore allows to use lower grade silicon.

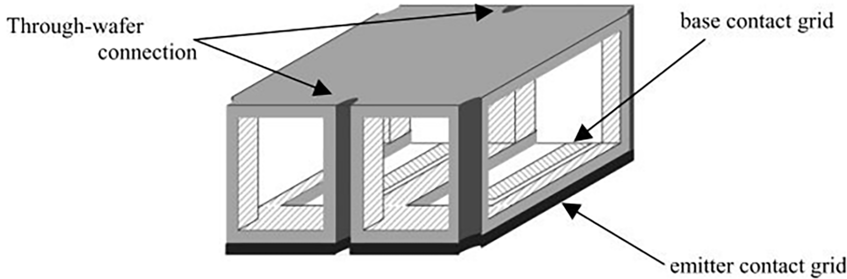

Fig. 2.6 Emitter wrap-through (EWT) solar cell architecture.

2.3.3 Interdigitated back-contact (iBC)

The concept of interdigitated solar cells was proposed by Schwartz and Lammert in 1975 [54][55], as a solution for solar concentrator. In this architecture both metal contacts are placed on the rear side of the cell, in form of interdigitated pattern. Also the emitter and back surface field diffusion regions follow the interdigitated design (see fig. 2.7). This design offers all the advan-

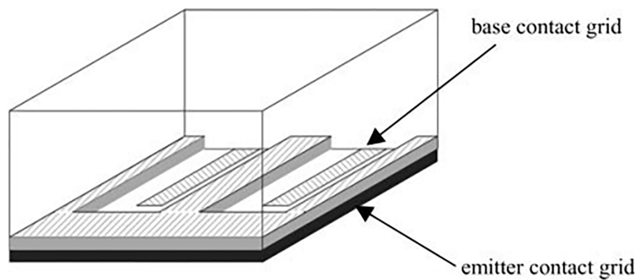

Fig. 2.7 Interdigitated back-contact (iBC) solar cell architecture.

tages mentioned above, such as completely lack of shadowing, possibility of coplanar interconnections and low series resistance, due to possible high metallization coverage on the rear. However there are some critical parameters to take in account. Most of the carriers are generated near the top surface (since most energetic photons are absorbed almost immediately inside the cell). In iBC, however, the junction is on the rear side of the cell. Therefore, in order to be collected, carriers have to travel from one surface to the other, avoiding recombination due to two main causes: a poorly passivated front surface and a low lifetime bulk. Thus lifetime in the bulk, τ_{bulk} and surface recombination velocity at front surface, S_f are the most critical parameters in the iBC solar cell architecture.

Chapter 3

Solar cell numerical modeling

In this chapter the methodology of numerical simulation of a solar cells will be presented. Technology Computer-Aided Design (TCAD) software Sentaurus, used in this work, will be explained, along with the main calibration parameters and models implemented in the simulation process to achieve the best reliability and correspondence with actual fabricated device behavior.

3.1 Introduction to solar cell numerical simulations

Numerical simulation of silicon solar cells provides many advantages over the repeated fabrication approach. First, the much lower cost of implementation, eliminating the need for production equipment or material, along with clean room and facilities. Moreover the simulations can be used to analyze the behavior of a cell in detail, pointing out loss mechanisms intrinsic in specific regions or due to specific causes. Multidimensional simulation are the standard nowadays, given the more complex architecture of the cells and for a more accurate modeling of lateral and vertical currents. For many years the most used solar cell simulator was PC1D, developed at Iowa University in

1985 [56]. It is a software capable to solve semiconductor equations using finite element method (FEM) , unlike many other previous programs. However, the possibility to obtain only one dimensional simulations, along with the use of dated physical models, make this software outdated and not sufficient for modern solar cell simulations. Though there are some other TCAD simulator softwares on the market, such as ATLAS from Silvaco [57], or COMSOL Multiphysics [58], the most diffused simulator for solar cells is Sentaurus by Synopsis [11].

3.2 Finite Element Method

Sentaurus is a general purpose finite element method simulator for semiconductor devices. The behavior of a solar cell is simulated solving the Drift-Diffusion model described in Chapter 1 and in particular the three equations that govern the carrier motion in a semiconductor, which are:

- Poisson equation (eq.1.33)
- Continuity equation for electrons and holes (eq. 1.34, 1.35)
- Transport equations (eq. 1.26, 1.27)

The partial differential equations (PDE) listed above are discretized and solved using the FEM, which has the advantage over the finite difference method (FDM) of being able to handle very complicate geometries and structures, at the cost of a more complicated implementation [59]. Since its original application in structural analysis, the FEM has been used in many fields, from hydraulics to mechanics, to electronic devices simulation, to analyze very different types of structures and interactions. In general, the steps to apply this method are [60]:

- The domain of simulation is divided into a finite number of sections or elements

- A simple function to approximate the variation of the governing equation for each element is derived
- The functions of each section are assembled in the solution region
- The resulting system of equations is solved

The main advantage of this approach is that is possible to divide very complex simulation domains into small, simple sections, such as rectangular or triangular boxes in case of 2D simulation. The resulting structure, called *mesh*, is one of the fundamental phases in the simulation process. A mesh too fine leads to an huge number of points and thus to increased computational power and time, while a mesh too coarse can result in losing information and accuracy of the simulation or even in convergence problems. Fig. 3.1 shows an example for a good constructed mesh. It is worth noting that the mesh consists both of triangular and rectangular elements and how the element size is smaller in the regions where a more precise modeling is required, such as corner or interfaces between different materials. Once the mesh is defined, the next step is to define the desired function for each element, for example the potential V_e. It's necessary to defined an approximation for the potential within any element and interpolate the distribution at the boundary of each box to grant continuity. The approximate solution for the entire region is

$$V(x,y) \backsimeq \sum_{e=1}^{N} V_e(x,y) \tag{3.1}$$

where N is the number of elements in which the solution region is divided. Most common approximation for V_e inside an element is a polynomial expression, such as:

$$V_e(x,y) = a + bx + cy \tag{3.2}$$

for triangular elements and

$$V_e(x,y) = a + bx + cy + dxy \tag{3.3}$$

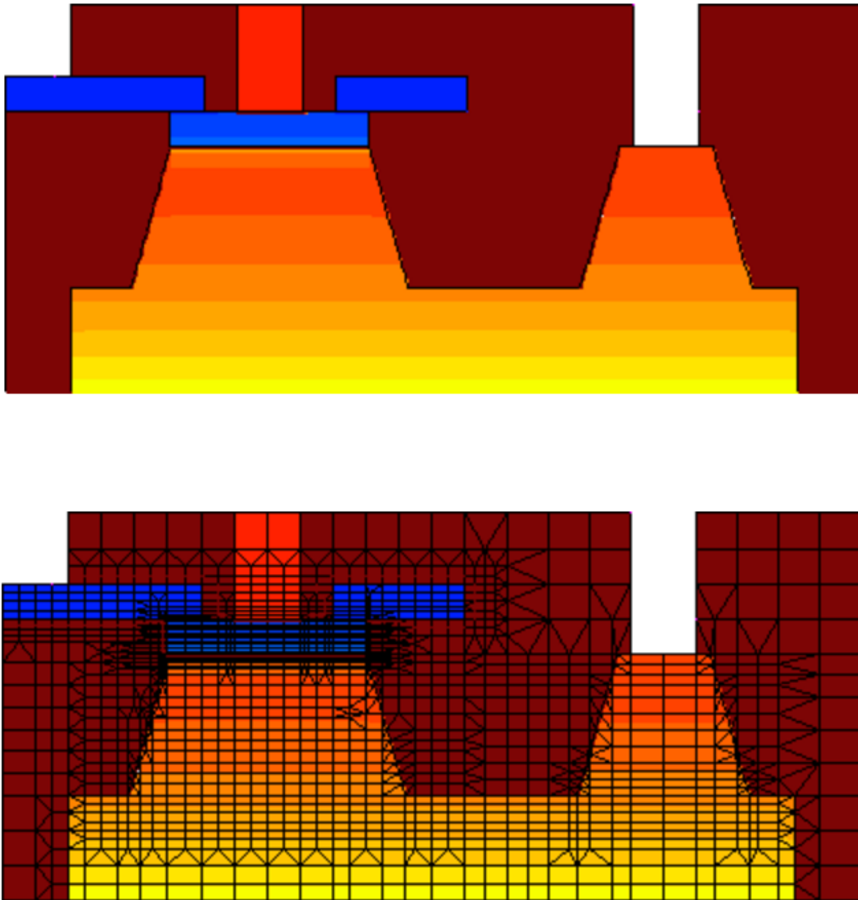

Fig. 3.1 Finite element method mesh implementation example.

for a quadrilateral element. The constants a, b, c and d needs to be determined. The potential is usually non-zero inside the element and goes to zero outside. Poisson's, continuity and transport equations are discretized for each node of the mesh and solved using Newton iterative method with the application of Bank Rose algorithm [59], to determine electron and hole concentrations and electrostatic potential in the whole device.

3.3 Physical models

The process of simulation of solar cell requires that all the physical mechanisms that occur in a real cell are reproduced inside the numerical simulation. This ensures the accuracy of the results and the possibility to use them for a correct analysis. Physical phenomena are described with mathematical models that, within a certain degree of approximation, can be successfully used to emulate their effects. For the simulations presented in this work, the models reproducing the behavior of a solar cells have been implemented in the Sentaurus simulator and calibrated with the state-of-the-art parameters in literature. A thorough examination of solar cell modeling can be found in [61]. Specific models have been used for: Fermi-Dirac statistics, Band-Gap narrowing (BGN), carrier mobility, Auger recombination, SRH recombination in bulk and at the surfaces.

3.3.1 Carrier statistics

Electrons and holes concentrations can be calculated from their respective quasi-Fermi potentials, using the Boltzmann statics (used for many years in solar cells simulations):

$$n = N_C \, e^{\left(\frac{F_N - E_C}{kT}\right)} \tag{3.4}$$

and

$$p = N_V \, e^{\left(\frac{E_V - F_P}{kT}\right)} \tag{3.5}$$

where N_C and N_V are the effective density-of-states, F_N and F_P the quasi-Fermi energies for electrons and holes and E_C and E_V the conduction and valence band edges. However, if the doping density is higher than 10^{19}, a concentration that can be usually found in the n^+ heavily doped emitter and often

also in the BSF region of the iBC cells, Pauli exclusion principle becomes relevant with an effect called Pauli blocking [62], and Fermi-Dirac statistics implementation must be used. Activating the correspondent command in the simulator is possible to use this more accurate carrier statistics to calculate carrier densities as [11]:

$$n = \gamma_n N_C \, e^{\left(\frac{F_N - E_C}{kT}\right)} \tag{3.6}$$

and

$$p = \gamma_p N_V \, e^{\left(\frac{E_V - F_P}{kT}\right)} \tag{3.7}$$

where γ_n and γ_p are expressed as:

$$\gamma_n = \frac{n}{N_C} \, e^{\left(-\frac{F_N - E_C}{kT}\right)} \tag{3.8}$$

and

$$\gamma_p = \frac{p}{N_V} \, e^{\left(-\frac{E_V - F_P}{kT}\right)} \tag{3.9}$$

3.3.2 Band Gap Narrowing (BGN)

Intrinsic carrier concentration n_i is a key parameter in the simulation of a solar cell, since it affects all the recombination processes which are one of the main limiting factor for the efficiency. The most widely used value for this parameter was measured in 1991 as $n_i = 1 \times 10^{10} cm^{-3}$ [63], but this value was later demonstrated to be influenced by band gap narrowing (BGN) [64]. BGN is a shrinkage of the bandgap that occurs when the impurity concentration is particularly high. Shallow level donor impurities create energy levels near the conduction band, and shallow level acceptor impurities create levels near the valence band. The overlap of this states with increasing

doping creates a continuum of states that reduces the bandgap. Schenk in 1998 proposed a finite-temperature full random-phase approximation model for BGN [65], determining $n_i = 9.65 \times 10^9 cm^{-3}$ for undoped silicon. Bandgap is temperature dependent, and this has been modeled as [66]:

$$E_g(T) = E_g(0) - \frac{\alpha T^2}{T+\beta} \tag{3.10}$$

where α and β are parameters specific for the material and $E_g(0)$ is the bandgap for $T = 0K$. For a specific temperature T, the effective bandgap is:

$$E_g,eff(T) = E_g(T) - E_{BGN} \tag{3.11}$$

where

$$E_{BNG} = \Delta E_g^0 + \Delta E_g^F \tag{3.12}$$

E_g^F is a correcting factor used in correlation with the Fermi statistics mentioned before [11] and E_g^0 is determined by the particular bandgap narrowing model used. Many authors have proposed models to describe doping induced BGN, such as Bennet-Wilson [67], Slotboom [68] [69] [70] [71] and Jain-Roulston [72]. A very used model for BGN in n-type silicon is from del Alamo [73] [74] [75], according to which:

$$\Delta E_g^0 = \begin{cases} E_{REF}\ ln\left(\frac{N_{TOT}}{N_{REF}}\right) & \text{if } N_{TOT} \geq N_{REF} \\ 0 & \text{if } N_{TOT} < N_{REF} \end{cases} \tag{3.13}$$

where $N_{REF} = 7 \times 10^{17} cm^{-3}$ and $E_{REF} = 18.7 \times 10^{-3} eV$, and N_{TOT} is the total doping concentration. All these models do not depend on free carrier concentration, however high carrier concentration due to optical generation may cause bandgap narrowing. In order to reproduce the increase in the intrinsic concentration n_i occurring at high doping density and to take in account high carrier injection due to optical generation, the model proposed

in [76] has been implemented. It is a revised Schenk bandgap narrowing model with Fermi-Dirac statistics set to properly obtain the value of $n_i = 9.65 \times 10^9 cm^{-3}$ at low doping density, that has very good agreement with experimental data reported in [64]. Fig. 3.2 reports the intrinsic carrier density

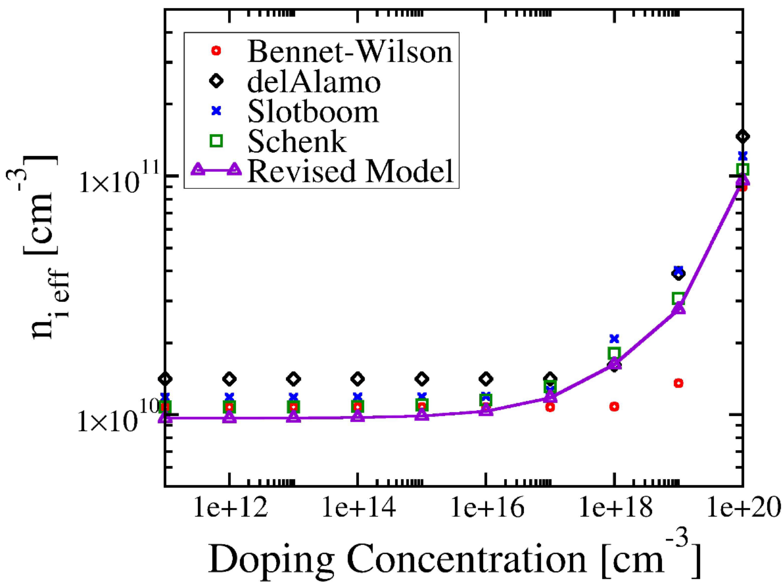

Fig. 3.2 Intrinsic carrier density accounting for BGN for different models, including the revised one used for the simulations [76].

n_i dependence from the doping concentration for different models (Bennet, del Alamo, Slotboom, Schenk) together with the revised model used in this work. In Sentaurus some of the cited models are already implemented, but is also possible to provide a tabled customized bandgap narrowing model, which is the method applied for the simulations.

3.3.3 Carriers mobility model

Mobility is parameter that takes in account the interactions of the carriers accelerated by electric field with lattice phonons, impurity ions, other carriers and surfaces (see eq.(1.19)). A very widely used model for mobility in PV simulations, and also in this work, was proposed by Klaassen in 1992 [21] [77], and it's called Philips unified mobility model. It describes majority and minority carrier mobility and includes impurity screen by charge carriers, electron-hole and cluster of impurities scattering and temperature dependence. It is a good calibrated model and fits boron doped silicon very well, while there is slightly less accuracy in the higher doping range for phosphorous, as showed in fig. 3.3.

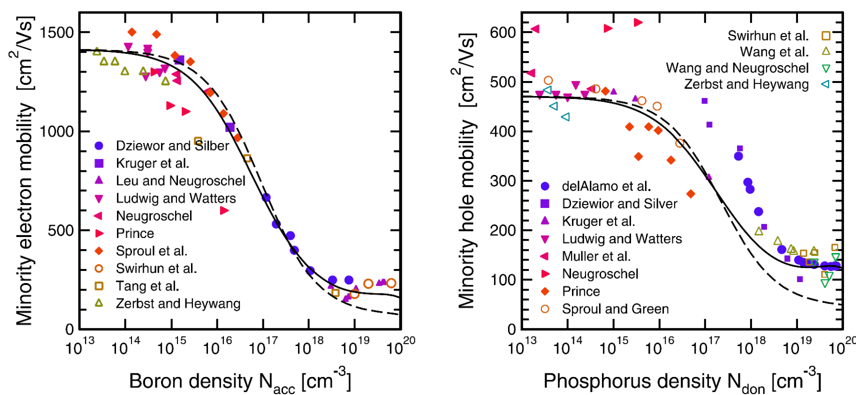

Fig. 3.3 The symbols are measured minority electron mobility (left) and minority hole mobility (right). Klaassen's model of the majority mobility is shown as dashed line, while model of the minority as solid line [61].

3.3.4 Bulk recombination

Recombination is the complementary process of generation, a response of the system to a state of disequilibrium caused by an external perturbation (such as optical generation) and, as described in Chapter 1, is one of the

most important mechanisms in the operation of a solar cell. The different types of recombination have been parametrized with specific models to improve the accuracy of the simulations. Intrinsic recombination, consistent to Coulomb-enhanced Auger and radiative recombination, has been parametrized according to Richter *et al.* in [78] and [79] to account for dopant density and carrier injection level by the calculation of intrinsic recombination lifetime of minority carriers τ_{int}.

$$\tau_{int} = \frac{\Delta n}{(np - n_{i,eff}^2)(2.5\times10^{-31} g_{eeh} n_0 + 8.5\times10^{-32} g_{ehh} p_0 + 3.0\times10^{-29}\Delta n^{0.92} + B_{rel}B_{low})} \quad (3.14)$$

with the factors:

$$g_{eeh}(n_0) = 1 + 13\left\{1 - tanh\left[\left(\frac{n_0}{N_{0,eeh}}\right)^{0.66}\right]\right\} \quad (3.15)$$

and

$$g_{ehh}(n_0) = 1 + 7.5\left\{1 - tanh\left[\left(\frac{p_0}{N_{0,ehh}}\right)^{0.63}\right]\right\} \quad (3.16)$$

with $N_{0,eeh} = 3.3\times10^{17} cm^{-3}$, $N_{0.ehh} = 7.0\times10^{17} cm^{-3}$ and B_{low} and B_{rel} radiative related recombination coefficient.

Recombination losses due to trap-assisted recombination through deep defect level has been modeled by assuming the single-level trap model by Shockley–Read–Hall (SRH) [17] [18] with traps in the energy mid-gap.

$$R_{net}^{SRH} = \frac{np - n_{i,eff}^2}{\tau_p(n + n1) + \tau_n(p + p_1)} \quad (3.17)$$

with

$$n_1 = n_{i,eff} e^{\frac{E_{trap}}{kT}} \quad (3.18)$$

and

$$p_1 = n_{i,eff} e^{-\frac{E_{trap}}{kT}} \tag{3.19}$$

The doping dependence of carrier lifetimes (τ_{SRH}) in phosphorus-doped FZ-Si has been calculated using the empirical determined Scharfetter relation according to [80]:

$$\tau_{SRH} = \frac{\tau_0}{1 + \frac{N_{dop}}{N_0}} \tag{3.20}$$

where $\tau_0 = 2ms$ and $N_0 = 1.6 \times 10^{16} cm^{-3}$. In this way, effective bulk lifetime τ_{eff} can be estimated as:

$$\frac{1}{\tau_{eff}} = \frac{1}{\tau_{int}} + \frac{1}{\tau_{SRH}} \tag{3.21}$$

3.3.5 Surface recombinations

To account for the SRH recombination due to defects at material interfaces, either planar or textured, the model used is an extension of the SRH formula in the bulk:

$$R^{SRH}_{surf,net} = \frac{n_s p_s - n^2_{i,eff}}{(n_s + n_{i,eff} e^{\frac{E_{trap}}{kT}})/s_p + (p_s + n_{i,eff} e^{-\frac{E_{trap}}{kT}})/s_n} \tag{3.22}$$

where n_s and p_s are the hole and electron densities at the surface and s_n and s_p are the surface recombination velocities (SRV) for electrons and holes, respectively. The recombination rate is limited by holes in n-type regions, i.e by the recombination velocity parameters for holes s_p, and, complementary, by the electron surface recombination velocity s_n in p-type regions.The recombination velocities of otherwise identically prepared surfaces depend, in general, on the concentration of the dopant at the surface. Sentaurus calculates

Table 3.1 SRV doping dependence model parameters for eq.(3.24).

Parameter	*Planar*	*Textured*
s_1 (cm/s)	500	2800
N_1 (cm^{-3})	1×10^{19}	1×10^{19}
γ_1	0.6	0.6
s_2 (cm/s)	60	300
N_2 (cm^{-3})	1×10^{19}	1×10^{19}
γ_2	3	3

this dependence as:

$$s = s_0 \left[1 + s_{ref} \left(\frac{N_{dop}}{N_{ref}} \right)^{\gamma} \right] \tag{3.23}$$

where N_{dop} is the doping concentration at the surface and s_0, s_{ref}, N_{ref} and γ are user defined parameters. For phosphorous doped passivated surfaces, Altermatt *et al.* found a more accurate formula to fit the experimental data, which is [62]:

$$s = s_1 \left(\frac{N_{dop}}{N_1} \right)^{\gamma_1} + s_2 \left(\frac{N_{dop}}{N_2} \right)^{\gamma_2} \tag{3.24}$$

All the parameters in eq.(3.24) are dependent on the passivation material, the doping species and the geometry of the surface (planar or textured). In table 3.1 are reported the parameters for both planar and textured surface and in figure 3.4 the fitting of measured data with the modeling curves. For a boron doped region surface, the same model can be used but taking also in account the effect of the fixed trapped charge at the interface, which, since is positive, increases the recombination velocity of the minority carries (electrons) from 3 to 5 times [81] [82].

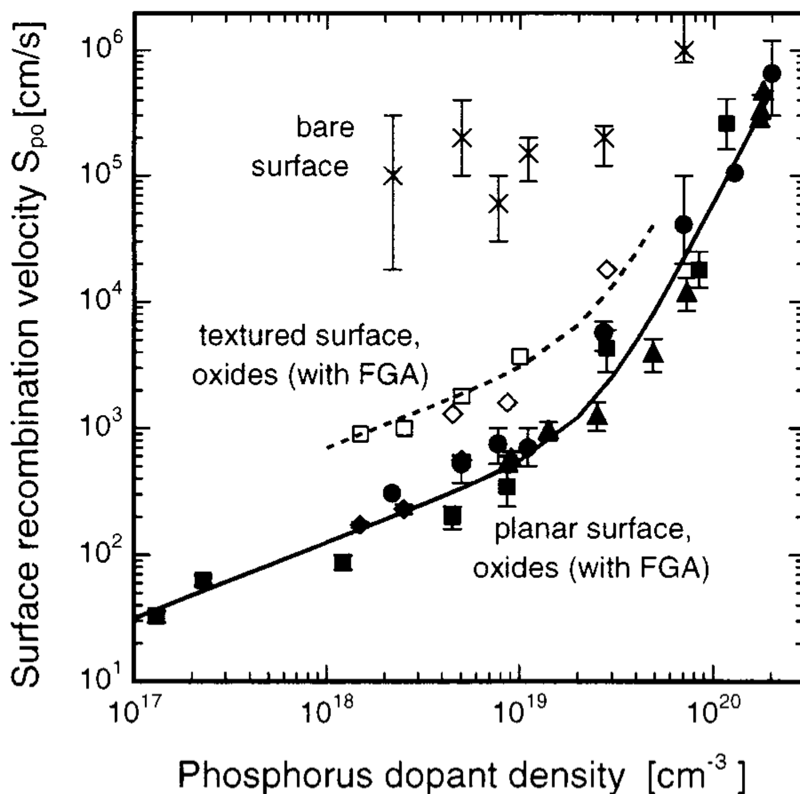

Fig. 3.4 Surface recombination velocities for holes s_{p0} as function of the doping level. Symbols are measurements in different scenarios while lines are parametrization of eq. (3.24), dashed for textured and solid for planar surfaces, respectively [62].

3.4 Optical generation

An important mechanisms to carefully model for an accurate simulation of the behavior of a solar cell is the optical generation of carriers due to light exposure. As explained in Chapter 1, incident light, through the photovoltaic effect, creates electron-hole pairs inside the semiconductor. The characteristics of the incident light (wavelength, intensity) and of the exposed surface (reflectance, absorption) as well as those of the rear surface must

be parametrized and modeled. The simulated cell featured a textured front

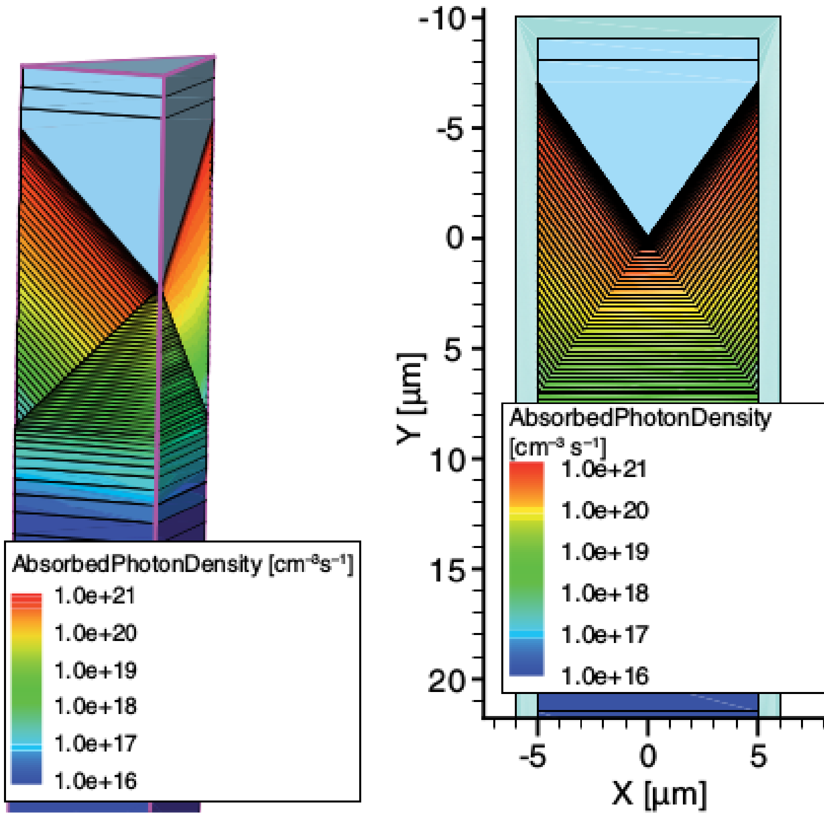

Fig. 3.5 Schematic of the 3D simulated domain for the optical generation calculation (left) and 2D slice (right).

surface with anti-reflective coating (ARC). The texturing consisted of regular upright pyramids of 10 μm-wide base and opening angle between the two faces of 70°. The ARC was composed by 42 nm Si_3N_4 and 27 nm SiO_2. These values were chosen in order to minimize reflection for wavelengths close to the peak power of the solar spectrum. The power spectrum of the incident light has been parametrized according to the AM15G spectrum [14]. A 3D pyramidal structure has been simulated using raytracing simulator accounting

for the thin film stack boundary condition to model ARC at front interface. The domain used for the calculation of the optical generation is shown in fig. 3.5. Raytracer in Sentaurus uses a recursive algorithm, starting with a source ray and building a binary tree that track the transmission and the reflection of the ray. At interfaces with different refractive index a transmission/reflection

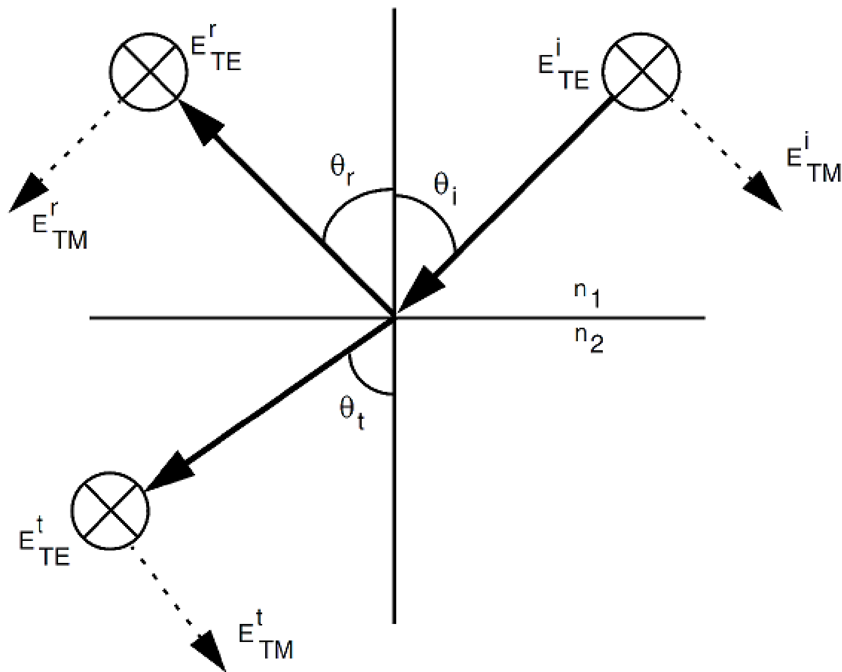

Fig. 3.6 Reflection and transmission of an incident ray at planar surface.

process occurs. Incident ray splits into reflected and transmitted rays, the TE component of the polarization vector keeps the same direction, while the TM component changes direction. This is best explained in fig. 3.6. E^i is the incident ray, with TE and TM polarization components, E^r is the reflected ray and E^t is the transmitted ray. n_1 and n_2 are the refractive index of the different materials and θ_i, θ_r and θ_t the incident, reflected and transmitted

angles. These angles can be derived form the Snell's law as:

$$n_1 sin\theta_i = n_2 sin\theta_t \tag{3.25}$$

The raytracer computes the plane of incidence at each interface, decompose the polarization vector into TE and TM components, and applies reflection and transmission coefficients to these components. To simulate the effect of the ARC the raytracer cannot be used directly due to the interference nature of the working process. A thin-layer stack boundary condition is used to model the interference effect in raytracing [11] (see fig. 3.7). The incidence angle

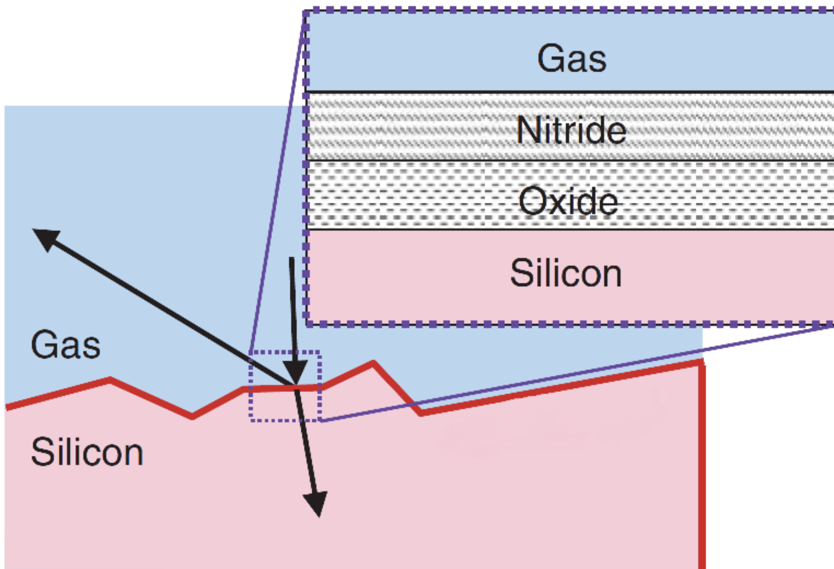

Fig. 3.7 Thin layer stack boundary condition used to simulate the ARC.

of rays is passed as input to a transfer matrix method (TMM) solver which returned reflectance, transmittance and absorption to the raytracer. TMM is used to calculate the propagation of light through a stratified medium,

where multiple reflections can interfere destructively or constructively. The method is based on the continuity condition for the electrical field across the boundaries from one medium to another, according to Maxwell's equations. The stack of layers is represented with a matrix which is the results of the product of the matrices corresponding to single layers. The non metalized back side was passivated by a 0.1 μm-thick SiO_2 layer, thus bottom internal reflectance was calculated by means of Fresnel equations according to the kind of back interface, passivated or contacted by aluminum. The rear side was assumed to be rough and was described by Phong rough-surface scattering model [83].

The 3D optical generation map calculated for different wafer thickness value was spatially integrated over the distance from the front interface in order to calculate the 1D optical generation profile. Finally, this optical generation map was interpolated on spatial nonuniform 2D mesh for the simulation of the device. The optical generation simulated in the whole solar cell simulation domain is showed in fig. 3.8. It is worth noting the slightly higher generation above the passivated portion of the back interface due the higher reflectivity of the silicon/passivation interface with respect to the silicon/aluminum interface.

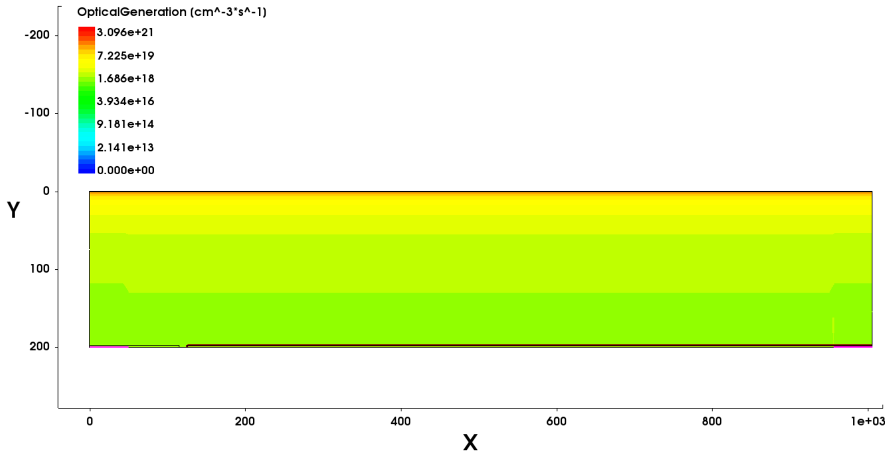

Fig. 3.8 Optical generation in the simulation domain of the solar cell.

3.5 Simulation domain and meshing strategy

For many years, the standard approach for solar cells simulation was to use 1D simulations of the transversal profile, using software like PC1D, given the homogeneity of the structure on the longitudinal axes. The novel and more complex architectures developed in recent years have made this kind of simulation not adequate anymore, creating the need of multidimensional 2D and 3D simulation. Fig. 3.9 shows the tridimensional sketch of an iBC solar cell. It's clear that the structure cannot be simulated with 1D approach, since the different transversal profiles and the necessity of taking in account lateral transport mechanisms. Given the homogeneity of the structure in depth, the more suitable approach is a 2D simulation of the structure, of a slice on the longitudinal axes. Fig. 3.10 shows a section of the structure with indicated all the main regions of the cell. In order to reduce the number of points of the mesh and consequently the computational power needed, but keeping the accuracy of the modeling, the simulation domain chosen is the symmetry element showed in fig. 3.11, that corresponds to the basic module of the structure.

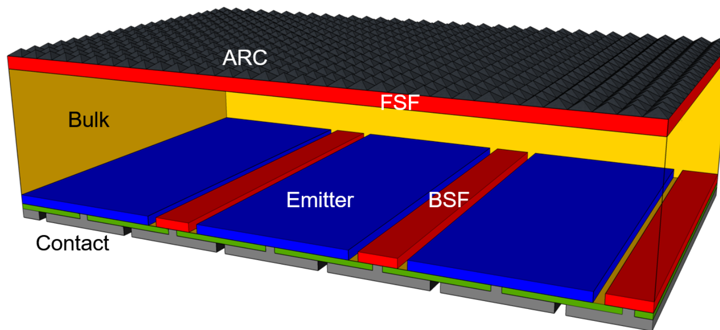

Fig. 3.9 3D sketch of an iBC solar cell.

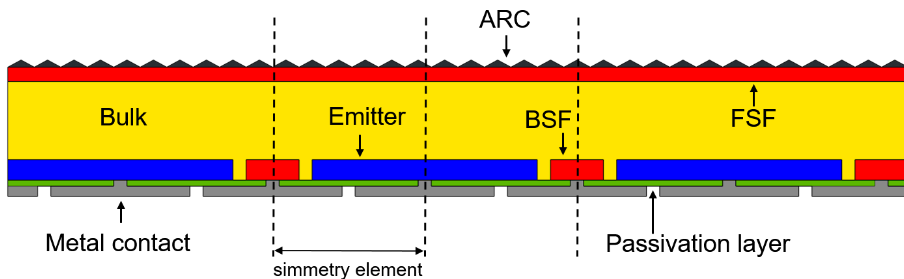

Fig. 3.10 2D longitudinal slice of the 3D structure of fig. 3.9.

The active area of the cell has been simulated, i.e. all the silicon regions, while metallization and passivation, as well as ARC on the front surface has been computed as boundary conditions. Only the metal contact portion directly adjacent to the structure as been included in the simulation, while fingers and busbars have been taken in account separately.

Once the simulation domain has been created with the structure editor tool of the simulator, an appropriate meshing strategy has been selected to achieve the best compromise between the number of points (which determine the computational time) and the required accuracy. The overall grid is showed in

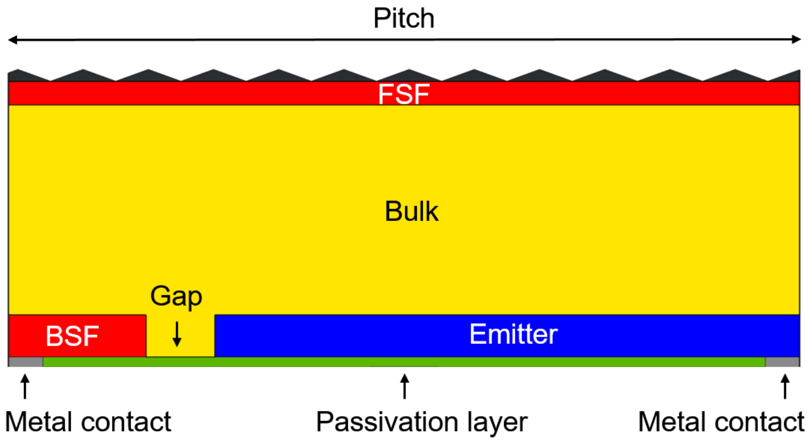

Fig. 3.11 Simulation domain used in this work and definition of the main regions.

fig. 3.12. The mesh was created finer where there is a need for more accuracy:

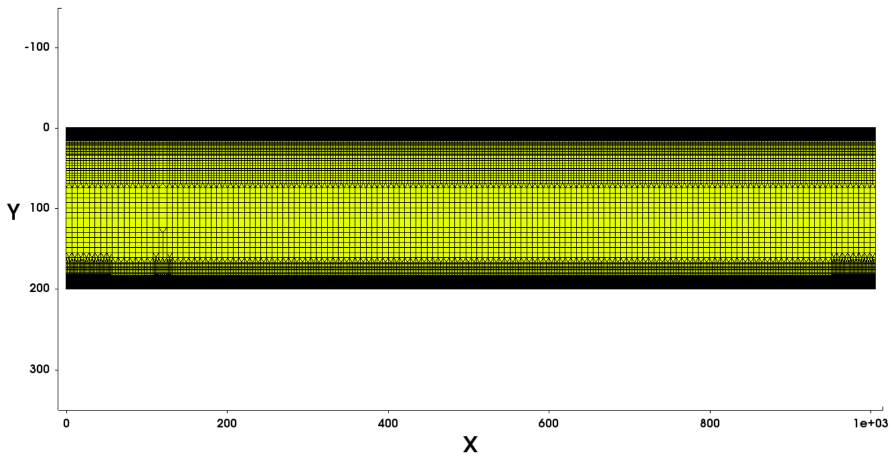

Fig. 3.12 Overall simulation mesh across the simulated domain.

near the front surface, where the most energetic carriers are absorbed and optical generation is higher (see fig. 3.13); near the rear surface, where

is located the *pn*-junction, and the BSF, to take in account the effect of Auger recombination (see fig. 3.14). Given the high impact of the surface recombination on the performance of this kind of cell, all the surfaces have been modeled with a very fine mesh, of minimum resolution of $1nm$. To reduce the number of points the step size was made coarser in the center region, where there was no need for such an high resolution.

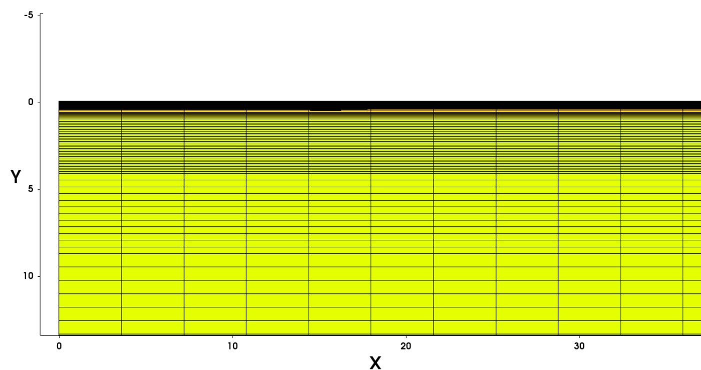

Fig. 3.13 Meshing strategy on the top surface, finer to better simulate FSF auger recombination, surface recombination and higher optical generation.

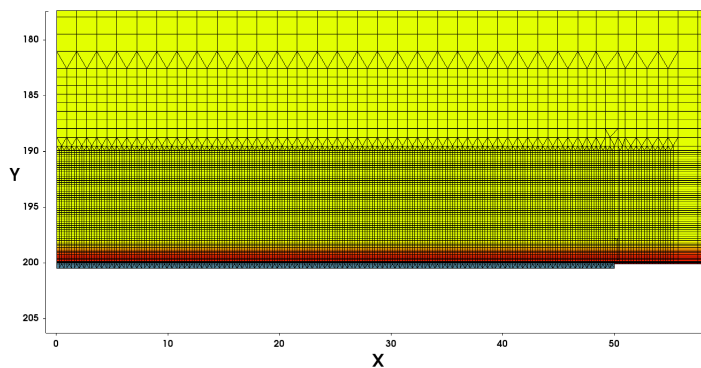

Fig. 3.14 Meshing strategy on the rear surface, finer to better simulate Auger recombination in emitter and BSF, surface recombination on the passivation and the contacts.

Chapter 4

Optimization of doping parameters

In this chapter the performance of the simulated solar cell will be analyzed with respect to doping parameters variations of the main regions of the simulated domain. The trends in efficiency will be detailed and explained, providing useful insight for a better calibration of the design process.

4.1 Simulation methodology

Fig. 4.1 shows a schematic representation of the element of symmetry simulated, as explained in Chapter 3. For this simulations a FZ-Si *n*-type doped wafer has been considered, with a thickness of 200 μm, featuring a resistivity of 2 Ω·cm, within the range reported by McIntosh *et al.* [84]. An ohmic contact of 100 μm without potential barrier and a resistivity of 2 $\Omega \cdot cm^2$ has been simulated. The recombination velocity for carriers at metal/Si interface has been set to 1×10^6 cm/s. Doping concentration has been considered fully ionized and activated. In order to investigate the impact of the main doping parameters, simulations has been performed by changing the doping peaks in emitter, BSF and FSF regions. In each set of simulations, only one

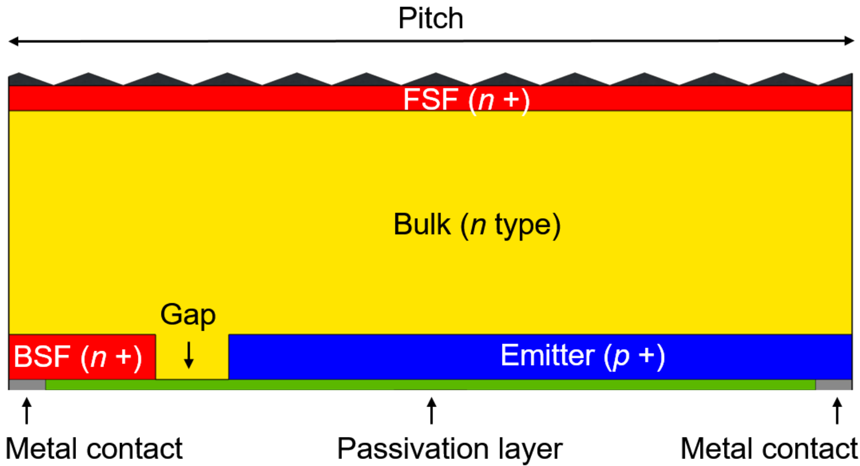

Fig. 4.1 Element of symmetry used for doping parameters variation simulations.

parameter at time as been changed, in order to study its specific impact on the performance. For each parameter analyzed the overall Efficiency η and the single figures of merit, short-circuit current density J_{SC}, open-circuit voltage V_{OC} and Fill Factor (see eq. (4.1)), are reported and analyzed.

$$\eta = \frac{J_{SC} V_{OC} FF}{P_{in}} \tag{4.1}$$

Simulations were carried out under illumination to estimate the J_{SC} recombination losses and in dark conditions [85] to evaluate the impact of recombination on V_{OC} [86]. A first set of simulation was performed without the texturing, with the front surface planar and covered by ARC. A second set, more representative of actual iBC solar cells, was performed using the texturing described in Chapter 3. The main reason for this choice was to understand if the texturing may have an impact on the optimal doping for each region.

4.2 Planar front surface

The symmetry element showed in fig. 4.1 (without texturing) has been simulated. Pitch was 2 mm and gap 75 μm. The doping profiles in BSF, FSF and Emitter was Gaussian functions of the spatial coordinate featuring the peak located at the edge of the interface and junction depth of 2 μm for BSF and Emitter and 0.5 μm for the FSF region. The simulation parameters assumed was the peak doping concentration of the Emitter $D_{emi,pk}$, the BSF $D_{BSF,pk}$ and the FSF $D_{FSF,pk}$ regions.

4.2.1 FSF region

Fig. 4.2 shows that changes in FSF doping peak $D_{FSF,pk}$ influence markedly the main figures of merit, in particular the J_{SC}. According to the dark analysis illustrated in fig. 4.3, a decrease in the contribution of the total saturation current density due to surface recombination at the Si/SiO_2 interface with increasing $D_{FSF,pk}$. In fact, higher doping peaks lead to relatively more intense electrical field reducing consequently the minority carrier concentration overall in the FSF region. However, for higher $D_{FSF,pk}$ values, the Auger recombination contribution becomes significant. For a cell with simulated parameters the inflection point of the FSF doping is $1 \times 10^{18} cm^{-3}$. It is worth nothing that the increase in SRH and surface recombination current density is marked above this point, due to the dependence of lifetimes and surface recombination velocity on doping concentration.

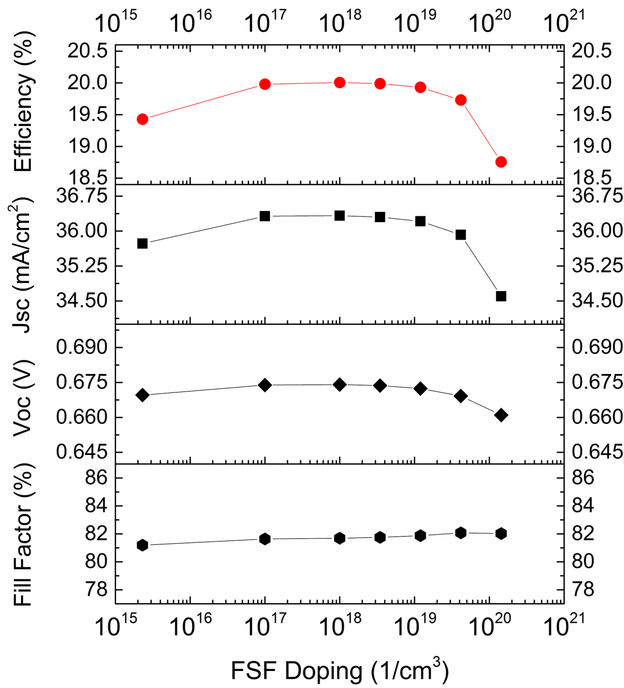

Fig. 4.2 Efficiency, short-circuit current density J_{SC}, open-circuit voltage V_{OC} and Fill Factor for FSF doping peak $D_{FSF,pk}$.

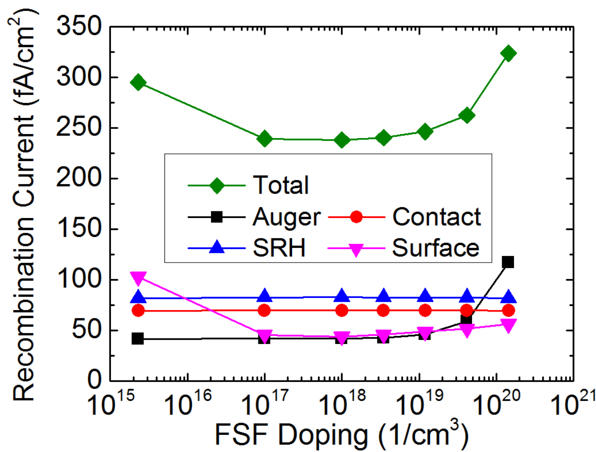

Fig. 4.3 Dark recombination current density components for simulations changing FSF doping peak $D_{FSF,pk}$.

4.2.2 BSF region

Similarly to the case of FSF doping, the change in peak doping concentration of BSF ($D_{BSF,pk}$) has a significant impact on J_{SC}, as shown in fig. 4.4. An increasing trend of J_{SC} is observed with increasing $D_{BSF,pk}$, due to the enhanced effectiveness of the electrical field distribution which prevents minority carrier recombination at the rear contact. This effect leads also to an increase in V_{OC}. However, as it can be seen in fig. 4.5, Auger recombination becomes relevant for BSF doping peaks above approximately $4.16 \times 10^{19} cm^{-3}$.

On the contrary, a negligible influence of $D_{BSF,pk}$ on SRH and surface recombination contribution to the total saturation current density is observed. This can be ascribed to the increase in either carrier doping-dependent lifetime and surface recombination velocity at Si/SiO_2 interface with increasing $D_{BSF,pk}$, which is compensated by a reduction of the amount of excess minority carriers thanks to the relatively stronger electrical field. The trend of the total recombination current is in agreement to those of J_{SC} and V_{OC}. To summarize, for a cell with this characteristics an optimum value of $4.16 \times 10^{19} cm^{-3}$ for $D_{BSF,pk}$ has been determined.

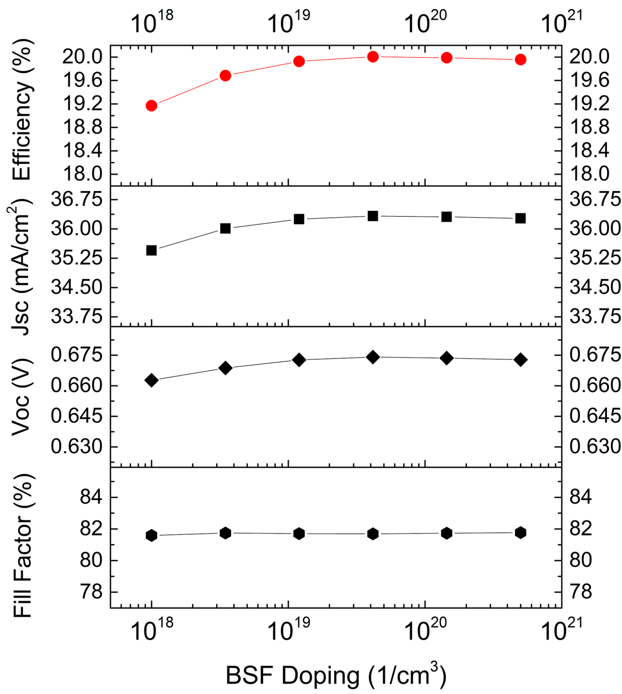

Fig. 4.4 Efficiency, short-circuit current density J_{SC}, open-circuit voltage V_{OC} and Fill Factor for BSF doping peak $D_{BSF,pk}$.

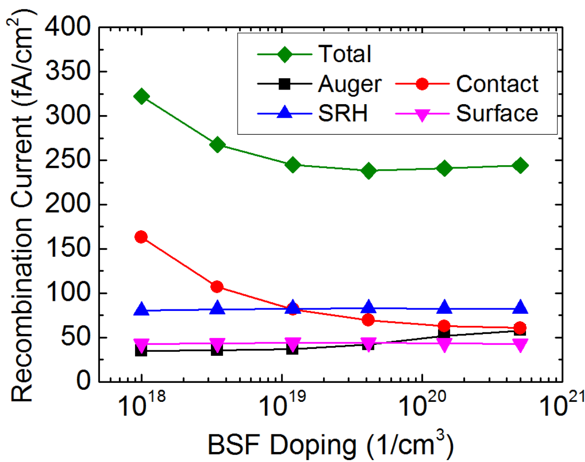

Fig. 4.5 Dark recombination current density components for simulations changing BSF doping peak $D_{BSF,pk}$.

4.2.3 Emitter region

As it can been seen in fig. 4.6, remarkable variations of V_{OC}, FF and consequently of conversion efficiency η occur with increasing peak doping concentration of the emitter diffusion ($D_{emi,pk}$). It is worth noting that the short-circuit current density J_{SC} has a negligible dependence on the peak doping concentration in the emitter region. Indeed, the effects of the doping variation occur in a relatively small region in the rear side of the cell where the carrier photogeneration is the lowest on the solar cell. On the other hand, the FF increases with increasing $D_{emi,pk}$ due to a reduction of the emitter sheet resistance. A trade-off between two competitive mechanisms leads to an optimum $D_{emi,pk}$ value (at approximately $4.16 \times 10^{19} cm^{-3}$) which allows the maximization of the (V_{OC}) efficiency: depletion region width and Auger recombination loss. An increase in doping concentration in emitter region leads to an increase of V_{OC} due to a greater depletion region. However, the decrease in V_{OC} above $D_{emi,pk}$ equal to $4.16 \times 10^{19} cm^{-3}$ is observed; the degradation of V_{OC} is explained by the trend of the saturation current density calculated under dark conditions illustrated in fig. 4.7.

For relatively low emitter doping concentration peaks, the recombination at contacts is the main component of the total recombination, due to a decrease of minority carriers on emitter region caused by a stronger electrical field on the junction; this explains why the SRH and the Surface Recombination exhibit a negligible dependence on $D_{emi,pk}$. However, for peak doping level above $4.16 \times 10^{19} cm^{-3}$, Auger recombination becomes stronger and predominant on the total recombination as we expected in the case of doping profiles exhibiting higher peak concentration. Therefore, a trade-off between electrical field intensity in the junction and Auger recombination rate is observed for a cell with this parameters.

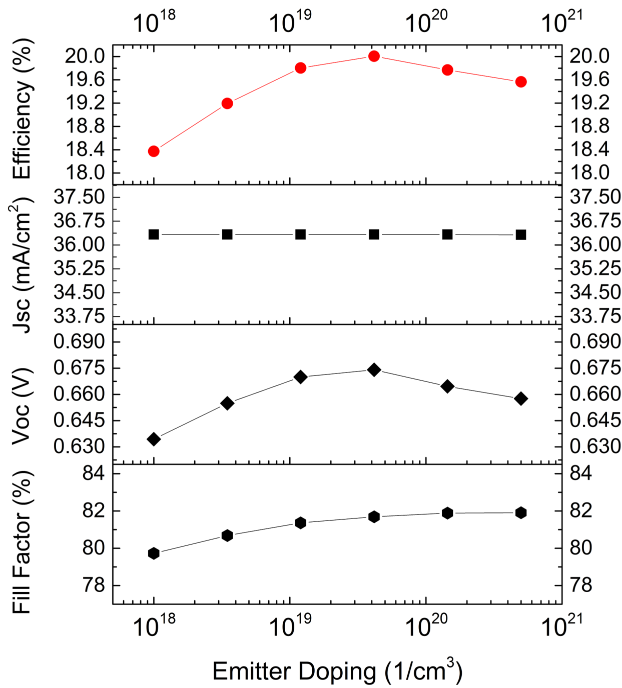

Fig. 4.6 Efficiency, short-circuit current density J_{SC}, open-circuit voltage V_{OC} and Fill Factor for Emitter doping peak $D_{emi,pk}$.

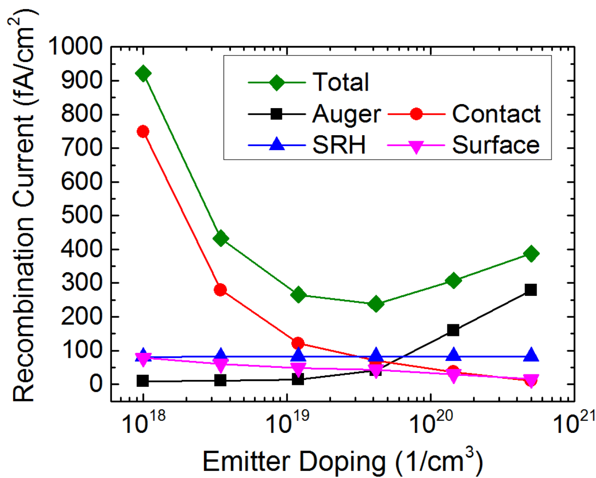

Fig. 4.7 Dark recombination current density components for simulations changing Emitter doping peak $D_{emi,pk}$.

4.3 Textured front surface

The symmetry element showed in fig. 4.1 has been simulated. Pitch was 955 μm and gap 5 μm. The entire space of parameters obtained by varying the doping peak concentration of FSF from $2.31 \times 10^{15} cm^{-3}$ up to $1.44 \times 10^{22} cm^{-3}$, of BSF and emitter from $1 \times 10^{18} cm^{-3}$ up to $5 \times 10^{22} cm^{-3}$ range has been simulated.

The doping profiles in BSF, FSF and Emitter was Gaussian functions of the spatial coordinate featuring the peak located at the edge of the interface and junction depth of 2 μm for BSF and Emitter and 1 μm for the FSF region (see fig. 4.8). The simulation parameters assumed was the peak doping concentration of the Emitter $D_{emi,pk}$, the BSF $D_{BSF,pk}$ and the FSF $D_{FSF,pk}$ regions.

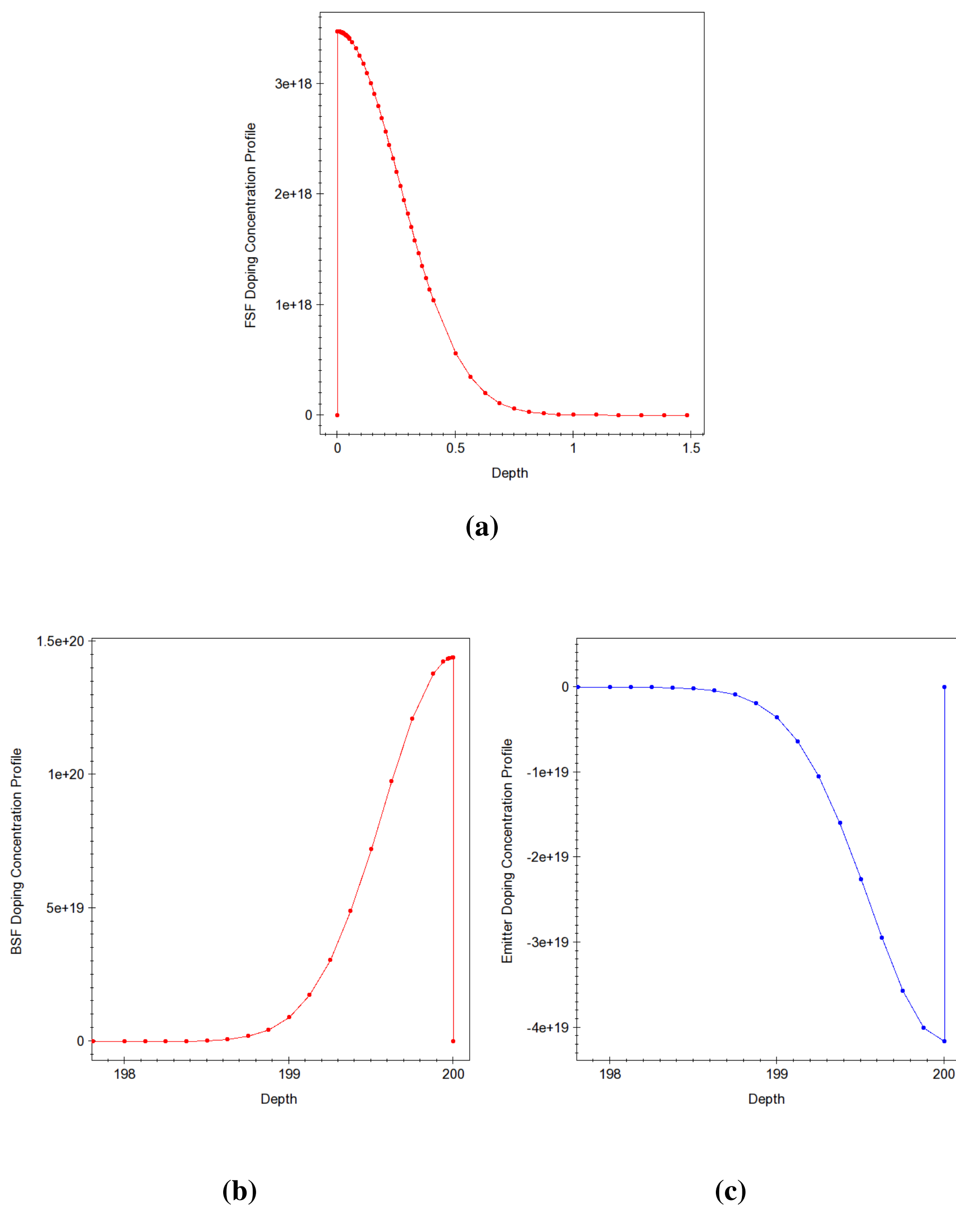

Fig. 4.8 Doping profiles in the three regions: (a) FSF, (b) BSF) and (c) Emitter. Doping peaks value changes through the simulations.

4.3.1 FSF region

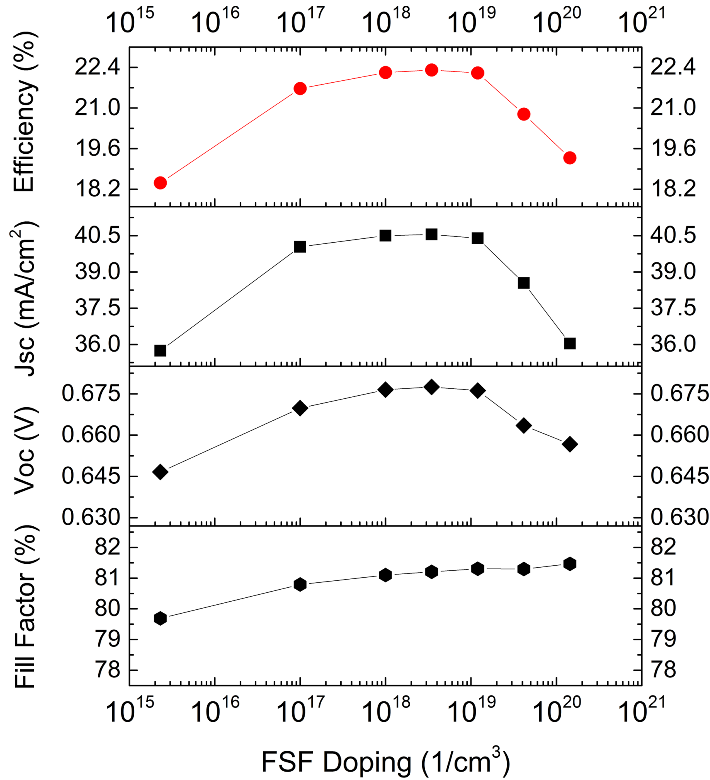

Fig. 4.9 Efficiency, short-circuit current density J_{SC}, open-circuit voltage V_{OC} and Fill Factor for FSF doping peak $D_{FSF,pk}$.Efficiency exhibits a bell-shape with a clear maximum value at doping concentration level of $3 \times 10^{18} cm^{-3}$.

The trends of figure of merit for changes in FSF doping peak $D_{FSF,pk}$ are shown in fig. 4.9. It is possible to observe that the efficiency η exhibits a bell shape, leading to a maximum value for $D_{FSF,pk}$ of $3.48 \times 10^{18} cm^{-3}$, in agreement with the qualitative trends reported in [87]. The behavior of efficiency is determined by the J_{SC} bell shape, which can be explained ,

by the total recombination current density under illumination U-shape, for short-circuit current conditions, as shown in fig. 4.10

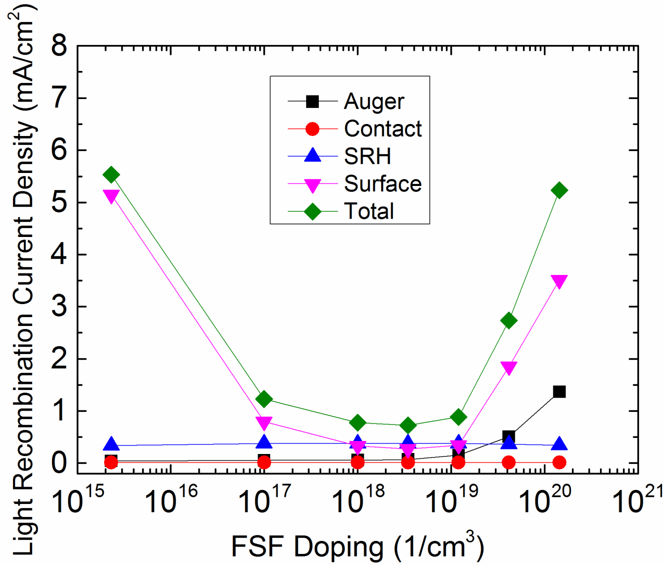

Fig. 4.10 Recombination losses components under illumination in short-circuit conditions explaining J_{SC} behavior, that dominates the efficiency trend in FSF doping peak concentration ($D_{FSF,pk}$) experiment.

The total recombination current density trend is determined by the surface recombination component , i.e. the trap-assisted SRH recombination at the Si/SiO_2 front surface interface. The rate of the surface recombination due to interface defects at the textured front face decreases with increasing doping levels, for doping concentrations below the efficiency peak. In this case, this is caused by the reduction in minority carrier density in the FSF region and at the interface determined by the higher electrical field, as shown in fig. 4.11.

When doping level increases above the efficiency peak, however, the SRH surface recombination becomes stronger again due to the fact that the surface recombination velocity at interface SRV is doping dependent contrasting with the concentration of minority carriers. Moreover, for higher doping peak, a small, but relevant, contribution to the increasing total recombination

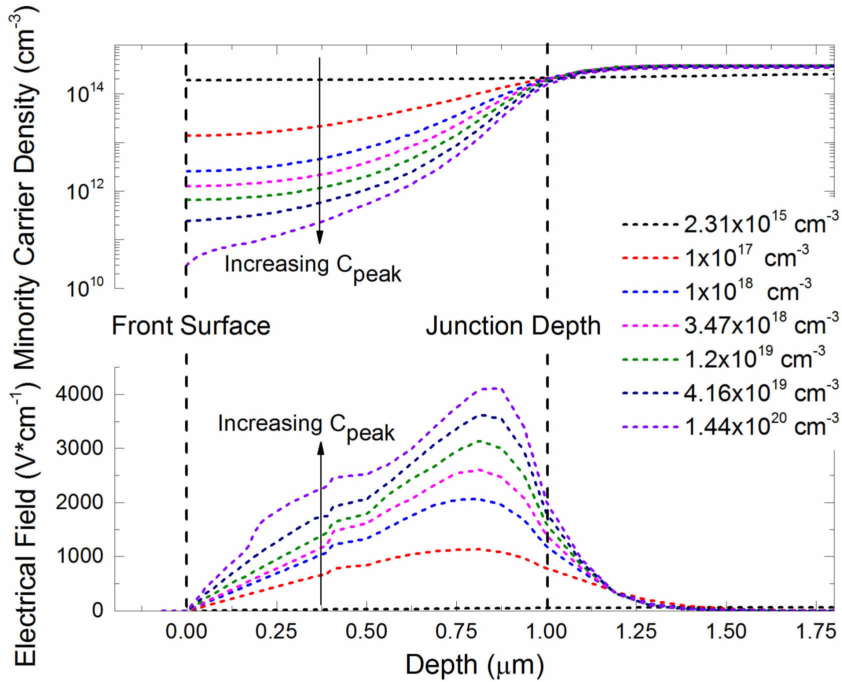

Fig. 4.11 Comparison of minority carrier (hole) density and electrical field intensity for different FSF doping peak concentration at short-circuit condition under illumination in FSF region. Higher FSF doping levels lead to stronger electrical field intensity in the junction depth and to lower minority carrier density values at interface. Depth equal to 0 μm indicates the front interface position.

is due to the Auger recombination, which clearly increase with increasing doping concentration. Finally, an increase in FF trend can be noted, due to the reduction of the series resistance, as reported in [88].

4.3.2 BSF region

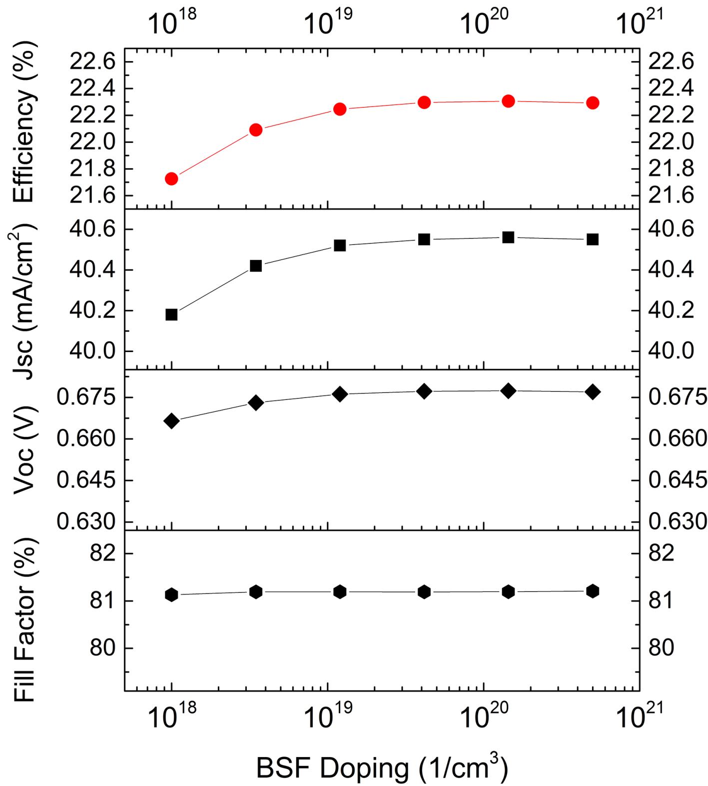

Fig. 4.12 Efficiency, short-circuit current density J_{SC}, open-circuit voltage V_{OC} and Fill Factor for BSF doping peak $D_{BSF,pk}$. Efficiency exhibits a maximum value at doping concentration level of $1.44 \times 10^{20} cm^{-3}$. J_{SC}.

Fig. 4.12 shows the trend of η for different BSF doping peak levels $D_{BSF,pk}$. There is an initial rise for efficiency until a maximum value for $D_{BSF,pk} = 1.44 \times 10^{20} cm^{-3}$ and then a slight decrease. In a similar way than the FSF region, the short-circuit current determines the trend for the overall efficiency. J_{SC} behavior is explained by the mirrored curve of the total recombination current density in short-circuit conditions under light,

showed in fig. 4.13. An increase in the doping level leads to a lowering of the recombination at base contact, leading to an increase in J_{SC} and efficiency. This is ascribed to the reduction of minority carrier density at the Si/Al interface, due to the stronger electrical field intensity with increasing $D_{BSF,pk}$, as can be seen in fig. 4.14. This also leads to the small increase that can be observed in the V_{OC} trend.

For relatively high doping levels, however, the total recombination slightly increase, due to the rise of Auger recombination, which is a doping dependent phenomenon. A trade-off that allows to maximize the efficiency is then achieved for an intermediate doping level.

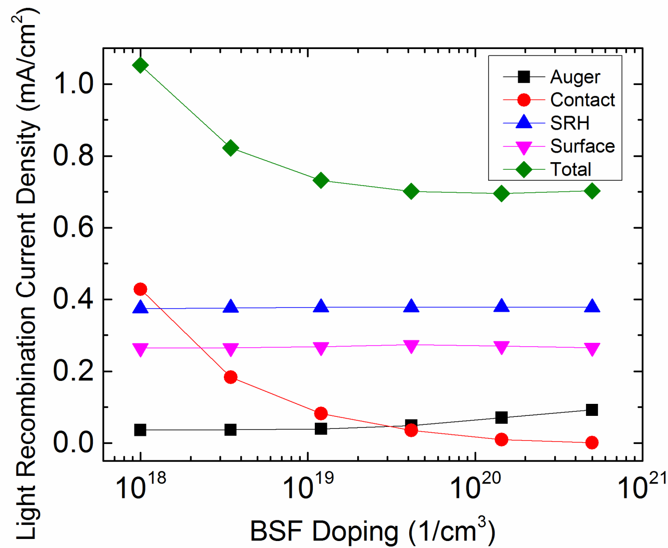

Fig. 4.13 Recombination losses components under illumination in short-circuit conditions explaining J_{SC} behavior, that dominates the efficiency trend in BSF doping peak concentration ($D_{BSF,pk}$) experiment. The increase in Auger recombination for higher $D_{BSF,pk}$ determines a minimum point in Total recombination.

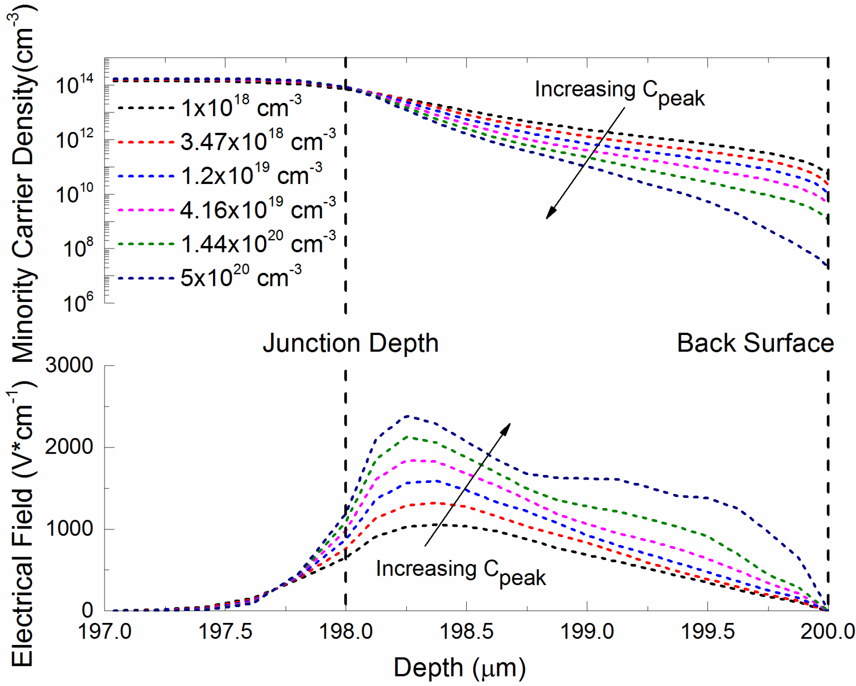

Fig. 4.14 Comparison of minority carrier (hole) density and electrical field intensity for different BSF doping peak concentration at short-circuit condition under illumination in BSF region. Higher BSF doping levels lead to stronger electrical field intensity in the junction depth and to lower minority carrier density values at interface. Depth equal to 200 μm indicates the rear interface position.

4.3.3 Emitter region

In fig. 4.15 are shown the trends for the efficiency and the single FOM as function of emitter doping peak $D_{emi,pk}$. Strong variations of V_{OC} and Fill Factor can be observed. The efficiency η follows a bell shape with a maximum for a $D_{emi,pk}$ value of $4.16 \times 10^{19} cm^{-3}$.

The trend in V_{OC} can be explained by examining the mirrored curve of the total saturation current density in dark condition, showed in fig. 4.16. Two contrasting mechanisms contribute to create the U shape of this current. For low doping, an increase in $D_{emi,pk}$ leads to a decease of the contribution of

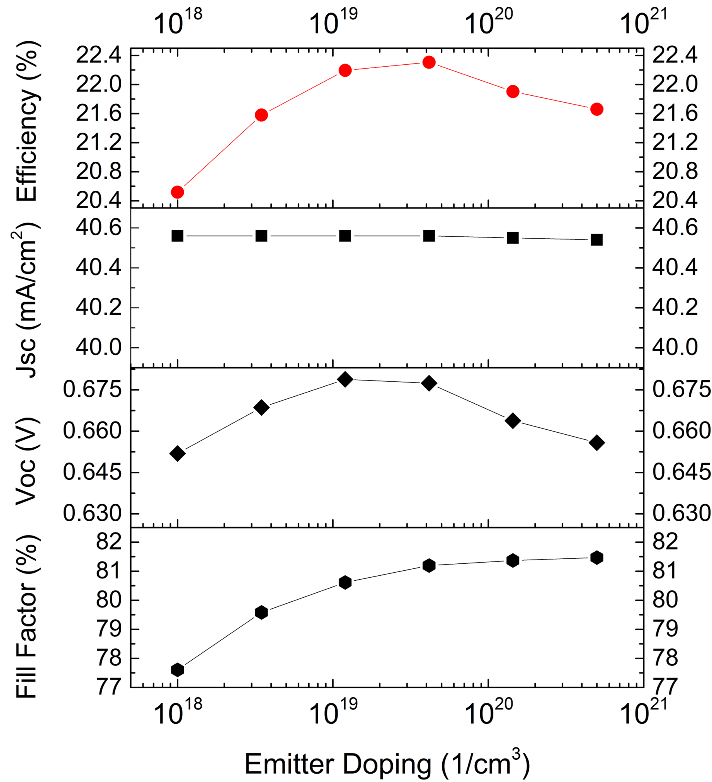

Fig. 4.15 Efficiency, short-circuit current density J_{SC}, open-circuit voltage V_{OC} and Fill Factor for Emitter doping peak $D_{emi,pk}$. Efficiency exhibits a clear maximum value at doping concentration level of $4.16 \times 10^{19} cm^{-3}$.

the recombination at emitter contact, in agreement with King and Swanson [89]. This is determined by the stronger electrical field intensity at the Si/Al interface for higher $D_{emi,pk}$, which results in a reduction of minority carrier density at the contact interface, as can be seen in fig. 4.17 for open-circuit conditions under illumination. For high $D_{emi,pk}$ level, however, Auger recombination contribution becomes significantly stronger and, even in presence of a decrease of surface recombination, predominant over the total recombination process. The trade-off between the two recombination components,

contact for low doping and Auger for high doping, leads to a minimum of the dark saturation current for $D_{emi,pk} = 1.2 \times 10^{19} cm^{-3}$, close to the value reported by Cousins in [90].

However, the total optimum $D_{emi,pk}$ value for maximum efficiency is located higher due to the Fill Factor contribution. Indeed, FF increases with increasing emitter doping peak, due to a reduction of the emitter sheet resistance.

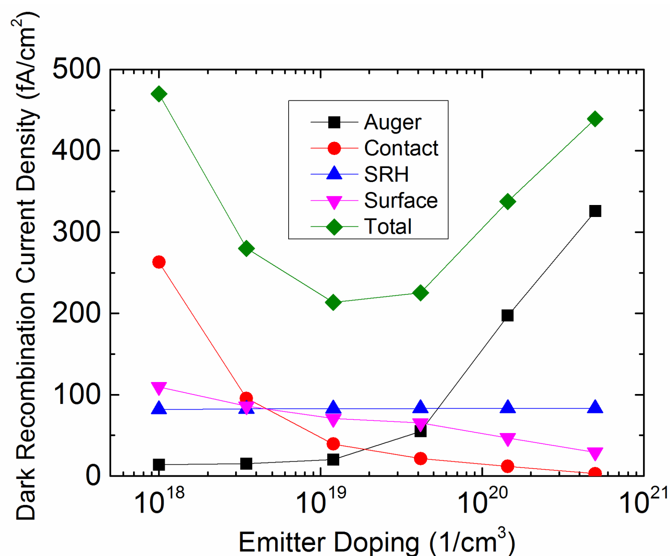

Fig. 4.16 Saturation current competitive components in dark conditions as function of Emitter doping peak $D_{emi,pk}$. The bell shape exhibits a clear minimum point at doping peak concentration $D_{emi,pk} = 1.2 \times 10^{19} cm^{-3}$.

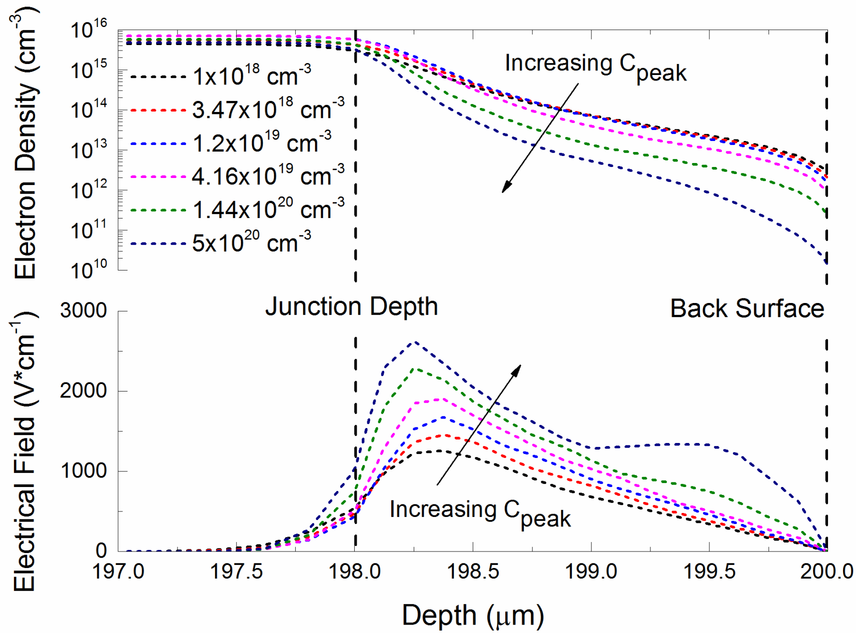

Fig. 4.17 Comparison of electron density and electrical field intensity for different emitter doping peak concentration in open-circuit condition under illumination in emitter region. Higher doping levels lead to stronger electrical field intensity in the junction depth and to lower minority carrier density values at Si/Al interface. Depth equal to 200 μm indicates the rear interface position.

4.4 Conclusions on doping parameters variations

In this chapter, an extensive study of the impact of the doping parameters of the three main doped regions, Emitter FSF and BSF, has been presented. The trends simulated have been explained in depth and related with a complete analysis of the recombination currents, detailed in their components.

For the planar front surface structure the efficiency curve as a function of doping exhibits a bell shape with a clearly identifiable optimum value for the three doping regions. In our simulated structure, the optimum values of peak doping are: $4.16 \times 10^{19} cm^{-3}$ for emitter, $4.16 \times 10^{19} cm^{-3}$ for BSF and $1 \times 10^{18} cm^{-3}$ for FSF. The efficiency decrease observed at lower doping

values is explained in terms of higher contact recombination for BSF and emitter, and in terms of higher surface recombination for FSF. The efficiency decrease observed at higher doping values is explained in terms of higher Auger recombination for all cases. Therefore, the optimum doping peak value is result of the trade-off between surface recombination at silicon interfaces and Auger recombination losses. This means that is expected that the optimum peak doping should change depending on the quality of the passivation at interfaces Si/SiO_2 and Si/Al.

Even for the textured front surface cell the simulated trends reveal that the efficiency curve as a function of doping in all the three regions examined exhibits a bell shape with a specific maximum value for the three regions. The efficiency degradation for lower doping values is explained in terms of higher contact recombination for BSF and emitter, and in terms of higher SRH surface recombination for FSF. The efficiency decrease observed at higher doping values is explained in terms of higher Auger recombination for BSF and emitter, and in terms of SRH surface recombination losses for FSF. For the simulated solar cell, the values of peak doping that maximize the efficiency η are: $4.16 \times 10^{19} cm^{-3}$ for emitter, $1.44 \times 10^{20} cm^{-3}$ for BSF and $3.48 \times 10^{18} cm^{-3}$ for FSF.

Making a comparison between the planar and the textured front surface some considerations can be done. In all cases, the lower efficiency reported for the planar surface can be ascribed to the reduction of short-circuit current J_{SC} due to the absence of texturing on the front and therefore the higher reflectance and lower photogenerated current. With respect to the FSF doping peak the optimum maximum is shifted because, for higher doping peaks, in the planar structure the dominant recombination is the Auger, while in the textured structure, since the much higher surface recombination velocity SRV, the prevailing recombination is the surface recombination component. The overall trends in both cases of planar and textured front surface are the same, and thus in terms of fabrication guidelines, if the passivation of

the front surface can be realized with sufficient quality, the inclusion of the texturing step ensures over 2% points more in efficiency and it is strongly recommended.

Chapter 5

Optimization of geometrical parameters

In this chapter the performance of the simulated solar cell will be analyzed with respect to geometrical variations of the main regions of the simulated domain. The behavioral trends resulting will be detailed and explained, providing informations about the best fabrication guidelines to obtain increased efficiency.

5.1 Simulation methodology

In fig. 5.1 is represented the symmetry element simulated with the indication about the parameters variated in this chapter. The characteristics of the cells are the same reported in Chapter 4, therefore: FZ-Si *n*-type doped wafer, with a thickness of 200 μm (except for the thickness variations simulation set), with a resistivity of 2 Ω·cm; ohmic contact of 100 μm without potential barrier, resistivity of 2 Ω·cm^2 and recombination velocity for carriers at metal/Si interface of 1 $\times 10^6$ cm/s. Doping has been considered fully ionized and activated. The geometrical parameters considered are: Gap between BSF and Emitter, BSF width W_{BSF}, Emitter width W_{emi} and the Pitch, i.e.

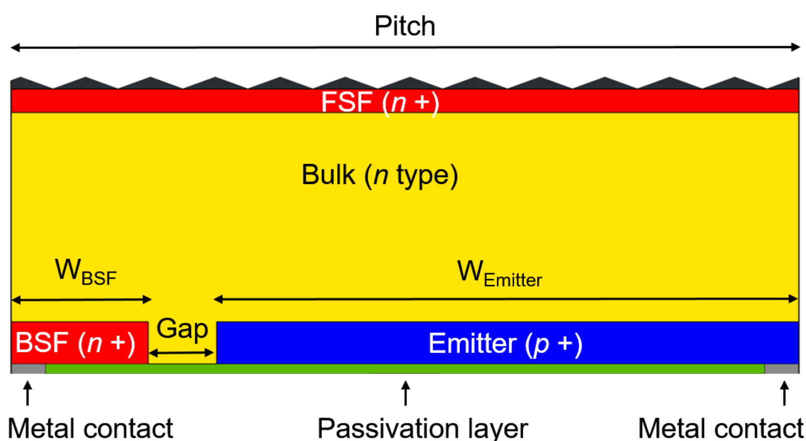

Fig. 5.1 Element of symmetry used for doping parameters variation simulations.

the distance between the centers of the contacts, that defines the size of the symmetry element.

For this kind of simulations, the geometries of the rear face regions are linked, thus a variation in one parameter leads to the variation of another. For each simulation the geometries changing are described. As for Chapter 4, for each parameter analyzed the overall Efficiency η and the single figures of merit, short-circuit current density J_{SC}, open-circuit voltage V_{OC} and Fill Factor, are reported and analyzed. All the simulations were performed under illumination to determine the J_{SC} recombination losses. Like the previous chapter two sets of simulation were performed: without the texturing, with the front surface planar and covered by ARC, and with the texturing and ARC.

5.2 Planar front surface

The symmetry element showed in fig. 4.1 (without texturing) has been simulated. The doping profiles in BSF, FSF and Emitter was Gaussian functions

of the spatial coordinate featuring the peak located at the edge of the interface and junction depth of 2 $/mu$m for Emitter and BSF and 0.5 μm for the FSF region and a peak doping concentration of $4.16 \times 10^{19} cm^{-3}$ for Emitter, $4.16 \times 10^{19} cm^{-3}$ for BSF and $1 \times 10^{18} cm^{-3}$ for FSF. The simulation parameters assumed was the width of the Gap, the width the Emitter W_{emi} with respect to Pitch, and the Pitch size.

5.2.1 Gap width

For this analysis the Gap has been changed along with the BSF width W_{BSF}, keeping constant emitter width W_{emi} and pitch.

The change of the gap size has an impact on all figures of merit as shown in fig. 5.2. A degradation of J_{SC} with increasing gap can be observed, due to the poor effectiveness of the electrical field which allows minority carrier recombination at the rear interface in gap region. In the same way, this leads to a slight decrease in V_{OC} that can be explained in terms of saturation current increase. The contribution of surface recombination becomes more important for higher gap due to the weaker electrical field as can be seen in fig. 5.3.

In addition, FF drops due to an increase of series resistance explained by the higher resistivity in gap region (lower doping) compared with BSF region (higher doping).Gap variation influence over efficiency is mainly due to recombination losses at gap interface and the higher efficiency is obtained with the smallest gap possible, even if the trend is not linear. In fact for gap smaller than 10 μm the efficiency trend tends to become constant.

This is behavior is strongly dependent on the quality of passivation on the rear surface, in particular on the gap region. The surface recombination velocity, and therefore the surface recombination current, can be greatly reduced with a good passivation, and in this case the main cause of losses will be the decrease in Fill Factor due to the different resistances between bulk and BSF region.

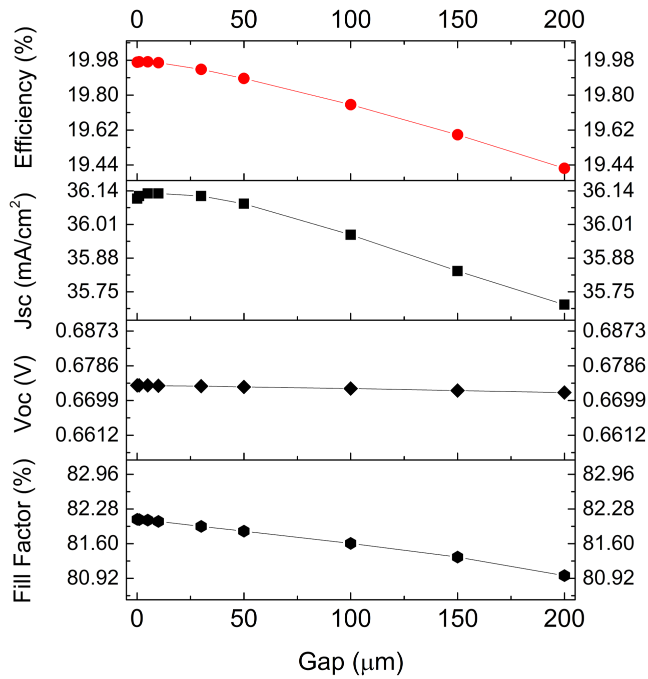

Fig. 5.2 Efficiency, short-circuit current density J_{SC}, open-circuit voltage V_{OC} and Fill Factor for gap width variations.

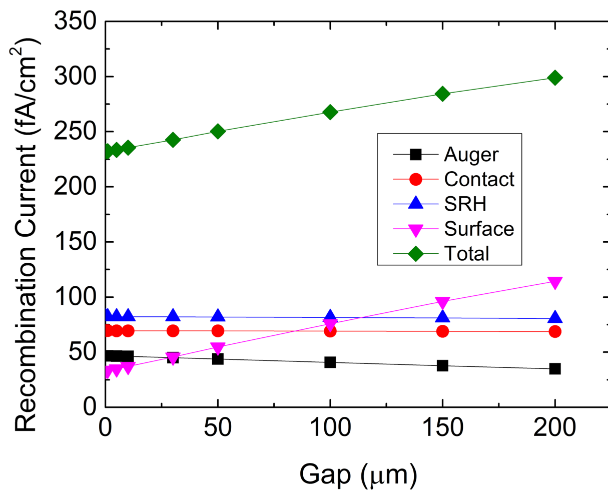

Fig. 5.3 Dark recombination current density components for simulations changing gap width.

5.2.2 Emitter width

For this analysis the emitter width W_{emi} and the BSF width W_{BSF} has been changed at the same time, keeping constant pitch and gap. To better describe the trends the *emitter coverage* R, i.e. the ratio between the emitter and the total pitch, is defined as:

$$R = \frac{W_{emi}}{Pitch} \tag{5.1}$$

The change of R has a significant impact on J_{SC} as it is shown in fig. 5.4. An increasing trend of J_{SC} with increasing emitter/pitch ratio can be observed, due to a larger *pn*-junction that enhances the effectiveness of the electrical field over bulk region preventing minority carrier recombination in this region and enhancing their collection. It is worth noting that FF and V_{OC} have the opposite behavior of J_{SC}. Degradation of V_{OC} can be explained by recombination currents as shown in fig. 5.5. The contribution of the surface recombination becomes significant for higher values of emitter/pitch ratio since surface recombination contribution of emitter is stronger than BSF because different doping species lead to different SRV.

In the same way, FF trend is explained by a trade-off between emitter and BSF sheet resistivity.With the simulated parameters, the impact of the V_{OC} and FF due to recombination and resistive losses becomes significant at higher emitter/pitch ratio and there is a slight optimum point around 0.84. It means that there is an optimum ratio due to a trade-off among a larger *pn*-junction, quality of passivation in rear Si/SiO_2 interface and BSF and emitter sheet resistance. In conclusion, W_{emi} has to be as higher as possible, depending on the quality of passivation in the rear of the cell, and at the same time W_{BSF} as smaller as the BSF contact allows.

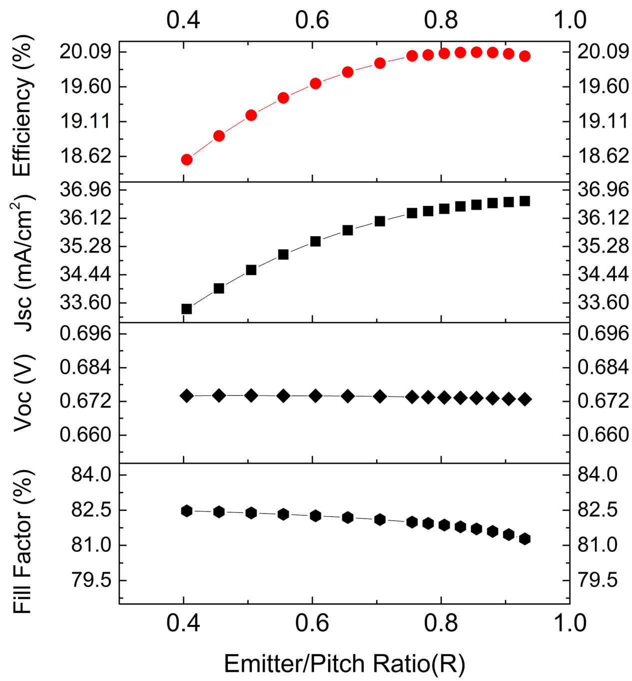

Fig. 5.4 Efficiency, short-circuit current density J_{SC}, open-circuit voltage V_{OC} and Fill Factor for emitter/pitch ratio R variations.

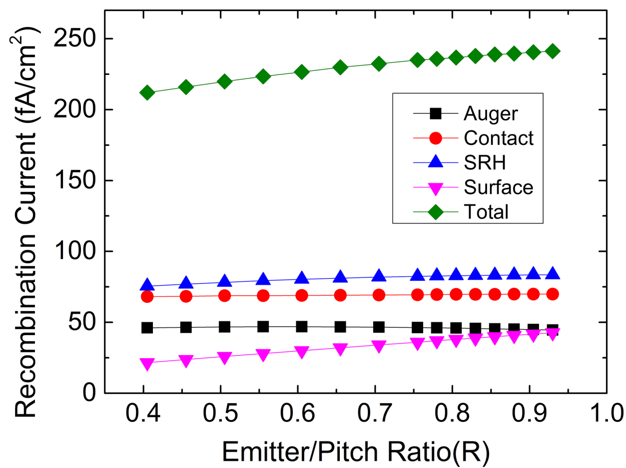

Fig. 5.5 Dark recombination current density components for simulations changing emitter/pitch ratio R.

5.2.3 Pitch width

For this analysis simulations changing pitch, i.e the size of the symmetry element and the distance between contacts, has been performed. W_{emi} and W_{BSF} were changing at the same time, keeping constant emitter/pitch ratio R and gap.

The change on pitch has a significant impact on FF as shown in fig. 5.6. A degradation of FF with increasing pitch longitude can be observed, due to the increase of series resistance, because the mean path for minority carriers to be collected increase in all regions: FSF, BSF, emitter and bulk. Increment on V_{OC} can be explained in terms of recombination current (see fig. 5.7), in fact there is a reduction of the contact recombination component due to a smaller portion of the pitch covered by contact region (it occurs because while pitch is changing contact width is kept constant). The changes over J_{SC} are small and can be explained by the trade-off between photocurrent generation and recombination losses in bulk region.

In conclusion, even if the V_{OC} increase with increasing pitch, this effect is not strong enough to compensate the FF reduction, so the greater efficiency is obtained for smaller pitch.

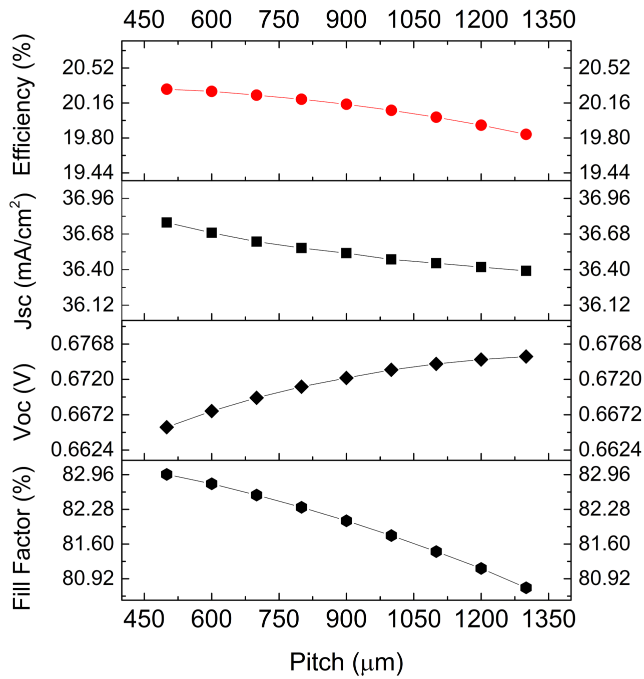

Fig. 5.6 Efficiency, short-circuit current density J_{SC}, open-circuit voltage V_{OC} and Fill Factor for pitch size variations.

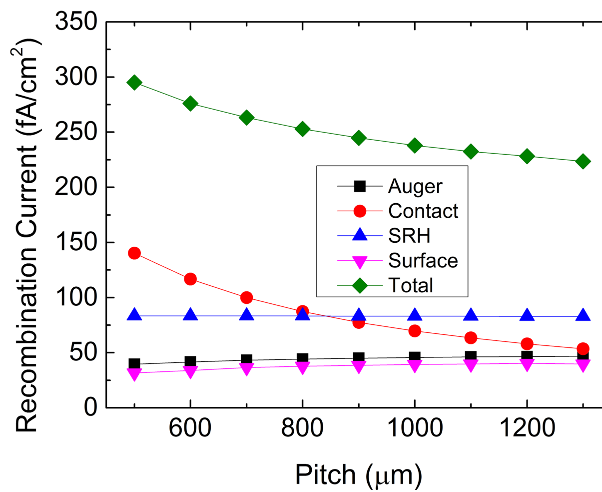

Fig. 5.7 Dark recombination current density components for simulations changing pitch size.

5.3 Textured front surface

The symmetry element showed in fig. 5.1 has been simulated. The doping profiles in BSF, FSF and Emitter was Gaussian functions of the spatial coordinate featuring the peak located at the edge of the interface and junction depth of 2 μm for BSF and Emitter and 1 μm for the FSF region (see fig. 4.8). The doping peak concentrations for the three regions have been set to the best values found in Chapter 4, in order to maximize the efficiency, and then to $4.16 \times 10^{19} cm^{-3}$ for emitter, $1.44 \times 10^{20} cm^{-3}$ for BSF and $3.48 \times 10^{18} cm^{-3}$ for FSF The simulation parameters assumed was the width of the Gap, the width the Emitter W_{emi} with respect to Pitch, the Pitch size and the thickness of the cell.

5.3.1 Gap width

The simulation has been performed by changing the BSF region width W_{BSF} and gap width at the same time, keeping constant the pitch (1000 μm) and the emitter width W_{emi} (725 μm). The surface recombination velocity for carriers (SRV) on gap was assumed as 25cm/s for base doping concentration according to [62]. Fig. 5.8 shows that for increasing gap width the total efficiency decreases. The principal cause to this behavior is the evident degradation of the Fill Factor. Since increasing the gap determines a reduction of the BSF region, which has a much lower resistivity, the trade-off between the resistance of the two regions explains the Fill Factor degradation for longer gap.

The J_{SC} shows no dependence on the gap variation, but this is explained observing fig. 5.9. The light recombination current behavior is the result of two competing components: as the gap increases, the surface recombination current increases, due to the reduction of the shielding effect of electrical field for wider gaps. On the other hand, increasing the gap in this configuration leads to a decrease of the BSF region volume, and then, since it is more heavily

doped, to a decrease in the Auger recombination. In a similar way the slight increase in V_{OC} can be explained, because in this case the effect of the Auger recombination reduction has more impact than the surface recombination increase.

The increase in trap-assisted recombination at interface depends on the decreasing of the electrical field created by the BSF which prevent minority carriers to arrive to the surface. The effect of defects at rear interface, expressed in terms of SRV, become critical for large gap regions, as reported in [80] [91]. If the defectivity of the interface is relatively high a degradation in J_{SC} and V_{OC} can be expected cause the of the more relevant surface recombination current component. In general, longer gaps lead to efficiency degradation due to both resistive and recombination losses, confirming the results reported in [92]. However, the gap must be kept large enough to prevent shunting between the emitter and BSF regions, that can results, depending on the fabrication process accuracy, in high resistive losses.

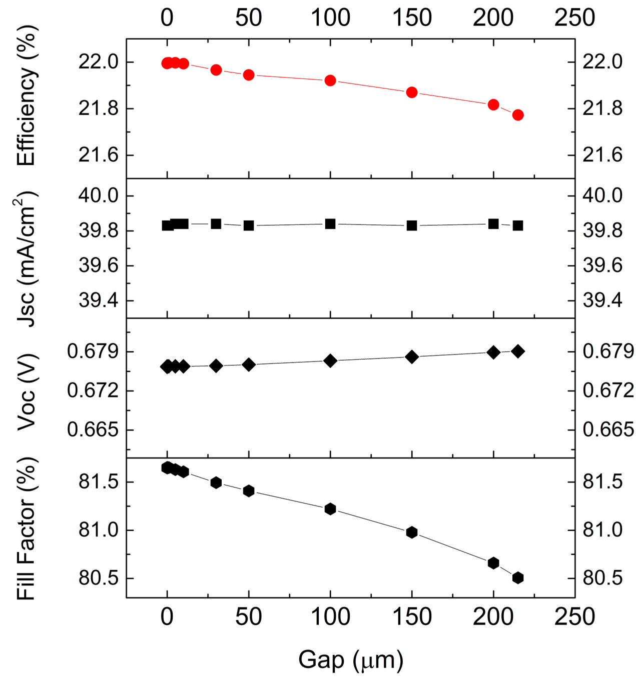

Fig. 5.8 Efficiency, short-circuit current density J_{SC}, open-circuit voltage V_{OC} and Fill Factor for gap width variations.

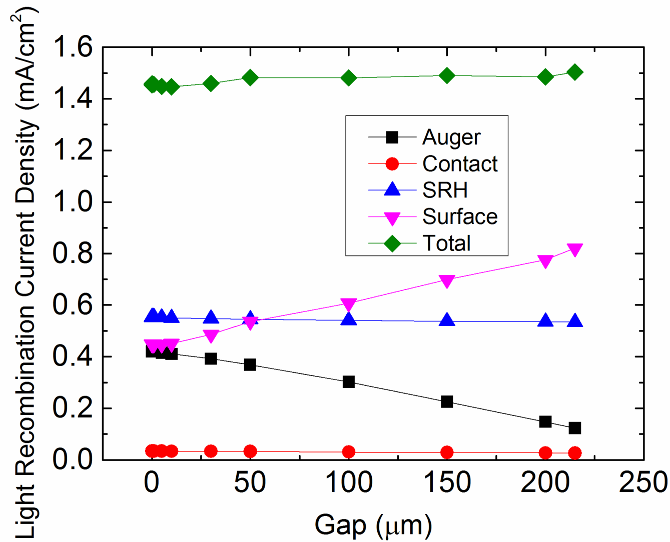

Fig. 5.9 Light recombination current density components for simulations changing gap width.

5.3.2 Emitter width

The simulation has been performed by changing the emitter width W_{emi} and the BSF region width W_{BSF} at the same time, keeping constant the pitch (1000 μm) and the gap (5 μm). Fig. 5.10 shows the trends of the FOM as function of the emitter/pitch ratio R (or emitter coverage), defined in the previous section (see eq. 5.1). Given this configuration, as R becomes higher, emitter width W_{emi} increases and BSF width W_{BSF} decreases.

The efficiency rise up with increasing emitter coverage ip to the value of 0.85 then slightly decreases. Observing the single FOM trends is straightforward to ascribe the improved efficiency to the J_{SC} increasing trend [93], while the reduction for higher R is due to Fill Factor reduction. The increment of short-circuit current can be explained observing the light recombination current density shown in fig. 5.11. As the emitter coverage increases, both SRH recombination current components (bulk and surface) as long as Auger recombination current decrease, because of the lower doping concentration in the emitter region with respect to the BSF region ($D_{emi,pk}$ is lower than $D_{BSF,pk}$).

The degradation of the Fill Factor can be explained considering the different resistivity of the emitter region with respect to the BSF region. Due to the different doping levels, emitter resistivity $\rho_{emi} = 42.76\Omega/\Box$ is higher than the BSF resistivity $\rho_{BSF} = 9.67\Omega/\Box$ and then, since increasing R determines, at the same time, an increment in the emitter volume and a reduction in the BSF volume , the total resistance increases. For the characteristic of the simulated cell an optimum value $R = 0.85$ has been found. However, since the optimum value depends on the lateral transport resistance it is influenced by the bulk resistivity an additional study has been carried out and it is reported in the next section.

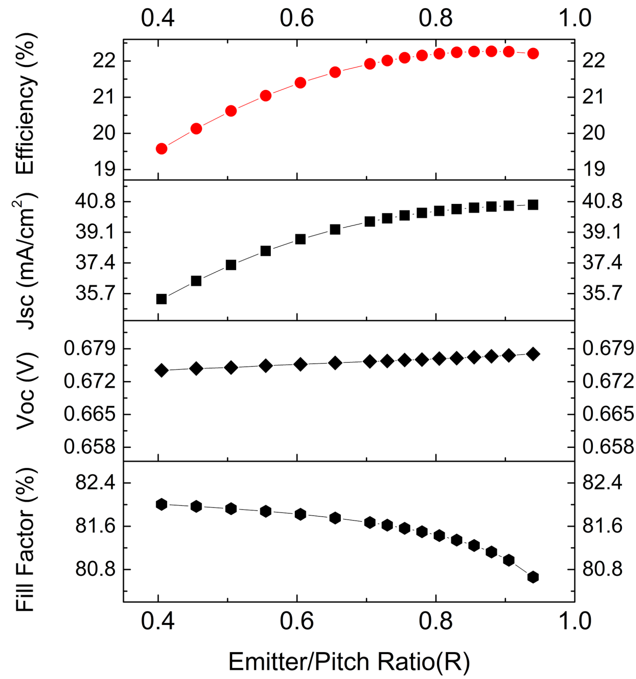

Fig. 5.10 Efficiency, short-circuit current density J_{SC}, open-circuit voltage V_{OC} and Fill Factor for emitter/pitch ratio R variations.

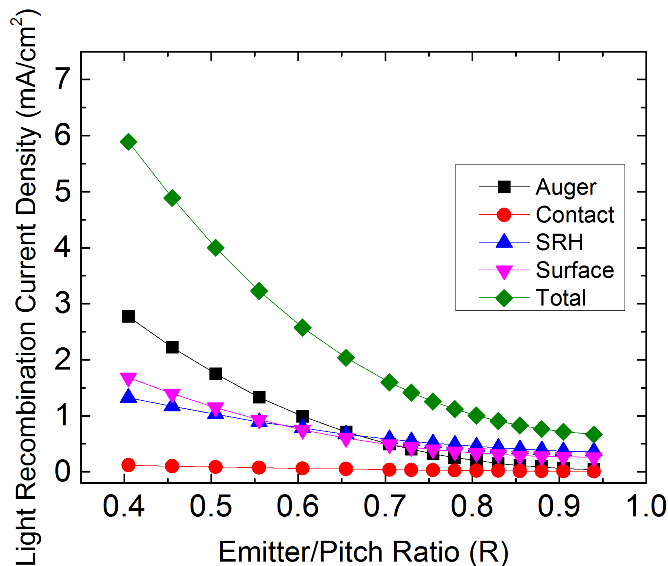

Fig. 5.11 Light recombination current density components for simulations changing emitter/pitch ratio R.

5.3.3 Optimum Emitter coverage

Several works have suggested different optimum values of emitter coverage ratio R_{opt} to reach maximum efficiencies [94] [95] ranging between 0.7 and 0.9. This optimum value is explained by electrical shadow and series resistance losses balance [96] as seen in the previous section. To better understand this parameter dependences and trends a set of simulation was performed considering the following parameter ranges: emitter and BSF doping peak from 1×10^{18} to $1 \times 10^{21} cm^{-3}$, BSF width from 55 μm to 300 μm, emitter width from 90 μm to 1600 μm, two different bulk resistivity values of 1 $\Omega \cdot cm$ and 10 $\Omega \cdot cm$. The main investigated parameter was R_{opt}, which represents the value of R required to maximize the efficiency for each analysis, performed by fixing some parameters and varying the others. Therefore, R_{opt} is a relative optimum and not the absolute optimum. Fig. 5.12 illustrates R_{opt} as a function of emitter and BSF doping keeping constant pitch and emitter width, for different values of BSF width and bulk resistivity. R_{opt} is clearly dependent on the emitter and BSF doping, as well as on the bulk doping, and to get the highest efficiency it may ranges in a wide interval between 0.6 and 0.95. For low resistive substrates the highest efficiencies are reached with very wide emitter, up to more than 90% of the pitch size. It is quite interesting to note that even for very high resistivity substrates it is possible to reach almost the same efficiencies, but using smaller emitter coverage, around 70% of the pitch, since in this case the Fill Factor degradation effect is more relevant.

For the next analysis doping levels were fixed to to optimum values for emitter and BSF: $D_{emi} = 1.58 \times 10^{19} cm^{-3}$ and $D_{BSF} = 2.51 \times 10^{20} cm^{-3}$ for 1 $\Omega \cdot cm$ bulk resistivity and $D_{emi} = 1.58 \times 10^{19} cm^{-3}$ and $D_{BSF} = 6.31 \times 10^{19} cm^{-3}$ for 10 $\Omega \cdot cm$ bulk resistivity.

Fig. 5.13 illustrates results from simulations that were performed to analyze R_{opt} as a function of pitch, BSF and emitter width for fixed doping levels reported above and for two different values of bulk resistivity. R_{opt}

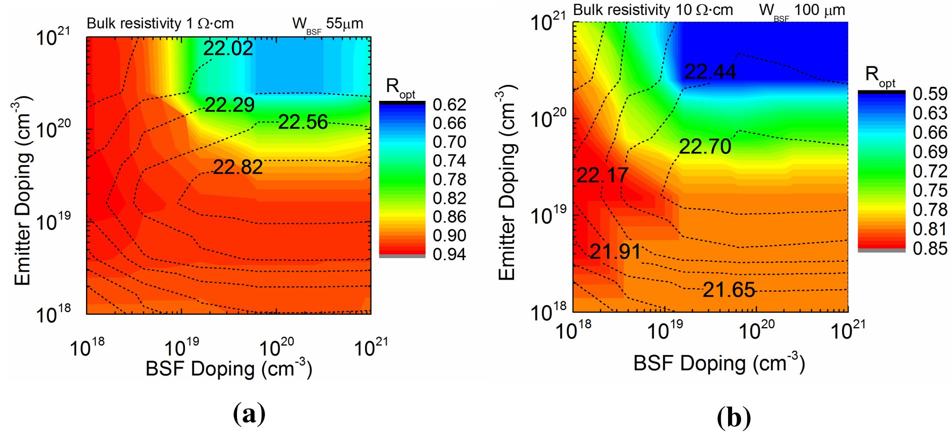

Fig. 5.12 R_{opt} dependence from BSF and emitter doping for bulk resistivity of (a) 1 $\Omega \cdot cm$ and (b) 10 $\Omega \cdot cm$. Dotted lines illustrate calculated efficiencies.

significantly increases with pitch and emitter width, while it significantly decreases with BSF width, ranging again in a wide interval between 0.6 and 0.95. In the case of a bulk resistivity of 1 $\Omega \cdot cm$ (10 $\Omega \cdot cm$), the absolute maximum efficiency is 23.08 (22.96) corresponding to R_{opt} of 0.91 (0.81).

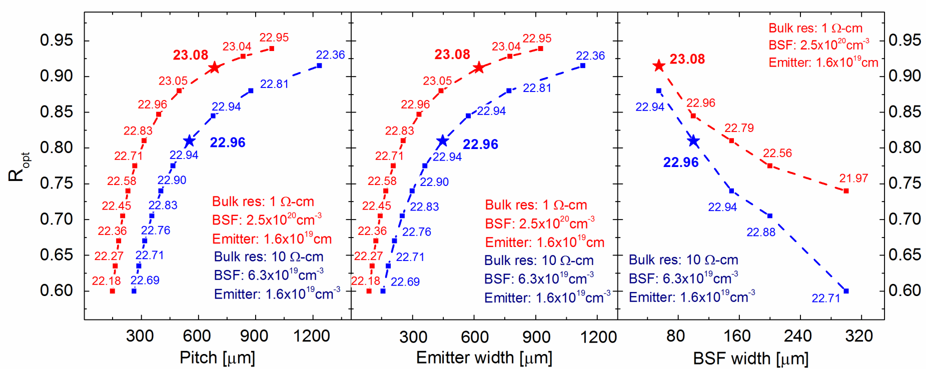

Fig. 5.13 Calculated R_{opt} for different values of pitch (left), emitter width (middle) and BSF width (right). Numbers above points are calculated efficiencies. Starred point is the highest simulated efficiency.

Fig. 5.14 illustrates efficiency as a function of BSF and emitter width keeping constant BSF and emitter doping levels for different values of bulk resistivity. It is worth noting that the BSF and the emitter width can be optimized independently one another. In the case of a bulk resistivity of $1\ \Omega \cdot cm$ ($10\ \Omega \cdot cm$), the optimum BSF width is 55 μm (100 μm) and the optimum emitter width is 646 μm (448 μm). These optimum values are obtained as a trade-off between electrical shading and series resistance effects. The electrical shading losses decrease by increasing the emitter width and by reducing the BSF width, while the series resistance losses increase by increasing the emitter width and by reducing the BSF width. By comparing fig. 5.14a and 5.14b, it is evident that by increasing the bulk resistivity, the optimum BSF width increases due to the stronger contribution of bulk to total series resistance losses.

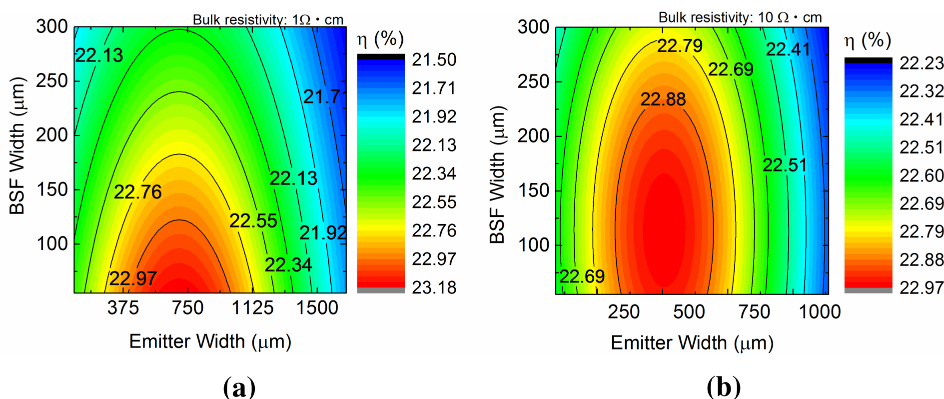

(a) **(b)**

Fig. 5.14 Simulated efficiency dependence from BSF and emitter width for a bulk resistivity of (a) $1\ \Omega \cdot cm$ and (b) $10\ \Omega \cdot cm$. In both cases, the BSF and the emitter width can be optimized independently one another.

To summarize, R_{opt} exhibits a strong dependence on emitter and BSF doping levels, pitch, emitter and BSF width, and bulk resistivity, ranging between 0.6 and 0.95. From the geometry design perspective, it is more effective optimizing independently the BSF and emitter width, than optimizing R at fixed pitch or BSF width. In the case of a bulk resistivity of $1\ \Omega \cdot cm$ (10

$\Omega \cdot cm$), an absolute maximum efficiency of 23.08 (22.96) for BSF width of 55 μm (100 μm) and emitter width of 646 μm (448 μm) has been obtained, which give a pitch of 706 μm (553 μm) and R_{opt} of 0.91 (0.81).

5.3.4 Pitch width

The simulation has been performed by changing the Pitch size, keeping constant the emitter/pitch ratio R to 0.85 and the gap to 5 μm and scaling the symmetry element to consequence.

Fig 5.15 shows that efficiency significantly decreases with increasing pitch, mainly because of the Fill Factor reduction. This is a consequence of the increase in series resistance due to the widening distance between contacts [97]. The minimum simulated pitch was 500 μm because going to lower values would have implied a BSF width smaller than the defined contact size. Thus, the maximum efficiency has been found for the smallest pitch size, as reported in [91] [96] [98].

The reduction in short-circuit current can be explained observing the light recombination currents. Indeed, as fig. 5.16 shows, the increase in pitch affects all the recombination current components, and this can be ascribed to the effect of electrical shading [93]. The increase in V_{OC} can be explained noting that contact size was kept constant in all the experiments. This caused a lower contact recombination current contribution for larger pitch sizes and, while the effect on J_{SC} is negligible, this had a much stronger impact on the V_{OC} behavior.

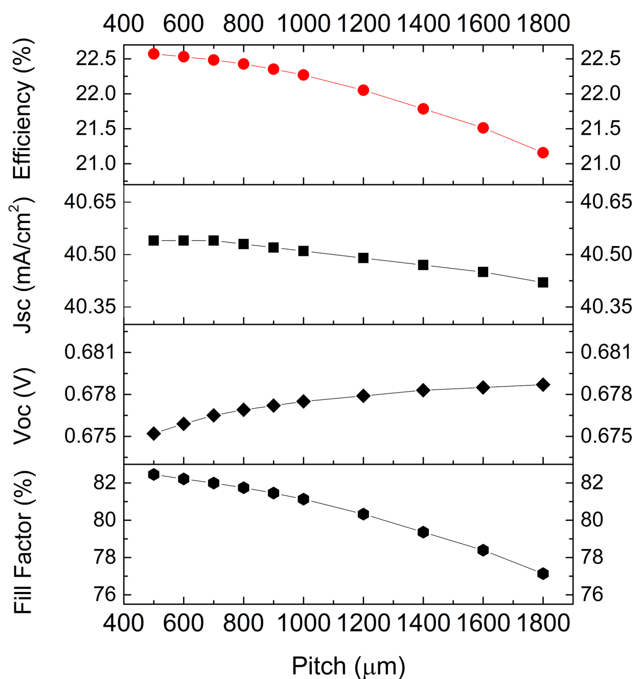

Fig. 5.15 Efficiency, short-circuit current density J_{SC}, open-circuit voltage V_{OC} and Fill Factor for pitch size variations.

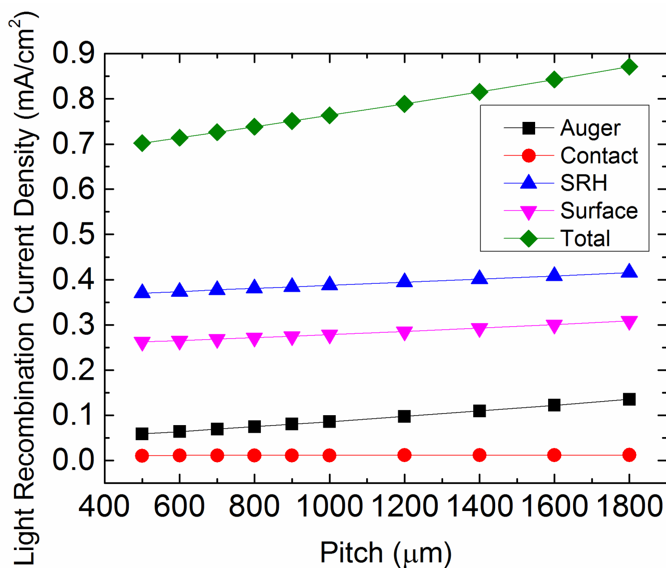

Fig. 5.16 Light recombination current density components for simulations changing pitch size.

5.3.5 Substrate thickness

The simulation has been performed by changing the substrate thickness of the cell D_{sub}, keeping constant the pitch (1000 μm), emitter/pitch ratio R to 0.85 and the gap to 5 μm.

Fig. 5.17 shows that efficiency strongly grows for increasing thickness from $50\mu m$ to $200\mu m$, in agreement with the results reported in [99], but then start to decrease. The main cause for the raising part of the trend is the increase in the short-circuit current J_{SC}, that follows the increase in the photogenerated current, shown in the figure. This is due to a longer optical path for the incident light, which allows to capture a larger fraction of the less energetic, long wavelength photons.

However, although the trend of the photogenerated current continues to grow for thicker substrates (even if at slower rate), after $D_{sub} = 200\mu m$ the short-circuit current decreases. This is due to a reduction either in the J_{SC} and in the V_{OC}, that happens because the effect of SRH recombination in the bulk starts to become significant, due to the longer path that carriers generated near the front surface need to travel before being collected at the contacts (see fig. 5.18). From this analysis, for a cell with the simulated parameters, the optimum substrate thickness has been determined to be $200\mu m$.

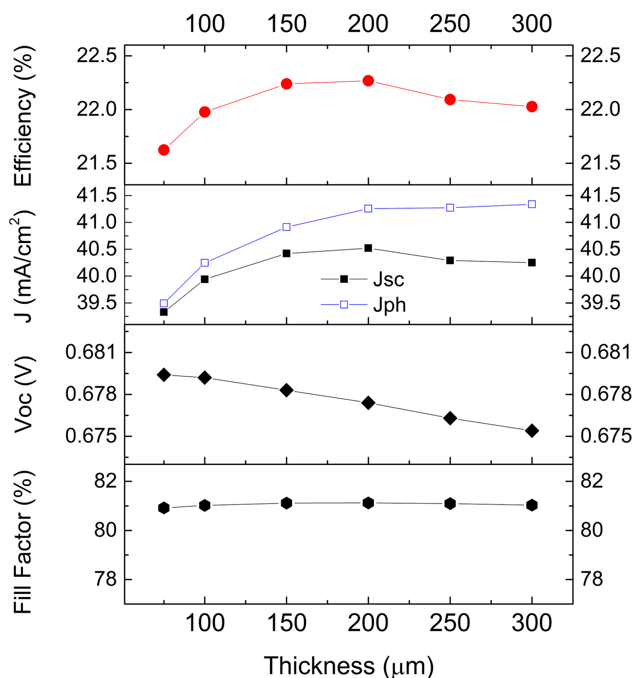

Fig. 5.17 Efficiency, short-circuit current density J_{SC}, open-circuit voltage V_{OC} and Fill Factor for substrate thickness variations.

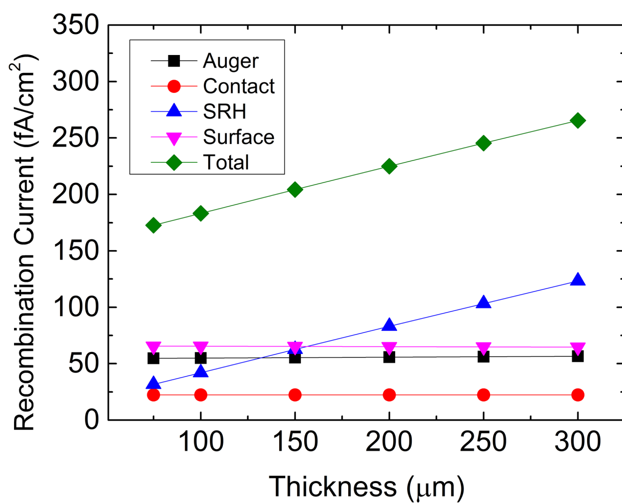

Fig. 5.18 Dark recombination current density components for simulations changing substrate thickness.

5.4 Double Emitter contact

One of the most challenging problems related to iBC architecture is the losses due by the electrical shading effect. The electrical shading effect is the result of a reduced minority charge carrier collection probability because of an increased recombination in the non-collecting base area, composed of the BSF and the gap [80]. In order to mitigate these losses, it is necessary to reduce the non-collecting base region and to extend the emitter width coverage until a certain optimal width, which is just before when the series resistance adversely affects the Fill Factor and starts to reduce the efficiency, as explained in a previous section.

A possible solution is to introduce a second emitter contact line, that improves the minority carrier collection providing a shorter path to the p contact and therefore reducing series resistance losses, especially for longer emitter regions. The simulated structure is shown in fig. 5.19, using a 200 μm substrate of 5 $\Omega \cdot cm$ resistivity, and doping peaks of the three regions $D_{emi,pk} = 5 \times 10^{19} cm^{-3}$, $D_{FSF,pk} = 3.47 \times 10^{18} cm^{-3}$ and $D_{BSF,pk} = 1.7 \times 10^{20} cm^{-3}$.

To improve the understanding of the metal-silicon contact a parameter called *emitter metal coverage* f has been introduced, representative of the fraction of the emitter contacted by metal.

$$f = \frac{2W_C}{W_{emi}} \tag{5.2}$$

where W_C is the single contact width.

A first set of experiments was performed by fixing $W_{emi} = 1200 \mu m$, and by varying the metallization fraction f from 0.002 to 0.25 (which means that W_C ranges from 1.2 μm to 150 μm) and the distance between the two emitter contacts normalized with respect to the emitter width (d/W_{emi}) from 0 to 0.875,(0 corresponds to a single contact case). It is worth noting that the two contacts are located symmetrically to the emitter center. The purpose of this

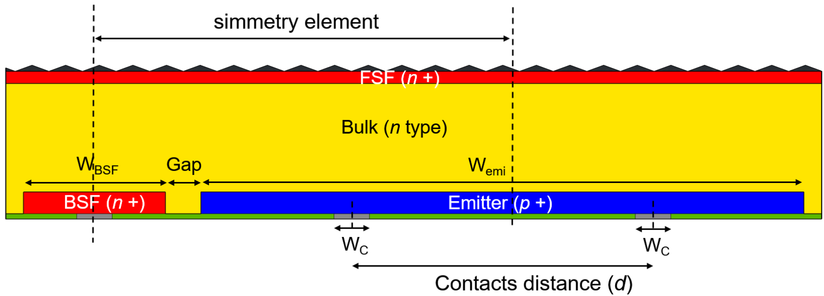

Fig. 5.19 Sketch of the simulated iBC solar cell with double emitter contact.

experiment was to reach the optimum distance between the contacts d and the most favorable emitter width Wc.

A second round of experiments was performed by keeping fixed $W_C = 5\mu m$ and by varying W_{emi} from 400 to 2200 μm for the emitter single and double contact cases, in order to investigate the effect of the second contact for different emitter sizes especially for the long emitter cases. In both sets of experiments, the resistance of the contact lines has been neglected, but was verified that this assumption is reasonable for the explored range of W_C.

Fig. 5.20 shows the efficiency and Fill Factor as a function of f and d/W_{emi} for a fixed $W_{emi} = 1200\mu m$. From this figure, it is possible to see that higher efficiency values are observed at smaller W_C. This effect is ascribed to the lowering of the contact recombination when the contact size is reduced.

The optimum position for smaller f is in the middle of the emitter symmetry element ($d/W_{emi} = 0.5$). When f increases, the higher efficiency values are obtained when the contacts are away from each other. This effect can be explained because the contact recombination increases as W_C rises, but changing the contacts position is a feasible way to maintain the Fill Factor value high as possible. Indeed, the series resistance is lower when the BSF

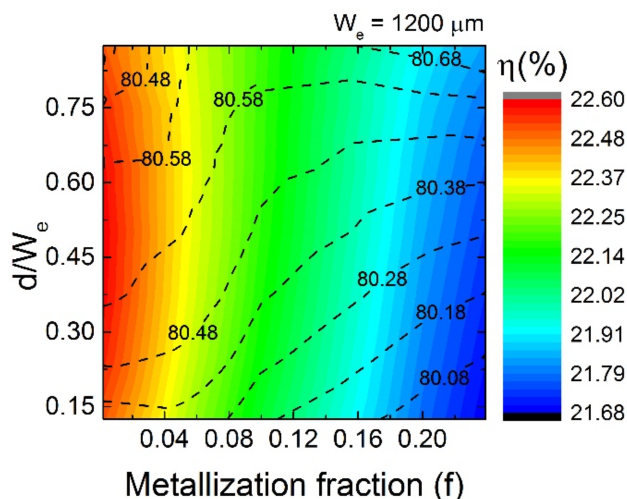

Fig. 5.20 Efficiency (color scale) and FF (dotted lines) as a function of f and d/W_{emi} for a fixed $W_{emi} = 1200\mu m$.

contact and the emitter contact are closer to each other, but just enough before V_{OC} degrades too much.

Fig. 5.21 shows efficiency comparison between the emitter single contact structure (dashed line), and a two contacts structure (solid line) as a function of d/W_{emi} with $W_{emi} = 1200\mu m$. For both structures f=0.0083 (that is $W_C = 4.98\mu m$ for double contact and $W_C = 9.96\mu m$ for single contact). A clear maximum point can be observed when $d/W_{emi} = 0.5$ for the double contact case. This effect is explained by the Fill Factor trend due to series resistance degradation. The addition of the second contact significantly improves the solar cell efficiency for longer emitters.

Fig. 5.22 is shown a comparison of the overall efficiency and the single figures of merit as a function of W_{emi} between single and double emitter contact with $d/W_{emi} = 0.5$. The efficiency exhibits a bell shape trend as a function of W_{emi} for both structures. As W_{emi} increases in size, two competitive effects are observed: on one hand, the V_{OC} increases, but on the other side the fill facto

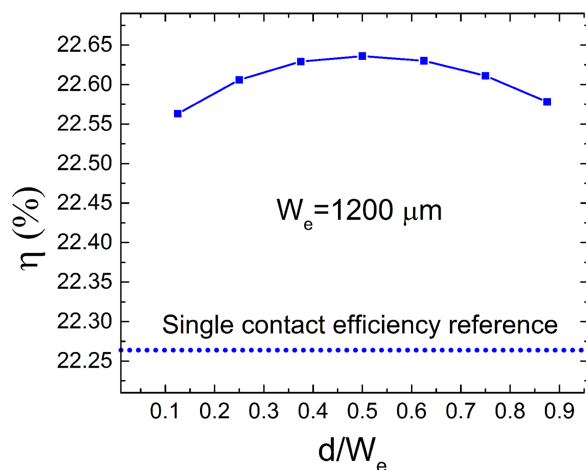

Fig. 5.21 Efficiency as a function of d/W_{emi} (dotted line represents the efficiency in case of single emitter contact).

is reduced due an increment of the series resistance. The maximum efficiency is observed at $W_{emi} = 400\mu m$ for both structures. Since this optimum value depends on the metallization fraction of the emitter region, by using larger contacts this optimum W_{emi} value increases. It is worth noting that in spite of the degraded V_{OC} due to higher surface recombination, the double emitter contact solar cell exhibits an improved efficiency.

To summarize, the addition of a second contact line on the emitter region strongly improves the iBC solar cell performance because of the reduced impact of the series resistance associated with long emitter regions [61]. At low values of the metallization fraction, the optimum position for the double contact emitter is observed in the middle of the emitter symmetry element. Efficiency exhibits a bell shape trend as a function of W_{emi} for both structures. The efficiency degradation at lower W_{emi} is ascribed to the lower V_{OC} while the efficiency degradation at higher W_{emi} is due to the Fill Factor degradation. By assuming a $W_C = 5\mu m$, the maximum efficiency is observed at $W_{emi} = 400\mu m$ in both structures.

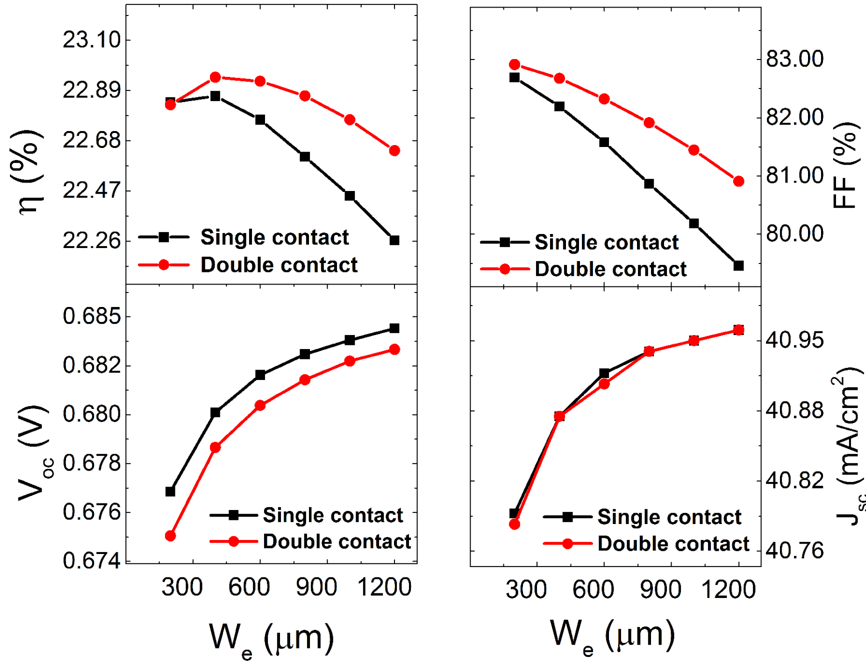

Fig. 5.22 Efficiency and figures of merit as a function of W_{emi} with single and double contact at emitter region, $W_C = 5\mu m$.

5.5 Conclusions on geometrical parameters

Many geometrical parameters of an iBC solar cell have been analyzed and the corresponding trends have been detailed.

For the case of planar front surface, the main parameter to be considered is the longitude of the emitter, because it defines the extension of the *pn*junction, thus the width of minority carriers collection zone. Then the pitch longitude which defines the fill factor due to series resistance losses. Finally, gap and BSF widths have an impact on surface recombination losses. From these considerations, higher values of efficiency are reached for: a)larger emitters/pitch ratio, b)smaller pitches, c)smaller BSF and gap.

In the case of textured front surface, with respect to the gap width between emitter and BSF regions, a degradation of efficiency have been observed for wider gaps, due to SRH surface recombination and resistive losses. Regarding the emitter/pitch ratio R a bell shape has been found. For small R, efficiency reduction is due to higher recombination losses (SRH and Auger recombination) because of the higher minority carrier density given the reduced junction electrical field, while for large R the resistive losses in the emitter region with respect to the BSF region determines a decrease in efficiency. For the a cell with the simulated parameters an optimum emitter/pitch ratio of 0.85 has been found.

However, this value is not absolute, since a deeper analysis on optimum emitter coverage pointed out its dependence not only on the cell geometry, but also on the BSF, emitter and bulk resistivities, concluding that the optimum emitter coverage is a function of the fabrication process constraints.

Regarding the pitch size, from the simulation was observed a reduction of the efficiency for larger pitch, mainly due to the increasing resistive losses causing a Fill Factor degradation. Lastly, an analysis on the substrate thickness has been performed, resulting in an optimum value of $200\mu m$ for an iBC solar cell with the simulated parameter, due to the cross point between photogeneration and bulk recombination.

Comparing the planar and textured front surface structures, as in the previous chapter, the relatively lower values for the simulated efficiencies can be ascribed to the lower short-circuit currents, due to poorer light absorption and thus lower photogeneration. In the gap width analysis, in both cases to smaller gaps corresponded better performance, however the reason is different. In the textured case the main source of losses was the Fill Factor degradation for larger gap due to trade-off between gap and BSF resistance. This happened also in the planar case, but together with a strong short-circuit current due to the higher surface recombination current related to an higher value of SRV used in the simulation. This means that, in terms of fabrication design, even if

it is possible to achieve a good passivation on the back surface, it is still quite important to reduce the gap width between emitter and BSF regions to keep an higher efficiency. In all the analyzed cases, the optimization trends for gap width, emitter/pitch ratio and pitch size was the same, making strongly recommended the introduction of a texturization step during the fabrication process, given the possibility to obtain over 2% more in efficiency.

Lastly, a variation on the geometry of the metal contacts of the emitter has been proposed and analyzed, resulting in a very promising improvement in the efficiency due to the reduced series resistance effect.

Conclusions

The key point for the world-wide diffusion and application of the photovoltaic technology as one of the main sources of energy is the production of low cost, high efficiency solar cells. The recent year developments have made this goal more relevant than ever and the approach has moved to the research for ever more efficient cells. The PV market is dominated by crystalline silicon devices and thus the research on this material is of fundamental importance to have the most distributed and wide enhancements. Since both the most efficient laboratory silicon solar cell and the most commercial photovoltaic module are based on the back-contact architecture, an insight of this kind of structure may be very useful to improve the production guidelines.

In order to conduct an optimization process, the simulation approach has proven to be very effective. The main reasons are: first, the cost of a simulation optimization is drastically lower than the optimization obtained by repeated fabrication and characterization steps, and second, the study conducted through simulations allows to determine in an highly detailed way all the processes occurring inside the cell and to point out the loss mechanisms, both in nature and in position.

In this work of thesis a crystalline silicon interdigitated back-contact (iBC) solar cell has been studied and analyzed using multidimensional simulations conducted with a TCAD software. Many design parameter variations have been applied and their impact on the performance of the solar cell has been detailed and explained.

In the first part of the thesis an overall view on the physics of a solar cell, along with the illustration of the architecture object of this study has been presented. Then, the modeling process applied for the analysis has been detailed, defining all the physical models used to ensure the accuracy of the simulation results.

In the second part a wide range of fabrication parameters have been analyzed, both in doping and geometries. Not only their effects on the total efficiency have been illustrated, but also the specific loss mechanisms that limit the efficiency have been pinpointed and investigated. With respect to the doping parameters of the three main regions of an iBC solar cell, bell-shapes have been found in efficiency, determining an optimum doping peak for each region. As for the geometrical design, the effect of wider gap and pitch has been found to be detrimental, while the definition of an optimum emitter coverage has been determined to be not absolute but subjected to the single regions resistivity. Finally, a proposed architecture with double contacts for the emitter region has been proved to be very effective in the enhancement of the efficiency.

All the analysis carried out provides useful knowledge on the behavior of an iBC solar cell, as well as design guidelines to the optimization of its architecture, with the aim of increase the solar conversion efficiency and reduce the production cost of this kind of solar cell.

References

[1] Intergovernmental Panel on Climate Change. Climate change synthesis report, 2014.

[2] IPCC. Climate change: The scientific basis, 2001.

[3] UNFCC. Adoption of the Paris agreement, 2015.

[4] S. Vaclav. Energy at the crossroads, 2006.

[5] International Energy Agency (IEA). Key World Energy Statistics, 2016.

[6] Ren21. Renewable global status report, 2016.

[7] Deutsche Bank Markets. 2014 outlook: Let the second gold rush begin, 2014.

[8] Fraunhofer ISE: Photovoltaics Report, updated: 20 October 2016.

[9] K. Masuko, M. Shigematsu, T. Hashiguchi, D. Fujishima, M. Kai, N. Yoshimura, T. Yamaguchi, Y. Ichihashi, T. Yamanishi, T. Takahama, M. Taguchi, E. Maruyama, and S. Okamoto. Achievement of more than 25% conversion efficiency with crystalline silicon heterojunction solar cell. *IEEE Journal of Photovoltaics*, 4:1433–1435, 2014.

[10] SunPower. SunPower TM X-Series data sheet, 2013.

[11] Synopsys. Inc. *Sentaurus Device User Guide*, 2012.

[12] A. Luque and S. Hegedus. *Handbook of Photovoltaic Science and Engineering*. Wiley, 2010.

[13] A. E. Becquerel. Memoire sur les effets electriques produits sous l'influence des rayons solaires. *Les Compte Rendus des L'academie des sciences*, 9:561–567, 1839.

[14] National Renewable Energy Laboratory. Reference Solar Spectral Irradiance: Air Mass 1.5. http://rredc.nrel.gov/solar/spectra/am1.5/.

[15] M. A. Green and M. J. Keevers. Optical properties of intrinsic silicon at 300k. *Progress in Photovoltaics*, 3(3):189–192, 1995.

[16] H. Schlangenotto, H. Maeder, and W. Gerlach. Temperature dependence of the radiative recombination coefficient in silicon. *Physica Status Solidi A 21a*, pages 357–367, 1974.

[17] W. Shockley and W. Read. Statistics of the recombinations of holes and electrons. *Physical Review*, 87(5):835, 1952.

[18] R. N. Hall. Electron-hole recombination in germanium. *Physical Review*, 87(2):387–387, 1952.

[19] D. J. Roulston, N. D. Arora, and S. G. Chamberlain. Modeling and measurement of minority-carrier lifetime versus doping in diffused layers of n+ -p silicon diodes. *IEEE Transactions on Electron Devices*, 29(2):284–291, 1982.

[20] R. Pierret and G. Neudeck. *Modular Series on Solid State Devices, Volume VI: Advanced Semiconductor Fundamentals*. Addison-Wesley, 1987. Chap. 6.

[21] D. B. M. Klaassen. A unified mobility model for device simulation i. model equations and concentration dependence. *Solid-State Electronics*, 35(7):953–959, 1992.

[22] C. Hu and R. M. White. *Solar Cells: From Basics to Advanced Systems*. McGraw Hill, London, 1983.

[23] A. G. Aberle. *Crystalline Silicon Solar Cells: Advanced Surface passivation and Analysis*. UNSW, Sydney, Australia, 1999.

[24] M. Green. *Solar Cells: Operating Principles, Technology and System Applications*. Prentice Hall, 1982. Chap. 5.

[25] K. Bucher, J. Bruns, and H. G. Wagemann. Absorption coefficient of silicon: An assessment of measurements and the simulation of temperature variation. *Journal of Applied Physics*, 75(2):1127–1133, 1994.

[26] W. Shockley and H. J. Queisser. Detailed balance limit of efficiency of p-n junction solar cells. *Journal of Applied Physics*, 32(3):510–519, 1961.

[27] A. De Vos. *Endoreversible Thermodynamics of Solar Energy Conversion*. Oxford University, Oxford, 1992.

[28] A. Richter, M. Hermie, and S.W. Glunz. Reassessment of the limiting efficiency for crystalline silicon solar cells. *IEEE Journal of Photovoltaics*, 3(4), 2013.

[29] M. A. Green, K. Emery, Y. Hishikawa, W. Warta, and E.D. Dunlop. Solar cell efficiency tables (version 48). *Progress in Photovoltaics: Research and Applications*, 24(7):905–913, 2016.

[30] P. W. Bridgman. Certain physical properties of single crystal of tungsten, antimony, bismuth, tellurium, cadmium, zinc and tin. *Proceedings of the American Academy of Arts and Sciences*, 60(6):305–383, 1925.

[31] K.Wolfgang, A. Müller, H.U. Höfs, I.A. Schwirtlich, and C. Häßler. Planar solidification of multicrystalline silicon for phtovoltaic applications. In *Gettering and Defect Engineering in Semiconductor Technology VII*, volume 57 of *Solid State Phenomena*, pages 401–412. Trans Tech Publications, 1997.

[32] T. Nishinaga. *Handbook of Crystal Growth: Fundamentals (2nd edition)*. Elsevier, 2015.

[33] J. Zhao, A. Wang, P. Campbell, and M. A. Green. A 19.8% efficient honeycomb multicrystalline silicon solar cell with improved light trapping. *IEEE Transactions on Electron Devices*, 46(10):1978–1983, 1999.

[34] M. Spiegel, C. Gerhards, F. Huster, W. Jooss, P. Fath, and E. Bucher. Industrially attractive front contact formation methods for mechanically v-textured multicrystalline silicon solar cells. *Solar Energy Materials and Solar Cells*, 74(1–4):175–182, 2002.

[35] Y. Inomata, K. Fukui, and K. Shirasawa. Surface texturing of large area multicrystalline silicon solar cells using reactive ion etching method. *Solar Energy Materials and Solar Cells*, 48(1):237 – 242, 1997.

[36] S. Gandhi. *VLSI Fabrication Principles*. John Wiley & Sons, New York, 1994. Chap. 9.

[37] B. Richards, J. Cotter, C. Honsberg, and S. Wenham. Novel uses of tio2 in crystalline silicon solar cells. *28th IEEE Photovoltaic Specialist Conf*, pages 375–378, 2000.

[38] R. Van Overstraeten and R. Mertens. *Physics, Technology and Use of Photovoltaics*. Adam Hilger Ltd, Bristol, 1986. Chap. 4.

[39] 19.4% efficient large-area fully screen-printed silicon solar cells. *ISFH*. http://www.isfh.de/institut_solarforschung/industrienahe-siebdrucksolarzelle.php?_l=1.

[40] H. McHugo, S. A.and Hieslmair and E. R. Weber. Gettering of metallic impurities in photovoltaic silicon. *Applied Physics A*, 64(2):127–137, 1997.

[41] M. A. Green. Silicon solar cells: at the crossroads. *Progress in Photovoltaics: Research and Applications*, 8(5):443–450, 2000.

[42] D. Macdonald and L. J. Geerligs. Recombination activity of interstitial iron and other transition metal point defects in p- and n-type crystalline silicon. *Applied Physics Letters*, 85(18):4061–4063, 2004.

[43] S. Martinuzzi, O. Palais, M. Pasquinelli, and F. Ferrazza. n-type multicrystalline silicon wafers and rear junction solar cells. *European Physical Journal-Applied Physics*, 32(3):187–192, 2005.

[44] T. Saitoh, H. Hashigami, S. Rein, and S. Glunz. Overview of light degradation research on crystalline silicon solar cells. *Progress in Photovoltaics: Research and Applications*, 8(5):537–547, 2000.

[45] T. Werner. Analyst day. *Sunpower Inc.*, page 24, 2015.

[46] J.M. Rodríguez, I. Tobías, and A. Luque. Random pyramidal texture modelling. *Solar Energy Materials and Solar Cells*, 45(3):241 – 253, 1997.

[47] M. A Green. *Silicon Solar Cells; Advanced Principles and Practice*. Center for Photovoltaic systems and devices, UNSW, Sydney, 1995.

[48] J. Zhao, A. Wang, and M. A. Green. 24.5 efficiency perl cells on fz substrates. *Progress in photovoltaics, Research and Applications*, 7(6):471–474, 1999.

[49] S. R. Wenham, S. J. Robinson, X. Dai, J. Zhao, A. Wang, Y. H. Tang, A. Ebong, C. B. Honsberg, and M. A. Green. Rear surface effects in high efficiency silicon solar cells. *Photovoltaic Energy Conversion, 1994., Conference Record of the Twenty Fourth. IEEE Photovoltaic Specialists Conference - 1994, 1994 IEEE First World Conference on*, 2:1278–1282, 1994.

[50] E. Van Kerschaver and G. Beaucarne. Back-contact solar cells: a review. *Progress in Photovoltaics: Research and Applications*, 14(2):107–23, 2006.

[51] E. Van Kerschaver, R. Einhaus, J. Szlufcik, J. Nijs, and R. Mertens. A novel silicon solar cell structure with both external polarity contacts on the backsurface. In *2nd World Conference on Photovoltaic Energy Conversion*, pages 1479–1482, 1998.

[52] J. M. Gee, W. K. Schubert, and P. A. Basore. Emitter wrap-through solar-cell. *23rd IEEE Photovoltaic Specialists Conference*, pages 265–270, 1993.

[53] J. M. Gee, M. E. Buck, W. K. Schubert, and P. A. Basore. Progress on the emitter wrap-through silicon solar cell. In The Netherlands Amsterdam, editor, *Proceedings of the 12th European Photovoltaic Solar Energy Conference*, pages 743–6, 1994.

[54] R. J. Schwartz and M. D. Lammert. Silicon solar cells for high concentration applications. *IEEE International Electron Devices Meeting*, pages 350–352, 1975.

[55] M. D. Lammert and R. J. Schwartz. The interdigitated back contact solar cell: a silicon solar cell for use in concentrated sunlight. *IEEE Transactions on Electron Devices*, 24(4):337–342, 1977.

[56] D. Rover, P. Basore, and G. Thorson. Solar cell modeling on personal computers. *Conference Record of the 18th IEEE Photovoltaic Specialists Conference*, pages 703–709, 1985.

[57] Silvaco. *Atlas*.

[58] COMSOL. *Multiphysics*.

[59] R. E. Bank, D. J. Rose, and W. Fichtner. Numerical methods for semiconductor device simulation. *IEEE Trans. Electron Devices*, 30(9):1031–1041, 1983.

[60] M. N. O. Sadiku. Numerical techniques in electromagnetics. *Second Edition*, 2, 2000.

[61] P. P. Altermatt. Models for numerical device simulations of crystalline silicon solar cells: a review. *Journal of Computational Electronics*, 10:314, 2011.

[62] P. P. Altermatt, J. O. J. O. Schumacher, A. Cuevas, M. J. Kerr, S. W. Glunz, R. R. King, G. Heiser, and A. Schenk. Numerical modeling of highly doped si:p emitters based on fermi dirac statistics and self-consistent material parameters. *Journal of Applied Physics*, 92:3187, 2002.

[63] A.B. Sproul and M. Green. Improved value for the silicon intrinsic carrier concentration from 275 to 375 k. *Journal of Applied Physics*, 70:846–854, 1991.

[64] P. P. Altermatt, A. Schenk, F. Geelhaar, and G. Heiser. Reassessment of the intrinsic carrier density in crystalline silicon in view of band-gap narrowing. *Journal of Applied Physics*, 93:1598–1604, 1991.

[65] A. Schenk. Finite-temperature full random-phase approximation model of band gap narrowing for silicon device simulation. *Journal of Applied Physics*, 84(7):3684–3695, 1998.

[66] W. Bludau, A. Onton, and W. Heinke. Temperature dependence of the band gap in silicon. *J. Appl.Phys.*, 45:1846–1848, 1974.

[67] H. S. Bennett and C. L. Wilson. Statistical comparisons of data on band-gap narrowing in heavily doped silicon: Electrical and optical measurements. *J. Appl. Phys*, 55(2):3582–3587, 1944.

[68] J. W. Slotboom and H. C. Degraaff. Measurements of bandgap narrowing in si bipolar-transistors. *Solid-State Electronics*, 19(10):857–862, 1976.

[69] J. W. Slotboom. The pn-product in silicon. *Solid-State Electronics*, 20(4):279–283, 1977.

[70] J. W. Slotboom and H. C. de Graaff. Bandgap narrowing in silicon bipolar transistors. *IEEE Trans. Electron Devices*, 24(8):1123–1125, 1977.

[71] D. B. M. Klaassen, J. W. Slotboom, and H. C. de Graaff. Unified apparent bandgap narrowing in n- and p-type silicon. *Solid-State Electronics*, 35(2), 1992.

[72] S. C. Jain and D. J. Roulston. Simple expression for band gap narrowing (BGN) in heavily doped Si, Ge, GaAs and GexSi1-x strained layers. *Solid-State Electronics*, 34(5):453–465, 1991.

[73] J. del Alamo, S. Swirhun, and R. Swanson. Simultaneous measurement of hole lifetime, hole mobility and bandgap narrowing in heavily doped n-type silicon," in. *International Electron Devices Meeting*, pages 290–293, 1985.

[74] S. E. Swirhun, Y.H. Kwark, and R. M. Swanson. Measurement of electron lifetime, electron mobility and band-gap narrowing in heavily doped p-type silicon. *IEDM Technical Digest, Los Angeles,CA, USA*, 32:24–27, 1986.

[75] J. A. del Alamo and R. M. Swanson. Measurement of steady-state minority-carrier transport parameters in heavily doped n-type silicon. *IEEE Trans. Electron Devices*, 34(7):1580–1589, 1987.

[76] R. De Rose, M. Zanuccoli, P. Magnone, E. Sangiorgi, and C. Fiegna. Open issues for the numerical simulation of silicon solar cells. *Ultimate Integration on Silicon (ULIS), 2011 12th International Conference on*, pages 1–4, 2011.

[77] D. B. M. Klaassen. A unified mobility model for device simulation ii. temperature dependence of carrier mobility and lifetime. *Solid-State Electronics*, 35(7):961–967, 1992.

[78] A. Richter, S. Glunz, F. Werner, J. Schmidt, and A. Cuevas. Improved quantitative description of auger recombination in crystalline silicon. *Phys. Rev. B*, 86, 2012.

[79] F. Ma, H. Liu, B. Liao, J. Chen, Z. Du, G. S. Samudra, A. G. Aberle, B. Hoex, and I. M. Peters. Impact of auger recombination parameterizations on predicting silicon wafer solar cell performance. *Journal of Computational Electronics*, 13(3):647–656, 2014.

[80] C. Reichel, F. Granek, M. Hermle, and S. W. Glunz. Investigation of electrical shading effects in back-contacted back-junction silicon solar cells using the two-dimensional charge collection probability and the reciprocity theorem. *Journal of Applied Physics*, 109(2), 2011.

[81] P. Altermatt, H. Plagwitz, R. Bock, J. Schmidt, R. Brendel, M. J. Kerr, and A. Cuevas. The surface recombination velocity at boron-doped emitters: comparison between various passivation techniques. *21st European Photovoltaic Solar Energy Conference*, 647, 2006.

[82] B. Hoex, J. Schmidt, R. Bock, P. P. Altermatt, M. C. M. van de Sanden, and W. M. M. Kessels. Excellent passivation of highly doped p-type si surfaces by the negative charge-dielectric Al2O3. *Applied Physics Letters*, 91(7), 2007.

[83] B. Phong. Illumination for computer generated pictures. *Communications of the ACM*, 18:311, 1975.

[84] K. R. McIntosh, M. J. Cudzinovic, D. D. Smith, W. P. Mulligan, and R. M. Swanson. The choice of silicon wafer for the production of low-cost rear-contact solar cells. In *3rd World Conference on Photovoltaic Energy Conversion*, pages 971–974, 2003.

[85] P. Magnone, D. Tonini, R. De Rose, M. Frei, F. Crupi, E. Sangiorgi, and C. Fiegna. Numerical simulation and modeling of resistive and recombination losses in mwt solar cells. *IEEE Journal of Photovoltaics*, 3(4):1215–1221, 2013.

[86] R. De Rose, P. Magnone, M. Zanuccoli, E. Sangiorgi, and C. Fiegna. Loss analysis of silicon solar cells by means of numerical device simulation. *Ultimate Integration on Silicon (ULIS), 2013 14th International Conference*, pages 205–208, 2013.

[87] R. R. King, R. Sinton, and R. Swanson. Studies of diffused phosphorus emitters : Saturation quantum efficiency. *IEEE transactions on electron devices*, 37:365, 1990.

[88] F. Granek, M. Hermle, C. Reichel, A. Grohe, O. Schultz-Wittmann, and S. Glunz. Positive effects of front surface field in high-efficiency back-contact back-junction n-type silicon solar cells. *Photovoltaic Specialists Conference, 2008. PVSC '08. 33rd IEEE*, pages 1–5, 2008.

[89] R. R. King and R. M. Swanson. Studies of diffused boron emitters: saturation current, bandgap narrowing, and surface recombination velocity. *IEEE Transactions on Electron Devices*, 38(6):1399–1409, 1991.

[90] P. J. Cousins, D. D. Smith, H.C. Luan, J. Manning, T. D. Dennis, A. Waldhauer, K. E. Wilson, G. Harley, and W. P. Mulligan. Generation 3: Improved performance at lower cost. *Photovoltaic Specialists Conference (PVSC)*, pages 275–278, 2010.

[91] J. Renshaw, M. H. Kang, V. Meemongkolkiat, A. Rohatgi, D. Carlson, and M. Bennett. 3d-modeling of a backpoint contact solar cell structure with a selective emitter. *34th IEEE Photovoltaic Specialists Conference (PVSC)*, pages 375–379, 2009.

[92] O. Nichiporuk, A. Kaminski, M. Lemiti, A. Fave, and V. Skryshevsky. Optimization of interdigitated back contacts solar cells by two-dimensional numerical simulation. *Solar Energy Materials and Solar Cells*, 86:517, 2005.

[93] M. Hermle, F. Granek, S. W. Glunz, and O. Schults-Wittman. Shading effects in back-junction back-contacted silicon solar cells. *33rd IEEEPhotovoltaic Specialist Conference*, 2008.

[94] E. Franklin, K. Fong, K. McIntosh, A. Fell, A. Blakers, T. Kho, D. Walter, D. Wang, N. Zin, M. Stocks, E.C. Wang, N. Grant, Y. Wan, Y. Yang, X. Zhang, Z. Feng, and P.J. Verlinden. Design, fabrication and characterisation of a 24.4interdigitated back contact solar cell. *Progress in Photovoltaics: Research and Applications*, 24(4):411–427, 2014.

[95] J. Renshaw and A. Rohatgi. Device optimization for screen printed interdigitated back contact solar cells. *Photovoltaic Specialists Conference (PVSC), 2011 37th IEEE*, pages 002924–002927, 2011.

[96] S. Kluska, F. Granek, M. Rüdiger, M. Hermle, and S. W. Glunz. Modeling and optimization study of industrial n-type high-efficiency back-contact back-junction silicon solar cells. *Solar Energy Materials and Solar Cells*, 94(3):568 – 577, 2010.

[97] F. Granek, M. Hermle, D. M. Huljic, O. Schultz-Wittmann, and S. W. Glunz. Enhanced lateral current transport via the front n+ diffused layer of n-type high-efficiency back-junction back-contact silicon solar cells. *Progress in Photovoltaics*, 17(1):47–56, 2009.

[98] L.J. Koduvelikulathu, V.D. Mihailetchi, G. Galbiati, A. Halm, R. Roescu, R. Kopecek, and K. Peter. 2D modeling of n-type ibc solar cells using silvaco atlas simulation. *11th International Conference on Numerical Simulation of Optoelectronic Devices, IEEE, Rome*, 2011.

[99] M. Zanuccoli, P. Magnone, E. Sangiorgi, and C. Fiegna. Analysis of the impact of geometrical and technological parameters on recombination losses in interdigitated back-contact solar cells. *Solar Energy*, 116:37–44, 2015.

List of Publications

- **V. Maccaronio, F. Crupi, L.M. Procel, L. Goux , E. Simoen, L. Trojman**,
  DC and low-frequency noise behavior of the conductive filament in bipolar HfO2-based resistive random access memory,
  Microelectronic Engineering 107, 1-5 (2013).

- **L.M. Pròcel, L. Trojman, J. Moreno, V. Maccaronio, F. Crupi, R. Degraeve, L. Goux, E. Simoen**,
  Experimental evidence of the quantum point contact theory in the conduction mechanism of bipolar HfO2-based resistive random access memories,
  Journal of Applied Physics, 114 (7), 074509 (2013).

- **P. Procel, V. Maccaronio, F. Crupi, G. Cocorullo, M. Zanuccoli**,
  Analysis of the impact of rear side geometry on performance of back-contact back-junction solar cells,
  Italian Conference on Photonics Technologies, Fotonica AEIT, Napoli (2014).

- **P. Procel, V. Maccaronio, F. Crupi, G. Cocorullo, M. Zanuccoli, P. Magnone, C. Fiegna**,
  Analysis of the impact of doping levels on performance of back-contact back-junction solar cells,

International Conference on Crystalline Silicon Photovoltaics, Energy Procedia 55, 128-132 (2014).

- **P. Procel, M. Guevara, V. Maccaronio, N. Guerra, F. Crupi, G. Cocorullo**,
  Understanding the Optimization of the Emitter Coverage in BC-BJ Solar Cells,
  Energy Procedia 77, 149-152 (2015).

- **M Guevara, P Procel, N Guerra, S Pierro, V Maccaronio, F Crupi, G Cocorullo**, Numerical simulation of back contact-back junction solar cells with emitter double contact,
  IET Conference Proceedings (2015).

- **P. Procel, M. Zanuccoli, V. Maccaronio, F. Crupi, G. Cocorullo, P. Magnone, C. Fiegna**,
  Numerical simulation of the impact of design parameters on the performance of back-contact back-junction solar cell,
  Journal of Computational Electronics, 15 (1), 260-268 (2016).